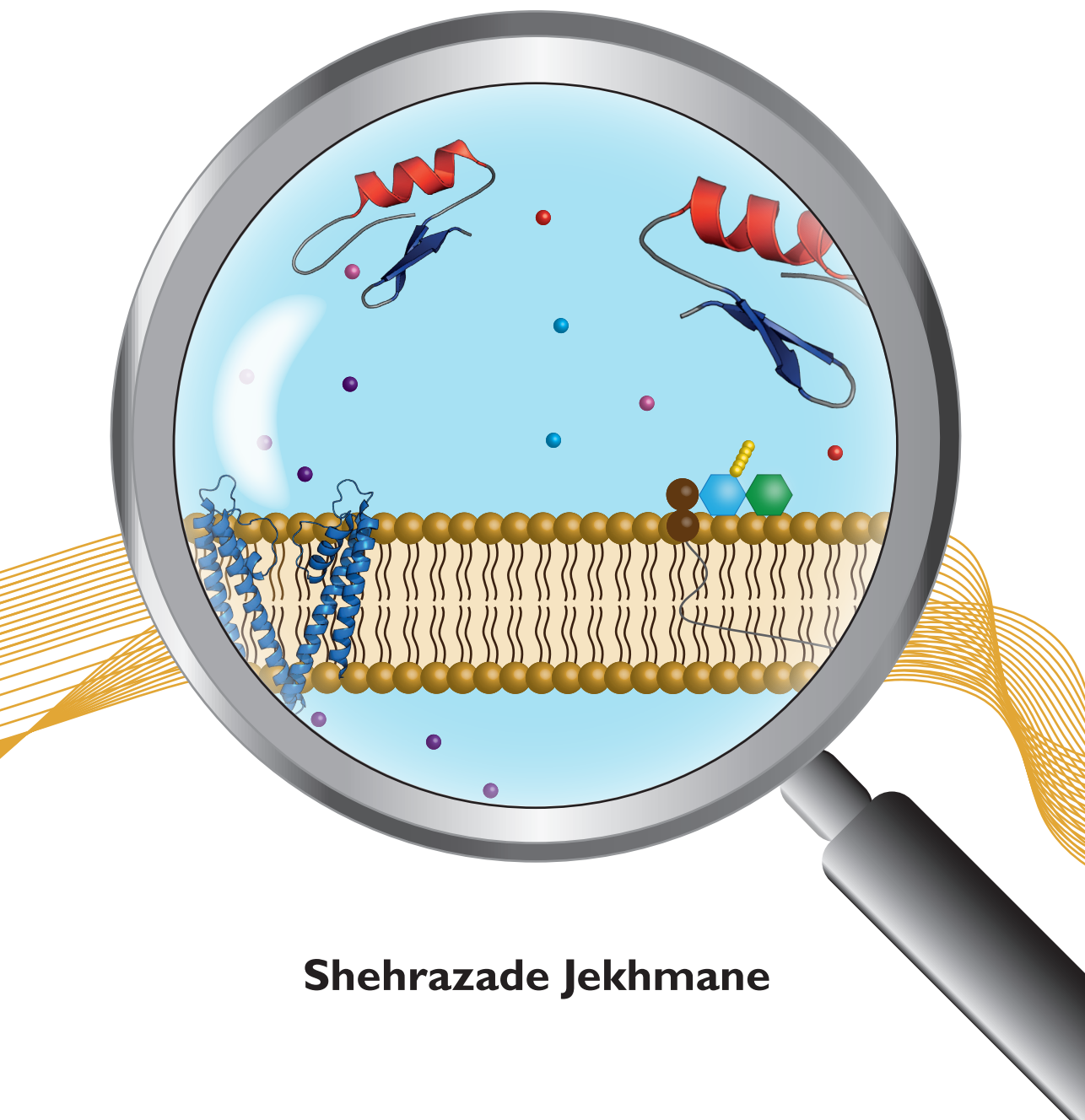# Solid-state **NMR** studies on therapeutic peptides

Shehrazade Jekhmane

Solid-state NMR studies on therapeutic peptides

Shehrazade Jekhmane

Solid-state NMR studies on therapeutic peptides

Vaste stof NMR studies aan therapeutische peptiden

(met een samenvatting in het Nederlands)

Proefschrift

ter verkrijging van de graad van doctor aan de
Universiteit Utrecht
op gezag van de
rector magnificus, prof.dr. H.R.B.M. Kummeling,
ingevolge het besluit van het college voor promoties
in het openbaar te verdedigen op

woensdag 6 mei 2020 des middags te 2.30 uur

door

Shehrazade Jekhmane

geboren op 17 december 1991
te Den Haag

Promotor:

Prof. dr. M. Baldus

Copromotor:

Dr. M.H. Weingarth

Table of contents

List of Abbreviations

AFM	Atomic Force Microscopy
AIFA	Agenzia Italiana del Farmaco
AMPs	Antimicrobial Peptides
AMR	Antimicrobial Resistance
BHMP1	Bone Marrow Homing Peptide
Ca^{2+}	Calcium
CAMHB	Cation-Adjusted Mueller-Hinton Broth
Cg-Def	Cg-Defh1, Cg-Defh2 and Cg-Defm
CLSI	Clinical and Laboratory Standards Institute
CP	Cross Polarization
CSA	Chemical Shift Anisotropy
CSPs	Chemical Shift Perturbations
CV	Column Volumes
cryo-EM	cryo-Electron Microscopy
1D	one-Dimensional
2D	two-Dimensional
3D	three-Dimensional
7DIV	seven Days *In Vitro*
DNP	Dynamic Nuclear Polarization
DOPC	1,2- Dioleoyl-sn-glycero-3-Phosphocholine
DPC	Dodecylphosphocholine
EEA	European Economic Area
ECM	Extracellular Matrix
EM	Embryonic
EMA	European Medicines Agency
EU	European Union
FDA	Food and Drug Administration
FID	Free Induction Decay
G'	Loss Modulus
G"	Storage Modulus
gene SOEing	gene Splicing by Overlap Extension
GlcNAc	N-Acetylglucosamine
HetNOE	Heteronuclear NOE
High P_0	High Open Probability

|	
H^N	Amino Protons
hNSC	human Neural Stem Cell
ITC	Isothermal Titration Calorimetry
K^+	Potassium
K_v	Voltage-gated K+
Low P_0	Low Open Probability
MAS	Magic Angle Spinning
MD	Molecular Dynamics
mDAP	meso-Diaminopimelic Acid
Mg^{2+}	Magnesium
MIC	Minimum Inhibitory Concentration
Mn^{2+}	Manganese
MRSA	Methicillin-resistant *Staphylococcus aureus*
MurNAc	N-Acetylmuramic acid
NMR	Nuclear Magnetic Resonance
PCR	Polymerase Chain Reaction
PEG	Polyethylene Glycol
PGA	Poly-Glycolic Acid
PGN	Peptidoglycan
PLA	Poly-Lactic Acid
PME	Particle-Mesh Ewald
PPi	Pyrophosphate
RGD	Arginine-Glycine-Aspartic acid
rMD	restraint MD
S0-S4	K^+ coordination sites
SAPs	Self-Assembling Peptides
Sc	central water-filled cavity
SCI	Spinal Cord Injury
SCS	Secondary Chemical Shift
SF	Selectivity Filter
ssNMR	solid-state NMR
SUVs	Small Unilamellar Vesicles
ThT	Thioflavin T
TM	Transmembrane
ZQ	Zero-Quantum

CHAPTER 1

General introduction

Introduction

The structure of biomolecules is of crucial importance for their functions. Hence, gaining knowledge on their structure will allow us to understand, for example, how they relate to particular disease symptoms. Therefore, the field of structural biology became especially important in the areas of medicine and drug development. X-ray crystallography enabled the first structural studies of biomolecules, such as the discovery of the DNA structure. Nowadays, there are numerous techniques, including cryo-electron microscopy (cryo-EM) and solution Nuclear Magnetic Resonance (NMR) spectroscopy, that permit the study of biomolecules and their structure.

Although the field of structural biology is still dominated by X-ray crystallography, solution NMR provides unique advantages for structural studies and is an integral part of drug discovery[2-5]. However, as the major focus in the field of drug development is shifting towards membrane proteins as drug target[8,9], solution NMR faces several limitations. Solid-state NMR (ssNMR), on the other hand, has no size limitations and allows the study of membrane-embedded or membrane-associated proteins in their close-to physiological context, which has been shown to be of critical value[10]. Moreover, pioneering developments have further pushed the boundaries of ssNMR and enabled the study of proteins directly in whole cells[11]. These progresses offer a great potential to expand the utility of ssNMR in drug development where structural features of drug targets and drug-target complexes can guide medicinal chemistry towards promising drug candidates. Also heterogeneous solids such as amyloid fibrils[12], cytoskeletal filaments[13] and nucleoprotein complexes[14] are amenable to ssNMR. Moreover, ssNMR is not limited to the analysis of structures only. It is a very versatile tool which, for example, can be applied to resolve target binding sites and to obtain site-specific information on the dynamics of the subjected complex from picosecond to second time timescales. Altogether, ssNMR is a powerful tool that will undoubtedly improve our current understanding on how to use membrane proteins as drug targets.

The work described in this thesis further underlines the versatility and strength of ssNMR in drug development. We show how NMR can be used to gain further knowledge on three different systems that might contribute to the design of novel therapeutics (Figure 1). These complexes include:

- the peptide antibiotic plectasin and the complex it forms with its target lipid II,
- self-assembling peptidic hydrogel scaffolds for tissue engineering of the spinal cord,
- the potassium channel KcsA.

These systems, together with the fundamental aspects of NMR, will be further introduced in the following sections.
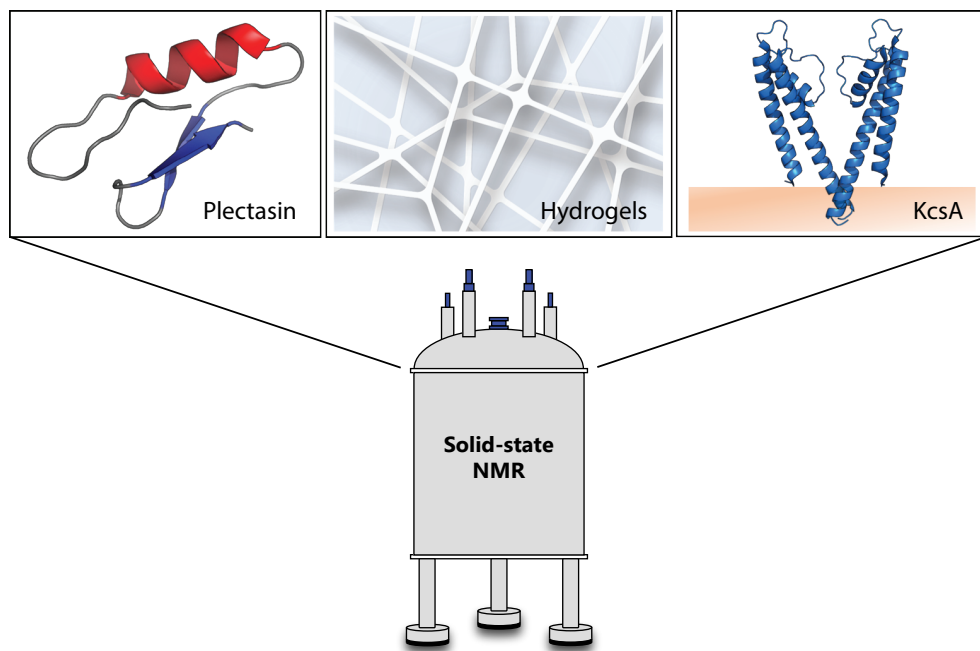

Figure 1. In this work, ssNMR is used to study three different systems: plectasin and its target, hydrogel scaffolds for tissue engineering, and KcsA.

Nuclear Magnetic Resonance

The principle behind NMR spectroscopy is that every atomic nucleus possesses an intrinsic property called a spin (I) that in turn has a magnetic moment (μ). Only nuclei with a non-zero spin have a magnetic moment and are thus visible for NMR spectroscopy. The magnetic moment, quantized into 2I + 1 directions, forces a spin to act as a tiny bar magnet and aligns the initially randomly oriented spin either with (low energy state) or against (high energy state) the applied external magnetic field. The interaction between the magnetic field and the spin is also known as the Zeeman interaction. The energy of a spin state can be calculated with the following equation:

$$E_z = -\gamma m \frac{h}{2\pi} B_0 \tag{1.1}$$

where E_z is the energy of the individual spin state, γ is the gyromagnetic ratio of the nucleus, h is the Planck's constant and B_0 is the externally applied magnetic field. In case of a spin ½, two different energy levels would be present (Figure 2).
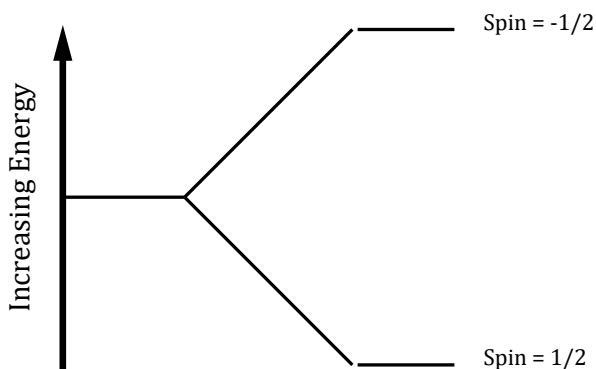
Figure 2. Simplified Zeeman energy levels for a nucleus with a spin ½ when placed in an external magnetic field.

Supposing there is an ensemble of nuclear spins, which is typically the case in an NMR sample, each of this energy state would have a certain population degree defined as p_α and p_β. The population distribution in the different states is described by the Boltzmann distribution:

$$\frac{p_\beta}{p_\alpha} = e^{-hv/kT} \tag{1.2}$$

where k is the Boltzmann constant, v is the Larmor frequency and T is the absolute temperature. The Larmor frequency is the rate by which spins precess around the magnetic field. More nuclei will occupy the low energy state rather than the high energy state, hence there will be a net magnetization aligned

with the applied magnetic field. This net or excess magnetization can be used for NMR studies, however, the excess corresponds to about 0.1 % of the spins, which can make sensitivity a challenge for NMR studies. Sensitivity issues can be overcome by, e.g., increasing the external applied magnetic field, decreasing the temperature or by detection on nuclei with a high γ. The latter strategy will be discussed further in the chapter.

In a typical NMR experiment, the response of the spins to applied radiofrequency (RF) pulses is measured. The RF pulses excite the spins from a low energy state (ground state) to a higher energy state (excited state), and the electric current induced by the excited state is acquired as a so-called free induction decay (FID).

Spin interactions in NMR

In this section, we briefly introduce the most relevant internal spin interactions in biological NMR. These interactions include the chemical shift, J-coupling, and dipolar coupling. While the chemical shift and the dipolar coupling are orientation-dependent, the J-coupling is orientation-independent.

Chemical shift

Besides spins, also electrons that orbit around nuclei are affected by the external applied magnetic field. The magnetic field causes the electrons to induce an electric current which in turn causes a local magnetic field at the nucleus. In other words, the spins are being "shielded" by the surrounding electrons from the external magnetic field. The magnitude of shielding depends largely on the density of electrons around the nucleus and the applied magnetic field, and is generally given by the parameter δ. The shielding of the nuclear spins is anisotropic, given that the electrons are not equally distributed around any kind of nucleus. This gives rise to chemical shift anisotropy (CSA).

J-coupling (scalar coupling)

J-coupling involves spin-spin interactions that are operated through bonding electrons. These so-called indirect spin-spin interactions are caused by hyperfine interactions between the nuclei and the local electrons. The J-coupling has both isotropic and anisotropic properties. The latter, however, is usually of no practical importance in NMR. The isotropic part of the J-coupling is a fundamental tool in NMR, especially in solution NMR, and is usually referred to as scalar coupling. It provides with information on the through-bond connectivity of atoms, which is manifested by signal splitting in NMR spectra.

Dipolar coupling

The dipolar coupling is a through space anisotropic interaction and

arises from two interacting spins that have a magnetic moment. This type of interaction is usually magnitudes stronger than J-coupling and depends on the gyromagnetic ratios and the cube of the distance of the interacting spins:

$$D = \gamma_1 \gamma_2 \left(\frac{h}{4\pi^2}\right)\left(\frac{\mu_0}{4\pi}\right) r_{1,2}^{-3} \tag{1.3}$$

where D is the dipolar coupling constant and r is the distance between spins 1 and 2, respectively. Dipolar coupling of spins occurs either between two of the same nuclei (homonuclear dipolar coupling) or between two different nuclei (heteronuclear dipolar coupling). These couplings behave differently during Magic Angle Spinning because of the presence of zero-quantum (ZQ) operators in the homonuclear dipolar Hamiltonian. These ZQ transitions render Hamiltonian time-dependent, which especially for strong homonuclear proton couplings prevents efficient averaging by MAS. For a homonuclear spin pair, the dipolar coupling can be expressed as:

$$H_D^{II} = \frac{1}{2}\frac{\mu_0\gamma_1\gamma_2h^2}{16\pi^3r^3}(3cos^2\theta - 1)(3I_{1z}I_{2z} - I_1 \cdot I_2) \tag{1.4}$$

Heteronuclear dipolar couplings of spins can be described by the following formula:

$$H_D^{IS} = \frac{\mu_0\gamma_1\gamma_2h^2}{16\pi^3r^3}(3cos^2\theta - 1)I_{1z}I_{2z} \tag{1.5}$$

Magic Angle Spinning

The aforementioned anisotropic interactions that nuclei experience can lead to very broad and featureless NMR signals in solids. In solution NMR, these interactions are averaged out by the fast tumbling of molecules, leaving only isotropic interactions such as the chemical shift and the relatively small (about 100 Hz) J-couplings. As a result, solution NMR spectra can feature exquisite resolution. In ssNMR, however, anisotropic interactions on the order of up to 100 kHz are present and can lead to substantially broadened signals. High-resolution can be restored in ssNMR with a technique called Magic Angle Spinning (MAS)[10]. By physically rotating the NMR sample at an angle of 54.74°, with respect to the direction of the external magnetic field, anisotropic NMR interactions such as CSA and dipolar couplings are cancelled out partially or completely (Figure 3). The MAS frequency is of prime importance in this case and needs to exceed the linewidth in order to avoid incomplete averaging of anisotropic interaction[15,16]. In practice, this is very difficult to achieve due to the very strong time-dependent ^{1}H-^{1}H dipolar couplings (~120 kHz). In spite of these complications, MAS spinning of NMR samples drastically improves the spectral quality and enables the application of sensitivity-enhancing and high-resolution NMR techniques such as ^{1}H-detection.
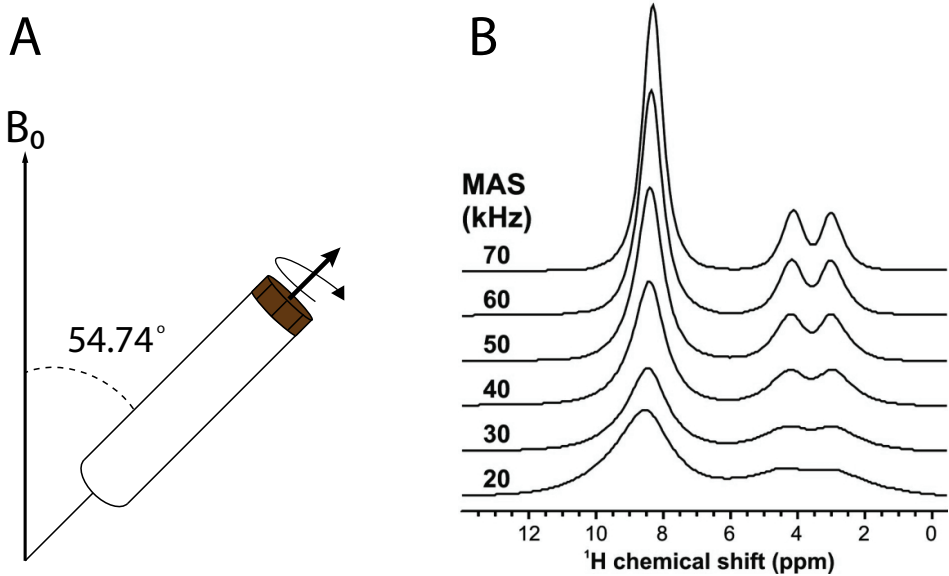
Figure 3. A) Schematic illustration of MAS. An NMR rotor containing sample is rotated physically at an angle of 54.75° relative to the magnetic field B0. B) ^{1}H NMR spectra of glycine at different MAS speeds. MAS significantly improves the spectral resolution[1].

[1]H detection

The broad applicability of NMR in biomedical research in solutions owes its success to the high sensitivity of ^{1}H due to its high natural abundance and γ. The γ of ^{1}H is about 4 and 10 times higher than for ^{13}C and ^{15}N, respectively. Since detection sensitivity relates to $(H_y/X_y)^{3/2}$, ^{1}H detection can in principal enable sensitivity gains of more than 30 for [15]N. It is therefore no surprise that [1]H-detection is becoming more and more routine in ssNMR. However, as discussed before, [1]H-^{1}H dipolar couplings are very strong and have to be attenuated, which can be achieved via fast (>50 kHz) MAS.

Relaxation and dynamics

NMR not only elucidates molecule structure, it also permits to probe dynamics in atomic detail by so-called relaxation measurements. Relaxation is a process where excited spins revert back to the ground state, thus where the net magnetization goes back to its equilibrium situation. In ssNMR there are distinct classes of relaxation processes that enable to probe different motional timescales. Below are three relaxation processes that were measured in this thesis:

T$_1$ relaxation

This relaxation process is also referred to as spin-lattice or longitudinal relaxation. It involves the restoration of the net magnetization, in the direction parallel to the magnetic field (z-plane), according to the Boltzmann distribution. T$_1$ relaxation can be used to probe motion on the fast picosecond-nanosecond time scale and is expressed as:

$$M_z(t) - M_0 = [M_z(0) - M_0]e^{-t/T_1} \tag{1.6}$$

with M$_z$ the magnetization in the z-plane after perturbation.

T$_2$ relaxation

T$_2$ relaxation, also known as spin-spin or transverse relaxation, takes place perpendicular to the magnetic field (xy-plane). At equilibrium, the net magnetization in the xy-plane equals to 0. It becomes non-zero when RF pulses are applied on the nuclear spins resulting in a transition of magnetization from the z-plane to the xy-plane. T$_2$ relaxation is the process by which the magnetization in the xy-planes decays and is expressed as:

$$M_{xy} = M_{xy}(0)e^{-t/T_2} \tag{1.7}$$

The time constant T$_2$ is typically small, in the order of microseconds and its magnitude dominates the linewidth of signals. The ratio between T$_2$ and T$_1$ relaxation rates is a commonly used approach to assess chemical exchange in a given system[17].

It should be noted that T$_2$ is usually not measured in ssNMR due to residual dipolar couplings. Instead, ssNMR uses T$_{1\rho}$ relaxation to probe dynamics on slower timescales.

T$_{1\rho}$ relaxation

T$_{1\rho}$ relaxation or spin-lattice relaxation in the rotating frame is very similar to T$_2$ relaxation. It also involves the decay of the magnetization in the xy plane. However, in T$_{1\rho}$ the reversion to equilibrium is under the influence of a continuous RF-field that captures the magnetization in the xy plane. This RF is often referred to as a spin-lock. T$_{1\rho}$ relaxation is typically used to probe the slow nanosecond to microsecond dynamics of a given system. Notably, T$_{1\rho}$ relaxation measurements in biomolecules are markedly facility at fast (>50 kHz) MAS frequencies[18].

A new generation of antibiotics

The widespread emergence of antimicrobial resistance (AMR) is dissipating the public health assurance that was once created by the large availability of antibiotics. The increasing prevalence of pathogens resistant to numerous of currently used antibiotics[19,20] places a significant burden on the health care system. A recent report showed that the health care burden in the European Union (EU) and European Economic Area (EEA) is similar to the combined effect of influenza, HIV and tuberculosis, and will account for 33 000 deaths every year[21]. As a consequence, AMR will also economically impact European countries[22]. This challenging pattern of multidrug resistant pathogens demands for novel antibiotics that target unexploited pathways and that are robust to AMR development. Naturally occurring antimicrobial peptides (AMPs) are an interesting class of antibiotics and have proven to be effective throughout evolution[23]. A promising class of AMPs targets lipid II, a crucial precursor in the synthesis of the bacterial peptidoglycan (PGN) network[24,25], and kills multidrug resistant pathogens at nanomolar levels. Especially AMPs that specifically target the pyrophosphate moiety of lipid II, which is deemed irreplaceable, are less sensitive to AMR development. Hence, lipid II, also referred as "the bacterial Achilles' heel", is an exquisite antibiotic target[24].

Lipid II – a validated target for antibiotics

All bacterial cell walls are composed of a PGN network that provides bacterial cells of any given species with shape and integrity. Therefore, a robust regulation of the PGN network synthesis is demanded upon bacterial growth. The PGN network is universally characterized by linear glycan chains, composed of alternating units of N-acetylmuramic acid (MurNAc) and N-acetylglucosamine (GlcNAc), that are interlinked by short peptide-bridges. Lipid II is key player in the synthesis of the PGN network as it carries one complete PGN subunit, which is connected to a unique pyrophosphate (PPi) group that is linked to a membrane-embedded C_{55} polyisoprenoid tail (Figure 4A).

The number of lipid II molecules in both Gram-positive and Gram-negative bacteria is limited, hence bacteria have encountered a dynamic so-called lipid II cycle where lipid II is constantly recycled to ensure effective PGN synthesis (Figure 4A). Therefore, the lipid II cycle forms an interesting target for antibiotic design. In short, any drug that sequesters lipid II and thereby blocks the PGN synthesis is considered a potential antibiotic candidate. The bacterial cell wall in Gram-positive bacteria is readily accessible from the outside for such peptides to interact with lipid II. The first identified lipid II targeting peptide is the glycopeptide vancomycin[26], which specifically binds the terminal acetyl-D-alanyl-D-alanine motif of the pentapeptide of lipid II[27,28]. For a long time, vancomycin was last resort drug for the treatment of infections with

Gram-positive bacteria, such as the infamous superbug methicillin-resistant Staphylococcus aureus (MRSA), which showed resistance against virtually all clinically used antibiotics. However, the emergence of vancomycin resistant pathogens[29] further emphasizes the need for novel antibiotics.
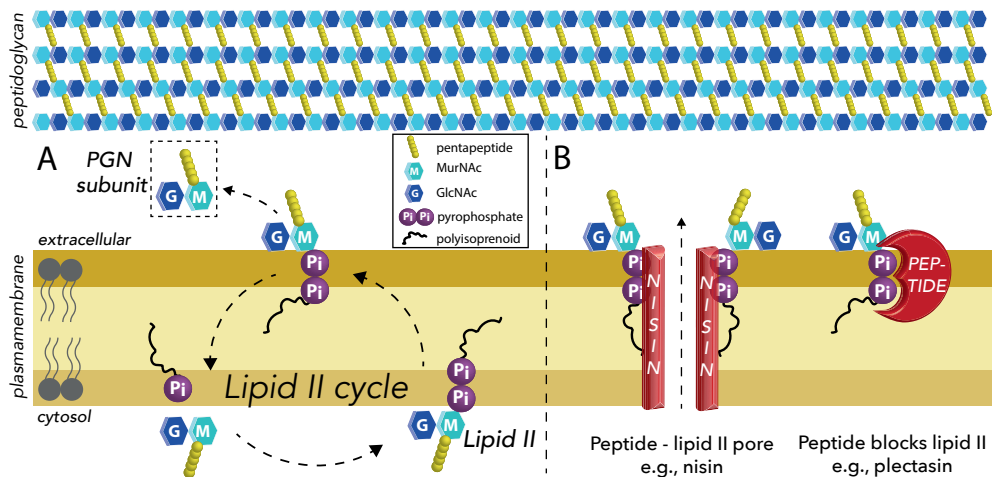
Figure 4. Lipid II is a validated target for novel antibiotic design. A) Lipid II is constantly recycled by the so-called "lipid II cycle" where it is assembled in the cytosol and flipped across the plasma membrane to maintain PGN network synthesis. B) Peptides can kill bacteria via two so far known mechanisms: targeted pore formation (left) and/or sequestering lipid II and hence blocking the PGN network synthesis (right).

Peptides that target the PPi group of lipid II not only show a unique mode of action that kills refractory bacteria such as MRSA at nanomolar concentrations, but are less prone to AMR development as the PPi group of lipid II is deemed irreplaceable. In addition, the presence of lipid II is limited to bacteria only and hence lipid II – targeting peptides do not display cytotoxicity towards mammalian cells. Therefore, peptides that target lipid II at the PPi group could form the foundations for next-generation antibiotics. However, detailed information on the medically relevant structural correlate of the drug – target complex is often scarce. Native structural studies on nisin, a lantibiotic that uses lipid II as a docking molecule to form pores in the membrane[30,31] (Figure 4B), revealed that indeed artificial media do not capture the biologically relevant nisin pore complex[32]. Moreover, novel features, that are crucial for the mode of action of nisin, were not accessible in membrane-less media. This further emphasizes the necessity of studying such small membrane-embedded drug-target complexes in native conditions.

Here, we briefly introduce a particularly interesting class of lipid II – targeting AMPs, the CSαβ defensins, for which, so far, only little structural data exists on the drug-target complex.

CSαβ defensin

Defensins are a family of small (3-5 kDa) host-defense peptides that are pivotal components of the innate immune system[33] in eukaryotes including mammals, invertebrates, plants and fungi. They are essentially ancient antibiotics that have potent activity towards a broad range of organisms. Their structural motif is defined by a β-sheet enriched fold and a framework that is held together by three to five disulfide bonds. Vertebrate defensins can be classified into three subgroups: α, β-, and θ-defensins. The latter is unique regarding its cyclic nature and is only found in Rhesus monkeys[34]. The signature motif of the α- and β-defensins includes a three-stranded antiparallel β-sheet structure[35]. Invertebrate[33] and numerous fungal defensins[36] adopt a cystine-stabilized α-helix-β-sheet fold and are therefore referred as CSαβ defensins.

Given the increasing interest in defensins and their applications, it is essential to understand their mode of action. To date, several CSαβ defensins were found to specifically target lipid II[31]. These peptides act by sequestering lipid II and thereby block the PGN network synthesis (Figure 4B). The first identified lipid II targeting CSαβ defensin is the fungal peptide plectasin, isolated from *Pseudoplectania nigrella*[37,38], which tightly binds to lipid II (K_D = 1.8 · 10^{-7} M) in a 1:1 stoichiometry. This discovery has led to the onset of a multiple of studies identifying novel lipid II targeting CSαβ defensin including the fungal defensins eurocin[39] and copsin[40], the oyster defensins Cg-Defh1, Cg-Defh2 and Cg-Defm[41] (Cg-Def) and the mussel defensin MGD-1[42]. These defensins show high structural similarity to plectasin. However, while plectasin and eurocin compose three disulfide bonds, copsin, MGD-1 and the oyster defensins have six disulfide bonds.

CSαβ defensins show great activity against a wide range of medically relevant Gram-positive bacteria, including penicillin-resistant *Streptococcus pneumoniae*[38,39,43]. They are tremendously stable due to the presence of several disulfide bonds and can be produced in large quantities. Altogether, CSαβ defensins form an excellent lead for the rational design of novel antibiotics. Interestingly, a plectasin triple mutant NZ2114 is currently in clinical trials[44]. This triple mutant is active against MRSA, whereas WT plectasin is not.

Although progress has been made in identifying the membrane target of plectasin and other CSαβ defensins, structural information on the drug - target complex is limited and completely absent in membranes. On the example of plectasin, our current structural understanding of the binding mode comes from a solution NMR study in dodecylphosphocholine (DPC) micelles with a truncated, water-soluble lipid II construct. Solution NMR titrations of lipid II containing micelles with plectasin showed chemical shift perturbations in a number of residues[38] that were used to derive a HADDOCK[45] model. This model

suggests that the backbone amide protons of residues F2, G3, C4 and C37 form hydrogen bonds with the lipid II pyrophosphate (Figure 5A). Interestingly, this binding motif is also present in both eurocin and MGD-1 (Figure 5B), which may imply that the binding mode is conserved among these defensins. Furthermore, the pentapeptide of lipid II was assumed to be at the complex interface where it forms hydrogen bonds with H18. This is in broad agreement with previous observations where enzymatic amidation of the D-glutamate of the pentapeptide radically affected the antimicrobial activity of plectasin[46].

These findings gave first insights into the mode of action of plectasin. However, many aspects remain unclear. For instance, the micelle model does not explain the big hit on the binding affinity of plectasin in the absence of the lipid II GlcNAc sugar[38], which is far from the complex interface (Figure 5A). Moreover, the ultra-conserved H18 (Figure 5B), which assumingly binds to the pentapeptide, was not observed in NMR studies in micelles[38]. It also does not provide with a structural foundation that explains the improved activity of the plectasin derivative NZ2114[44] towards *Staphylococcus aureus*. Moreover, experiments were performed using a water-soluble version of lipid II and therefore the 1:1 stoichiometry that was found might not be of relevance in the native complex with membrane-embedded lipid II. In addition, the functional nature of the negative patch (D9-E10-D11-D12, see Figure 5B) in plectasin remains unidentified.

While the fold is conserved, CSαβ defensins show only low sequence homology and have stark differences in the lengths of certain loops (Figure 5B, C). It remains unclear if these structural differences attribute to the binding mode to lipid II and if CSαβ defensins show at all a conserved mode of action.

In Chapters 2 and 3, we revisit the plectasin – lipid II complex in lipid membranes and aim to unravel important motifs with regards to the mode of action of plectasin. We reveal several features that were not observed in the micelle model and underline the relevance of studying such drug-target complexes in natural lipid membranes.
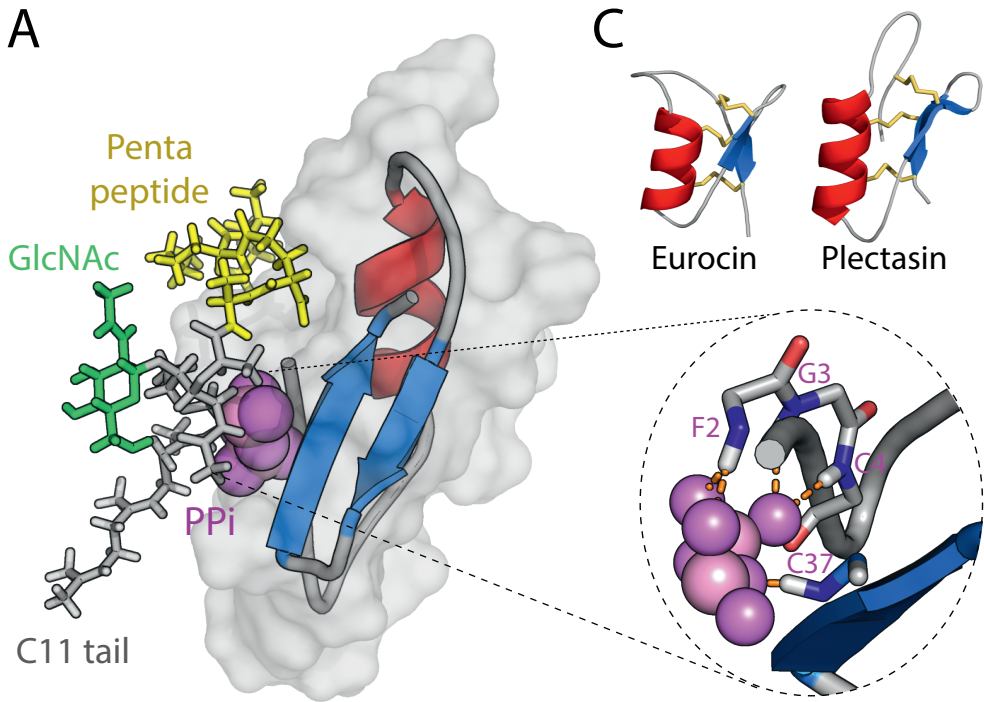
Figure 5. The mode of action of plectasin. A) CSP based docking model of the plectasin – lipid II complex in micelles. Plectasin coordinates the PPi group of lipid II through the backbone amino protons of residues F2, G3, C4 and C37 (see zoom, right). In this model, it is assumed that the pentapeptide of lipid II (yellow) is involved in plectasin binding. B) CSαβ defensins, including eurocin, show a similar fold as plectasin. Yet, they exhibit low sequence homology. C) Sequence alignment of several lipid II – binding CSαβ defensins. Conserved residues are indicated in orange, whereas the negative patch in plectasin is highlighted in red. The first ten residues of copsin are not included in the alignment.

Tissue Engineering

Tissue damage has a significant impact on life quality and expectancy as millions of deaths occur worldwide due to tissue dysfunction or loss. Tissue transplantation, although it can save lives, has serious limitations. The scarcity of organ donors[47,48] and prevalence of diseases, infections and rejections of tissue[48,49] associated with transplantations further complicate tissue transplantation. The situation is even more severe in undeveloped countries because of a lack of surgical services and infrastructure for rapid transport of organs. The field of tissue engineering has emerged to overcome these burdens and combines a multitude of disciplines to develop functional biological substitutes that restore, maintain or improve tissue function[50]. Central to the field is the use of embryonic (EM) stem cells because of their capacity to differentiate into a variety types of cells according to the provided stimuli (Figure 6).
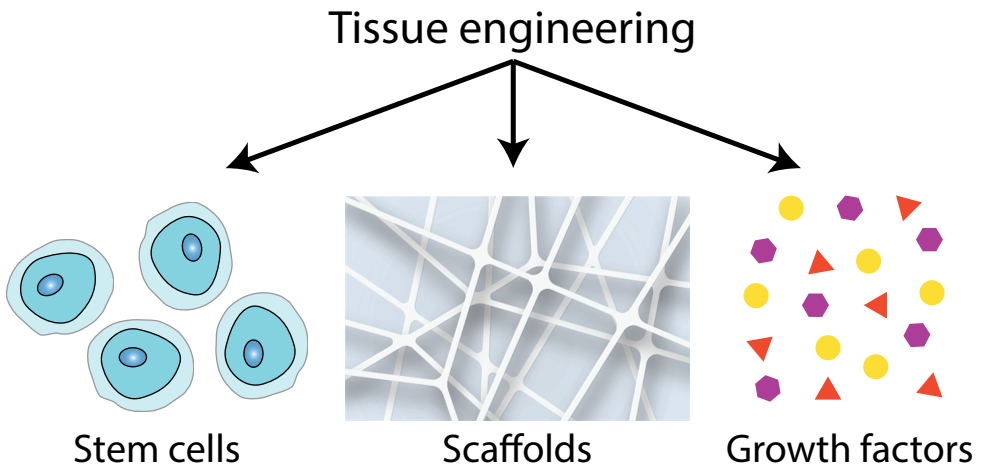
Figure 6. Tissue engineering is a complicated process involving the regeneration of healthy and functional tissue and can be considered to consist the triad of stem cells, scaffolds and growth factors.

Tissue engineering relies extensively on scaffolds to recapitulate the extracellular matrix (ECM) and accommodate and guide EM cells in their growth into specific tissue. They are therefore inherent to the success of tissue engineering. Ideal scaffolds should not only mimic the ECM in form, but also in functionality. Unfortunately, due to the complexity and diversity of the ECM, it is almost impossible to design scaffolds that are an exact replica in both form and functionality. Firstly, scaffolds should be biocompatible to avoid a triggered immune response, but at the same time have a suitable surface chemistry and structure for cell attachment and migration[51]. Secondly, the material of the scaffold should be well-considered as it dictates the mechanical properties of the scaffold which have to be consistent with the implantation site. To date, only

few scaffolds have been accepted by the Food and Drug Administration (FDA) and the European Medicines Agency (EMA)[52-54].

Scaffolds for tissue engineering

The first biomaterials that were designed for applications in the human body are hydrogels[55]. Hydrogels were initially designed for ocular use including contact lenses, but they are also qualified for tissue engineering purposes due to their highly hydrated 3D environment resembling the native ECM and their extensive architecture for cell proliferation and maintenance[56].

Hydrogels can be made from naturally derived or synthetic polymers. Natural polymers, including collagen, gelatine, fibrin, hyaluronic acid, silk, alginate and chitosan are highly biocompatible and have intrinsic characteristics of biological recognition which facilitate cell growth and proliferation. However, major rapid degradation, batch-to-batch differences, presence of impurities and the lack of control over the mechanical properties, architecture and structure of natural scaffolds make natural polymers far from ideal for clinical use[57]. Synthetic polymers are superior in this respect and offer high control over the mechanical and chemical properties. Moreover, they can be functionalized with the peptide unit arginine-glycine-aspartic acid (RGD)[58][29,30] which stimulates cell migration, proliferation, growth and organization[59]. Synthetic polymers that are widely used for scaffold production are poly-lactic acid (PLA), poly-glycolic acid (PGA) and polyethylene glycol (PEG)[60].

A more recent development in the flourishing area of tissue engineering has been the use of self-assembling peptides (SAPs) due to their incoherent biocompatibility and biodegradability[61-67]. One of the first SAP[68], EAK16 peptide, was inspired by the protein zuotin[69] that was serendipitously discovered in yeast. Several variants were derived from the EAK16 peptide, including the RAD16 peptide, and were shown to support cell attachment in a variety of cell types[70]. The group of Gelain biotinylated the RAD16 peptide and combined it with the biofunctional motif PFSSTKT which belongs to the Bone Marrow Homing Peptide (BHMP1) family. This intriguing biotinylated hybrid peptide not only exhibited outstanding assembly performance and biomechanics[71], but also promoted adhesion, proliferation and differentiation in human neural stem cell (hNSC) in vitro and in vivo [72,73].

Mechanical properties

The mechanical properties of hydrogels, on both macroscopic and microscopic level, play important roles in regulating cell behaviour. Macroscopically, they must withstand manipulations associated with cell culture proceedings and provide stability as the tissue regenerates. On the microscopic level, cells respond to the mechanical input of their microenvironment and alter their

genotype and phenotype depending on the mechanics of the environment[74,75]. Therefore, understanding the role of mechanical factors in redeveloping functional tissue is an important subject. In this regard, the exact attributes of mechanical properties that promote healthy tissue function remains unclear.
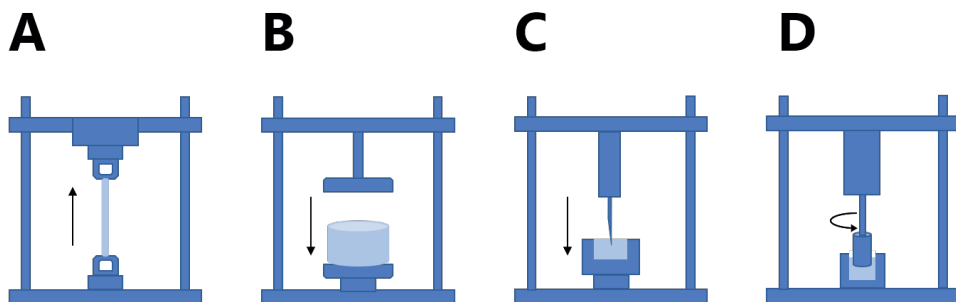
Figure 7. Common techniques to define the mechanical properties of hydrogels. A) Tensile tests. B) compression tests. C) Indentation tests. D) Oscillatory rheology. Different types of shearing geometries can be used attached to the rheometer, depending on the characteristics of the material: cone-plate, plate-plate and rotational cylinder. The latter is illustrated here.

Methods that have led to advances in our understanding of the mechanical functionality of scaffolds are tensile, compression and indentation tests, rheology measurements and Atomic Force Microscopy (AFM) (Figure 7A-D). However, a problem that is associated with these standard techniques is that they do not allow measurements of mechanical properties at the nano- and micro scales, let alone the atomic scale. As a consequence, molecular aspects that create a fundamental basis for the overall functionally of scaffolds remain unknown. Ideally, hydrogels should be exposed to techniques that enable the study of their mechanical properties at both macroscopic and atomic levels. An interesting alternative method that can provide with an unprecedented level of qualitative and quantitative evaluation of the mechanical properties of hydrogels is ssNMR. A multitude of studies have proven the success of ssNMR in the characterization of hydrogels[43,76-78]. Yet, none of these studies have reported on the mechanical properties of the subjected materials. In Chapter 4, we demonstrate how ssNMR can be used to exploit the mechanical properties of a number of SAP hydrogels that were designed by the group of Gelain[71]. We reveal previously unknown mechanical attributes that are inherent to the application of such scaffolds in tissue engineering.

KcsA: a model channel for potassium channels

Potassium (K^+) channels are the most widely distributed channels and are present in nearly all organisms[79,80]. They are membrane-spanning proteins that direct diverse important functions including the conduction of K^+ ions across the lipid barrier, thereby setting or resetting the resting potential in excitable and non-excitable cells[81]. K^+ conduction plays a key role in several cellular processes including hormone secretion, regulation of cell volume, and establishment of electrical pulses in excitable cells[82]. K^+ channels are highly specific for K^+ ions, ~10 000 times less permeant for Na^+ ions, and are able to conduct K^+ ions at near diffusion-limited rates (10^6 to 10^8 ions/channel/s)[83]. At the molecular level, ion discrimination is achieved by the so-called selectivity filter (SF). Recent advances in genetic linkage analysis have linked K^+ channel gene mutations or impaired function with various diseases of the heart, kidney, pancreas and nervous system[84]. An improved understanding of K^+ channels may lead to implications for the development of novel therapeutics targeting numerous impaired K^+ channels[85]. The identification of the prokaryotic K^+ channel KcsA from *Streptomyces lividans* has been of enormous value for the understanding of a large class of K^+ channels and is considered a model channel[86].

K^+ channels are divided into three major classes depending on their structure and function. These classes include: i) voltage-gated K^+ (K_v) channels, ii) two-pore K^+ channels and iii) inward rectifier K^+ channels containing six, four and two transmembrane (TM) helices, respectively. The basic organization of virtually all K^+ channels is a tetramer with four subunits that associate to form a fourfold symmetric complex around an ion pore. Notably, each subunit has two to six TM helices that bundle together at the C-terminus (activation gate), a central water-filled cavity (Sc), a pore helix that runs halfway through the membrane and a SF that coordinates the K^+ ions[86]. KcsA represents the simplest topology for a K^+ channel, a tetramer formed by four identical subunits of about 18 kDa, with each subunit containing only two TM helices (TM1 and TM2) (Figure 8A).

The SF is highly conserved in all K^+ channels and is composed by the amino acid sequence TVGYG (Figure 8B). It is characterized by four K^+ ion binding sites S1 – S4 that adopt a unique structural chain where carbonyl oxygen atoms are aligned towards the pore centre and serve as a ligand to the dehydrated K^+ ion (Figure 8C). Initially, it was believed that only S1 and S3 or S2 and S4 were occupied by K^+ ions and that water molecules accommodated the remaining sites[87]. However, contradicting studies have proposed a different scenario where K^+ ions move sequentially from one site to the next site as they move through the channel[6]. The exact mechanism is still under debate.
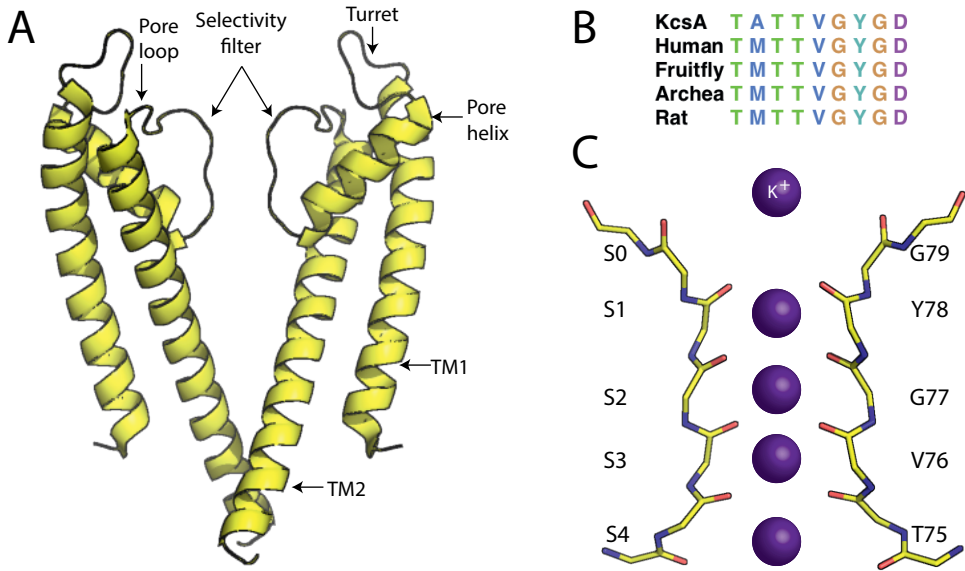
Figure 8. The basic organization of K+ channels is highly conserved. A) Structure of KcsA in the closed-conductive state. Each KcsA subunit is composed of two transmembrane helices (TM1 and TM2), one pore helix, one turret loop and a selectivity filter. B) The amino acid sequence TVGYG, which forms the selectivity filter, is highly conserved in K+ channels. C) The selectivity filter includes four cages where the backbone carbonyl oxygen serves as a ligand for the K+ ions. Figures A) and C) are obtained from PDB file 1K4C[6].

Although the topology of KcsA is close to the inward rectifier K+ channels, it resembles K_v channels much more with regards to its ion permeability and selectivity[86]. The major difference between K_v channels and KcsA lies in the stimuli ligand required for activation of the channels: K_v channels are activated by membrane depolarisation, whereas KcsA activation is established by lowering pH[88,89]. The activity of K_v channels plays a key role in determining the duration, shape and characteristics of any kind of action potential in vertebrates[90]. Hence, gaining more insight in the mechanism underlying activation and inactivation of KcsA could contribute to understand the mechanism of K_v channels at the molecular level.
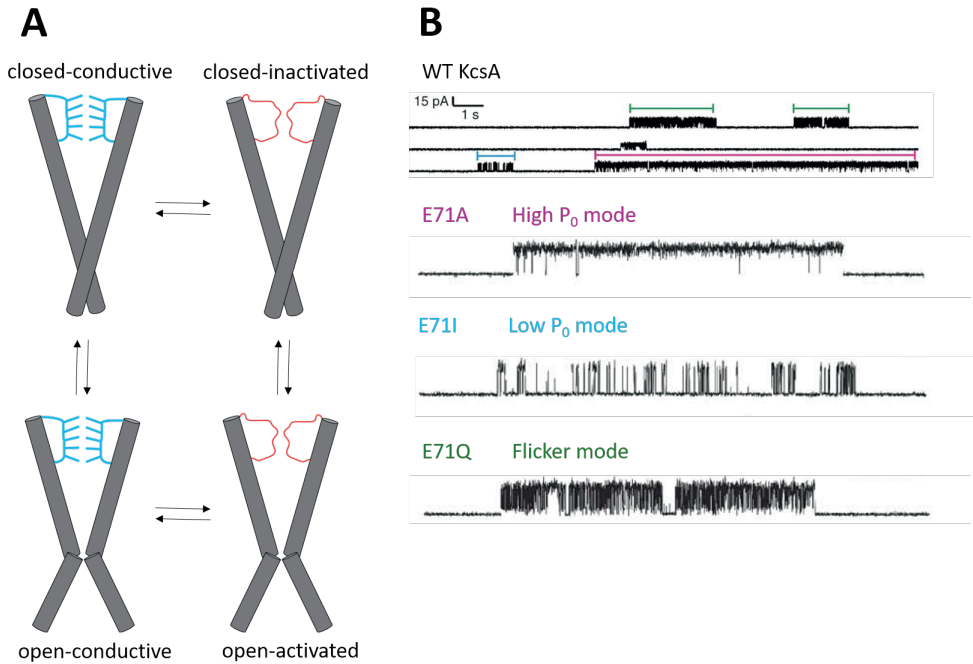
Figure 9. Modal gating behaviour in KcsA. A) The lower activation gate can be in an open or closed conformation and is tightly controlled by pH. The upper gate relates to the selectivity filter and transits between a conductive and inactivated state. B) Modal gating behaviour of KcsA recorded under steady-state conditions at pH 3.0 and 150 mV in 200 mM K^+ (top). Modal gating is dominated by the non-conductive C-type inactivated state with bursts of activity with variable kinetics behaviour. Representation of each gating mode captured with E71 mutants. Figure adapted from reference[7].

The activity of KcsA is governed by an interplay of the activation gate and the C-type inactivation gate. Opening and closing of the activation gate in KcsA is tightly controlled by protons. At neutral pH, the C-termini of the TM helices are held together through a network of hydrogen bonds that keep the channel in a closed conformation. When the pH is decreased to ~4, the key residues H25, E118 and E120 in the activation gate are protonated and the original hydrogen-bond network holding the bundle of helices together is disrupted[91,92]. As a result, the channel opens allowing the conduction of K^+ ions. Remarkably, conduction of K^+ ions decays in a time-dependent fashion even when the activation gate remains open. It was discovered that the transitions between conductive and nonconductive state of KcsA is dictated by the C-type inactivation gate[93]. This stochastic transition mechanism (Figure 9A) is also referred to as gating. In some K^+ channels these two mechanisms are coupled[94,95]. C-type inactivation is a slow inactivation process that is related to the SF and is initiated by a decrease in K^+ ion concentration[96].

Interestingly, KcsA gating is predominantly characterized by the nonconductive C-type inactivated state[96,97], which is abruptly and randomly interrupted by bursts of opening. These bursts display distinctly different kinetic modes[96]. So far, at least three different kinetic modes have been identified in KcsA with i) high open probability (high P_0), ii) low open probability mode (low P_0) and iii) a high frequency flicker mode[96] (Figure 9B). Random shifts between these gating modes are known as modal gating and are observed in many K^+ channels, yet the molecular origins are poorly understood.

Chakrapani and colleagues discovered that KcsA can be locked in intrinsically occurring 'modal gating' modes with E71X point-mutations[7]. The hydrogen-bond network between the triad W67-E71-D80 is critical for the activity of KcsA[7]. Interestingly, residues W67 and D80 are highly conserved in K^+ channels, whereas E71 is typically substituted by valine or isoleucine in eukaryotes. Mutating residue E71 to either alanine, isoleucine or glutamine locks KcsA in high P_0 state, low P_0 state or the flickering mode, respectively, facilitating the study of each mode independently[7]. Remarkably, crystal structures of the different E71 mutants, representing the different gating modes, revealed no structural differences and could not explain the distinct modal gating behaviours[7]. MD simulations suggested that changes in dynamics of the SF contribute to modal gating shifts[7], however, detailed experimental data on the SF were not available.

Altogether, the question on how the hydrogen-bond network between residues W67, E71 and D80 modulates gating behaviour of KcsA needs to be addressed to get a full understanding on the molecular determinants involved in the regulation of K^+ channels and modal gating. In Chapter 5, we explore the gating behaviour of KcsA by applying high-resolution ssNMR on WT KcsA and several E71X mutants including a mutant that mimics the eukaryotic SF. We reveal that motional shifts in the SF are of significant importance for modal gating of K^+ channels.

Scope of the thesis

The aim of the work presented here is to contribute to our current understanding of therapeutic peptides and membrane proteins, which are fundamental for future drug design. To achieve this, we have implemented modern ssNMR techniques on such systems in their native-like environment. In **Chapter 1** we have provided a brief outline on the principles of ssNMR and we introduce the three different systems that were explored with ssNMR.

In **Chapter 2** we present the first study on the antibiotic plectasin in complex with its target lipid II in lipid membranes. Combining solution and ssNMR data enabled us to identify structural elements that play an important role in lipid II binding. Our results also demonstrated that the plectasin – lipid II complex is significantly shaped by the membrane environment. In **Chapter 3**, we continued our structural study on the plectasin - lipid II complex. Using $^{15}N,^{13}C$-labelled lipid II we could for the first time experimentally investigate the complex interface. This enabled us to unravel the role of the lipid II sugar – pentapeptide head group in the complex. With modern ssNMR methods such as DNP we could demonstrate that plectasin oligomerizes upon lipid II binding, which was not observed before. Altogether, we could provide with critical insights in the plectasin – lipid II complex which allowed us to identify interesting hotspots for the rational design of novel antibiotics using plectasin as template.

In **Chapter 4** we exploit a series of peptidic hydrogels as potent scaffolds for tissue engineering of the spinal cord. Here, we show that ssNMR is a powerful tool for the characterization of mechanical properties of tissue engineering scaffolds at the atomic level with high resolution without the need of ^{13}C isotope-label enrichment. Our results also identified the scaffold heterogeneity as a, thus far, unknown crucial material parameter for the functionality of the scaffolds. Moreover, by integrating ssNMR and MD simulations, we succeeded to characterize the supramolecular organization of the hydrogels, which provided with new insights into the self-assembly procedure of the exploited peptides.

Chapter 5 focuses on the molecular determinants underlying modal gating behaviour in the K^+ channel KcsA. By combining ssNMR with MD simulations on different KcsA gating modes, we could, for the first time ever, show that conformational and motional changes, resulting from changes in selectivity filter dynamics, relate to the different modal gating shifts.

Finally, we discuss the contributions of ssNMR to our understanding of the plectasin – lipid II complex, peptidic hydrogels and modal gating behaviour in KcsA in **Chapter 6**.

References

1   nmr900.ca/testspectra_e.html.

2   Wylie, A. A. et al. The allosteric inhibitor ABL001 enables dual targeting of BCR–ABL1. Nature 543, 733 (2017).

3   Ashkenazi, A., Fairbrother, W. J., Leverson, J. D. & Souers, A. J. From basic apoptosis discoveries to advanced selective BCL-2 family inhibitors. Nature Reviews Drug Discovery 16, 273 (2017).

4   Erlanson, D. A., Fesik, S. W., Hubbard, R. E., Jahnke, W. & Jhoti, H. Twenty years on: the impact of fragments on drug discovery. Nature reviews Drug discovery 15, 605 (2016).

5   Kategaya, L. et al. USP7 small-molecule inhibitors interfere with ubiquitin binding. Nature 550, 534 (2017).

6   Zhou, Y., Morais-Cabral, J. H., Kaufman, A. & MacKinnon, R. Chemistry of ion coordination and hydration revealed by a K+ channel–Fab complex at 2.0 Å resolution. Nature 414, 43 (2001).

7   Chakrapani, S. et al. On the structural basis of modal gating behavior in K+ channels. Nature structural & molecular biology 18, 67 (2011).

8   Terstappen, G. C. & Reggiani, A. In silico research in drug discovery. Trends in pharmacological sciences 22, 23-26 (2001).

9   Drews, J. Drug discovery: a historical perspective. Science 287, 1960-1964 (2000).

10   Lowe, I. Phys Rev Lett 2: 285 (b) Andrew ER. Bradbury A, Eades RG (1959) Nature 183, 1802 (1959).

11   Narasimhan, S. et al. DNP supported solid-state NMR of proteins inside Mammalian Cells. Angewandte Chemie (2019).

12   Qiang, W., Yau, W.-M., Lu, J.-X., Collinge, J. & Tycko, R. Structural variation in amyloid-β fibrils from Alzheimer's disease clinical subtypes. Nature 541, 217 (2017).

13   Shi, C. et al. Atomic-resolution structure of cytoskeletal bactofilin by solid-state NMR. Science advances 1, e1501087 (2015).

14   Munowitz, M., Dobson, C., Griffin, R. & Harrison, S. On the rigidity of RNA in tomato bushy stunt virus. Journal of molecular biology 141, 327-333 (1980).

15   Andrew, E. & Eades, R. Removal of dipolar broadening of NMR spectra of solids by spectral rotation. Nature 1959, 183 (1802).

16   Lippens, G. et al. Study of compounds attached to solid supports using high resolution magic angle spinning NMR. Curr. Org. Chem 3, 147-169 (1999).

17   Kay, L. E., Torchia, D. A. & Bax, A. Backbone dynamics of proteins as studied by nitrogen-15 inverse detected heteronuclear NMR spectroscopy: application to staphylococcal nuclease. Biochemistry 28, 8972-8979 (1989).

18   Lewandowski, J. R., Sass, H. J. r., Grzesiek, S., Blackledge, M. & Emsley, L. Site-specific measurement of slow motions in proteins. Journal of the American Chemical Society 133, 16762-16765 (2011).

19   Gold, H. S. & Moellering Jr, R. C. Antimicrobial-drug resistance. New England journal of medicine 335, 1445-1453 (1996).

20   Walsh, C. Molecular mechanisms that confer antibacterial drug resistance. Nature 406, 775 (2000).

21   Cassini, A. et al. Attributable deaths and disability-adjusted life-years caused by infections with antibiotic-resistant bacteria in the EU and the European Economic Area in 2015: a population-level modelling analysis. The Lancet infectious diseases 19, 56-66 (2019).

22   Gandra, S., Barter, D. & Laxminarayan, R. Economic burden of antibiotic resistance: how much do we really know? Clinical microbiology and infection 20, 973-980 (2014).

23   Hancock, R. E. & Sahl, H.-G. Antimicrobial and host-defense peptides as new anti-infective therapeutic strategies. Nature biotechnology 24, 1551 (2006).

24   Breukink, E. & de Kruijff, B. Lipid II as a target for antibiotics. Nature reviews Drug discovery 5, 321 (2006).

25   Scheffers, D.-J. & Tol, M. B. LipidII: just another brick in the wall? PLoS pathogens 11, e1005213 (2015).

26   Levine, D. P. Vancomycin: a history. Clinical infectious diseases 42, S5-S12 (2006).

27   Williams, D. H. & Waltho, J. P. Molecular basis of the activity of antibiotics of the vancomycin group. Biochem. Pharmacol 37, 133-141 (1988).

28   Sheldrick, G. M., Jones, P. G., Kennard, O., Williams, D. H. & Smith, G. A. Structure of vancomycin and its complex with acetyl-D-alanyl-D-alanine. Nature 271, 223 (1978).

29   Chang, S. et al. Infection with vancomycin-resistant Staphylococcus aureus containing the vanA resistance gene. New England journal of medicine 348, 1342-1347 (2003).

30   Brötz, H. et al. Role of lipid-bound peptidoglycan precursors in the formation of pores by nisin, epidermin and other lantibiotics. Molecular microbiology 30, 317-327 (1998).

31   Breukink, E. et al. Use of the cell wall precursor lipid II by a pore-forming peptide antibiotic. Science 286, 2361-2364 (1999).

32   Medeiros-Silva, J. et al. High-resolution NMR studies of antibiotics in cellular membranes. Nature communications 9 (2018).

33   Ganz, T. Defensins: antimicrobial peptides of innate immunity. Nature reviews immunology 3, 710 (2003).

34   Tang, Y.-Q. et al. A cyclic antimicrobial peptide produced in primate leukocytes by the ligation of two truncated α-defensins. Science 286, 498-502 (1999).

35   Lehrer, R. I. & Ganz, T. Defensins of vertebrate animals. Current opinion in immunology 14, 96-102 (2002).

36   Zhu, S. Discovery of six families of fungal defensin-like peptides provides insights into origin and evolution of the CSαβ defensins. Molecular immunology 45, 828-838 (2008).

37   Mygind, P. H. et al. Plectasin is a peptide antibiotic with therapeutic potential from a saprophytic fungus. Nature 437, 975 (2005).

38   Schneider, T. et al. Plectasin, a fungal defensin, targets the bacterial cell wall precursor Lipid II. Science 328, 1168-1172 (2010).

39   Oeemig, J. S. et al. Eurocin, a new fungal defensin structure, lipid binding, and its mode of action. Journal of Biological Chemistry 287, 42361-42372 (2012).

40   Essig, A. et al. Copsin, a novel peptide-based fungal antibiotic interfering with the peptidoglycan synthesis. Journal of Biological Chemistry 289, 34953-34964 (2014).

41   Schmitt, P. et al. Insight into invertebrate defensin mechanism of action oyster defensins inhibit peptidoglycan biosynthesis by binding to lipid II. Journal of Biological Chemistry 285, 29208-29216 (2010).

42   Yang, Y.-S. et al. Solution structure and activity of the synthetic four-disulfide bond Mediterranean mussel defensin (MGD-1). Biochemistry 39, 14436-14447 (2000).

43   Cui, H., Webber, M. J. & Stupp, S. I. Self-assembly of peptide amphiphiles: From molecules to nanostructures to biomaterials. Peptide Science: Original Research on Biomolecules 94, 1-18 (2010).

44   Andes, D., Craig, W., Nielsen, L. & Kristensen, H. In vivo pharmacodynamic characterization of a novel plectasin antibiotic, NZ2114, in a murine infection model. Antimicrobial agents and chemotherapy 53, 3003-3009 (2009).

45   Dominguez, C., Boelens, R. & Bonvin, A. M. HADDOCK: a protein– protein docking approach based on biochemical or biophysical information. Journal of the American Chemical Society 125, 1731-1737 (2003).

46   Münch, D. et al. Identification and in vitro analysis of the GatD/MurT enzyme-complex catalyzing lipid II amidation in Staphylococcus aureus. PLoS pathogens 8, e1002509 (2012).

47   Jones, B. & Bes, M. Keeping kidneys: most countries struggle to meet the demand for transplant kidneys, but a few are reaping the benefits of systems dedicated to increasing the number of organ donations after death. Bulletin of the World Health Organization 90, 718-720 (2012).

48   Arshad, A., Anderson, B. & Sharif, A. Comparison of organ donation and transplantation rates between opt-out and opt-in systems. Kidney international 95, 1453-1460 (2019).

49   Wood, K. J. & Goto, R. Mechanisms of rejection: current perspectives. Transplantation 93, 1-10 (2012).

50   Lanza, R., Langer, R. & Vacanti, J. P. Principles of tissue engineering. (Academic press, 2011).

51   Cohen, S. et al. Design of synthetic polymeric structures for cell transplantation and tissue engineering. Clinical materials 13, 3-10 (1993).

52   Witten, C. M., McFarland, R. D. & Simek, S. L. Concise review: the US Food and Drug Administration and regenerative medicine. Stem cells translational medicine 4, 1495-1499 (2015).

53   Mao, A. S. & Mooney, D. J. Regenerative medicine: current therapies and future directions. Proceedings of the National Academy of Sciences 112, 14452-14459 (2015).

54   Bailey, A. M., Mendicino, M. & Au, P. An FDA perspective on preclinical development of cell-based regenerative medicine products. Nature biotechnology 32, 721 (2014).

55   Wichterle, O. & Lim, D. Hydrophilic gels for biological use. Nature 185, 117-118 (1960).

56   Tibbitt, M. W. & Anseth, K. S. Hydrogels as extracellular matrix mimics for 3D cell culture. Biotechnology and bioengineering 103, 655-663 (2009).

57   Hughes, C. S., Postovit, L. M. & Lajoie, G. A. Matrigel: a complex protein mixture required for optimal growth of cell culture. Proteomics 10, 1886-1890 (2010).

58   Shin, H., Jo, S. & Mikos, A. G. Biomimetic materials for tissue engineering. Biomaterials 24, 4353-4364 (2003).

59   Burdick, J. A. & Anseth, K. S. Photoencapsulation of osteoblasts in injectable RGD-modified PEG hydrogels for bone tissue engineering. Biomaterials 23, 4315-4323 (2002).

60   Lee, J., Cuddihy, M. J. & Kotov, N. A. Three-dimensional cell culture matrices: state of the art. Tissue Engineering Part B: Reviews 14, 61-86 (2008).

61   Gelain, F., Bottai, D., Vescovi, A. & Zhang, S. Designer self-assembling peptide nanofiber scaffolds for adult mouse neural stem cell 3-dimensional cultures. PloS one 1, e119 (2006).

62   Silva, G. A. et al. Selective differentiation of neural progenitor cells by high-

epitope density nanofibers. Science 303, 1352-1355 (2004).

63   Galler, K. M. et al. Self-assembling peptide amphiphile nanofibers as a scaffold for dental stem cells. Tissue Engineering Part A 14, 2051-2058 (2008).

64   Beniash, E., Hartgerink, J. D., Storrie, H., Stendahl, J. C. & Stupp, S. I. Self-assembling peptide amphiphile nanofiber matrices for cell entrapment. Acta biomaterialia 1, 387-397 (2005).

65   Narmoneva, D. A. et al. Self-assembling short oligopeptides and the promotion of angiogenesis. Biomaterials 26, 4837-4846 (2005).

66   Moore, A. N. & Hartgerink, J. D. Self-assembling multidomain peptide nanofibers for delivery of bioactive molecules and tissue regeneration. Accounts of chemical research 50, 714-722 (2017).

67   Arab, W., Rauf, S., Al-Harbi, O. & Hauser, C. A. Novel ultrashort self-assembling peptide bioinks for 3D culture of muscle myoblast cells. Int J Bioprint 4, 129 (2018).

68   Zhang, S., Holmes, T., Lockshin, C. & Rich, A. Spontaneous assembly of a self-complementary oligopeptide to form a stable macroscopic membrane. Proceedings of the National Academy of Sciences 90, 3334-3338 (1993).

69   Zhang, S., Lockshin, C., Herbert, A., Winter, E. & Rich, A. Zuotin, a putative Z-DNA binding protein in Saccharomyces cerevisiae. The EMBO journal 11, 3787-3796 (1992).

70   Zhang, S. et al. Self-complementary oligopeptide matrices support mammalian cell attachment. Biomaterials 16, 1385-1393 (1995).

71   Saracino, G. A. A. & Gelain, F. Modelling and analysis of early aggregation events of BMHP1-derived self-assembling peptides. Journal of Biomolecular Structure and Dynamics 32, 759-775 (2014).

72   Gelain, F. et al. BMHP1-derived self-assembling peptides: hierarchically assembled structures with self-healing propensity and potential for tissue engineering applications. ACS nano 5, 1845-1859 (2011).

73   Silva, D. et al. Synthesis and characterization of designed BMHP1-derived self-assembling peptides for tissue engineering applications. Nanoscale 5, 704-718 (2013).

74   Discher, D. E., Janmey, P. & Wang, Y.-l. Tissue cells feel and respond to the stiffness of their substrate. Science 310, 1139-1143 (2005).

75   Chowdhury, F. et al. Material properties of the cell dictate stress-induced spreading and differentiation in embryonic stem cells. Nature materials 9, 82 (2010).

76   Pouyani, T., Harbison, G. S. & Prestwich, G. D. Novel hydrogels of hyaluronic acid: synthesis, surface morphology, and solid-state NMR. Journal of the American Chemical Society 116, 7515-7522 (1994).

77   Dorkoosh, F. et al. Preparation and NMR characterization of superporous hydrogels (SPH) and SPH composites. Polymer 41, 8213-8220 (2000).

78   Labokha, A. A. et al. Systematic analysis of barrier-forming FG hydrogels from Xenopus nuclear pore complexes. The EMBO journal 32, 204-218 (2013).

79   Littleton, J. T. & Ganetzky, B. Ion channels and synaptic organization: analysis of the Drosophila genome. Neuron 26, 35-43 (2000).

80   Kuo, M. M.-C., Haynes, W. J., Loukin, S. H., Kung, C. & Saimi, Y. Prokaryotic K+ channels: from crystal structures to diversity. FEMS microbiology reviews 29, 961-985 (2005).

81   Yellen, G. The voltage-gated potassium channels and their relatives. nature 419, 35 (2002).

82   Hille, B. Ion channels of excitable membranes. Sinauer Associates. Sunderland,

MA 1375 (2001).

83   Sansom, M. S. et al. Potassium channels: structures, models, simulations. Biochimica et Biophysica Acta (BBA)-Biomembranes 1565, 294-307 (2002).

84   Shieh, C.-C., Coghlan, M., Sullivan, J. P. & Gopalakrishnan, M. Potassium channels: molecular defects, diseases, and therapeutic opportunities. Pharmacological reviews 52, 557-594 (2000).

85   Parekh, P. K. et al. Antimanic Efficacy of a Novel Kv3 Potassium Channel Modulator. Neuropsychopharmacology 43, 435 (2018).

86   Doyle, D. A. et al. The structure of the potassium channel: molecular basis of K+ conduction and selectivity. science 280, 69-77 (1998).

87   Morais-Cabral, J. H., Zhou, Y. & MacKinnon, R. Energetic optimization of ion conduction rate by the K+ selectivity filter. Nature 414, 37 (2001).

88   Heginbotham, L., LeMasurier, M., Kolmakova-Partensky, L. & Miller, C. Single Streptomyces lividans K+ channels: functional asymmetries and sidedness of proton activation. The Journal of general physiology 114, 551-560 (1999).

89   LeMasurier, M., Heginbotham, L. & Miller, C. KscA: it's an ion channel. J Gen Physiol 118, 303-314 (2001).

90   Fedida, D. & Hesketh, J. C. Gating of voltage-dependent potassium channels. Progress in biophysics and molecular biology 75, 165-199 (2001).

91   Thompson, A. N., Posson, D. J., Parsa, P. V. & Nimigean, C. M. Molecular mechanism of pH sensing in KcsA potassium channels. Proceedings of the National Academy of Sciences 105, 6900-6905 (2008).

92   Imai, S., Osawa, M., Takeuchi, K. & Shimada, I. Structural basis underlying the dual gate properties of KcsA. Proceedings of the National Academy of Sciences 107, 6216-6221 (2010).

93   Perozo, E., Marien, D. & Cuello, L. G. Structural rearrangements underlying K+-channel activation gating. Science 285, 73-78 (1999).

94   Loots, E. & Isacoff, E. Protein rearrangements underlying slow inactivation of the Shaker K+ channel. The Journal of general physiology 112, 377-389 (1998).

95   Olcese, R., Latorre, R., Toro, L., Bezanilla, F. & Stefani, E. Correlation between charge movement and ionic current during slow inactivation in Shaker K+ channels. The Journal of general physiology 110, 579-589 (1997).

96   Chakrapani, S., Cordero-Morales, J. F. & Perozo, E. A quantitative description of KcsA gating I: macroscopic currents. The Journal of general physiology 130, 465-478 (2007).

97   Cordero-Morales, J. F. et al. Molecular determinants of gating at the potassium-channel selectivity filter. Nature structural & molecular biology 13, 311 (2006).

CHAPTER 2

High-resolution ssNMR study of the
plectasin - lipid II complex in membranes

Abstract

The alarming rise of multi-drug resistant bacteria is a major threat to human health. It is hence of pressing need to develop novel antibiotics that operate via unexploited mechanisms and that are robust to resistance development. Ideal templates for such next-generation drugs could be peptide antibiotics that destroy the bacterial cell wall by binding to its essential membrane-anchored precursor lipid II at an irreplaceable pyrophosphate group. However, our molecular understanding of lipid II binding drugs is scarce and structural data in physiologically relevant conditions are absent. Here, using solid-state NMR methods, we report the first high-resolution study of the peptide-antibiotic plectasin in complex with lipid II in lipid membranes. Our study provides important new insights into plectasin's mode of action and highlights the critical influence of the membrane environment. We expect our study to open new avenues for the design of novel and improved antibiotics.

Introduction

Antimicrobial resistance is a growing threat to human health worldwide. High-profile reports have predicted the devastating consequences of antimicrobial resistance on the public health and global economy unless novel intervention strategies are mounted[1]. The need for novel antibiotics that act via unexploited mechanisms and that are robust to resistance developments has become imperative. Ideal templates for such drugs could be antimicrobial peptides that interfere with the biosynthesis of the bacterial cell wall by targeting the essential membrane-anchored precursor lipid II at an irreplaceable pyrophosphate group[3]. Such antibiotic peptides, including nisin[4,5], tridecaptin[6] and the recently discovered teixobactin[7], indeed kill persistent bacteria at nanomolar concentrations without detectable resistance and with no signs of cytotoxicity towards mammalian cells[8]. Hence, such peptides could form a new generation of clinically useful drugs. However, due to challenges that are presented in studying small membrane-embedded drug-receptor complexes in biological membranes, the structural correlate of medically relevant binding modes remains unknown. This lack of knowledge forms a major limitation for the rational design of novel antibiotics.

A particularly promising class of lipid II binding antimicrobial peptides are defensins. Defensins are small cysteine-rich host defence peptides that are part of the innate immune system in vertebrate and invertebrate animals, fungi and plants. Interestingly, it was reported that a class of defensins, the so-called CSαβ defensins, specifically target lipid II and thereby kill bacteria by blocking the cell wall synthesis. CSαβ defensins share a common fold where an α-helix is connected to a short β-sheet via several disulfide bridges. Due to their high structural resemblance, understanding the lipid II binding mode of CSαβ defensins is of broad pharmaceutical importance[9]. The best studied CSαβ defensin is plectasin from the fungus *Pseudoplectania nigrella*[2,4]. Plectasin and its improved derivative NZ2114 show activity against a broad range of bacteria including medically high relevant pathogens such as methicillin resistant *Staphylococcus aureus* (MRSA) and *Streptococcus pneumoniae*[2,10]. Moreover, plectasin is active in animal models, which are often a bottleneck in many drug design studies. This makes it an attractive candidate for clinical use, however, also in this case structural information in relevant media is absent. The only available model for the plectasin – lipid II complex comes from docking studies based on solution NMR chemical shift perturbations derived from micelles, where the lipid II binding site was identified as F2, G3, C4 and C37[4] (Figure 1A).

Plectasin is typically isolated from its natural producer or is chemically synthesized. However, these approaches are often complex and costly, especially when isotope labelling is required. The *Escherichia coli* expression system is a cost-effective and a simple alternative for the production of plectasin[11].

Nonetheless, many *E. coli* strains have a reduced cytoplasmic environment, which complicates the folding of plectasin. Therefore, a downstream complex refolding step is required when using such strains[11]. Here, we express ^{13}C, ^{15}N-labelled plectasin in *E. coli* Shuffle® cells, which is a strain that enables the formation of disulfide bridges in the cytoplasm and hence makes the downstream refolding of plectasin unnecessary.

In this study, we use ^{1}H-detected solid-state NMR (ssNMR)[12-14] to report the first high-resolution study of the plectasin – lipid II complex in lipid membranes. We analyse the structure and dynamics of bound and unbound plectasin in detail and discover new structural elements of plectasin that are critical for lipid II binding in lipid membranes. In addition, in Chapter 3 we use isotope labelled lipid II to experimentally illustrate the complex interface in membranes and identify, thus far, unknown key residues that are involved in lipid II binding. Therefore, our study highlights the critical importance of the physiological environment for the mode of action of lipid II binding antibiotics. Finally, we demonstrate with plectasin mutants that our insights enable the rational design of antibiotics against multi-drug resistant pathogens.

Results and Discussion

Recombinantly produced plectasin is correctly folded

Plectasin is the first isolated CSaβ defensin that targets lipid II[4] and has potential as antibiotic (Figure 1A). However, a simple and cost-effective protocol for the production of isotope labelled plectasin without the need of additional refolding procedures has yet to be established. Here, we expressed plectasin fused to SUMO in *E. coli* Shuffle® cells on minimal M9 medium supplemented with 0.5 g/L ^{15}NH$_4$Cl and 2.0 g/L ^{13}C-glucose (Figure 1B). Pure plectasin was yielded after a first purification (affinity chromatography), subsequently followed by cleavage of the SUMO protein and a second purification (gel filtration) (Figure 1B). We used solution NMR to investigate the structure of the recombinantly produced plectasin. First, we assigned the ^{1}H, ^{13}C and ^{15}N chemical shifts of free plectasin (Table S1) in solution and subsequently studied its structure (Figure 1C, D). The assignments were carried out *de novo* since previous studies[2,4] did not include ^{13}C labels. A [Cα-Cβ] secondary chemical shift (SCS)[15] analysis clearly showed the signature CSαβ-fold of plectasin, formed by α-helix D12-I22 and β-sheet G28-A31 – V36-C39 (Figure 1D). Interestingly, we discovered the presence of a further β-sheet like structure in the long N-terminal loop, which is not present in other lipid II-targeting CSαβ defensins[16], and which is assumed to form part of the lipid II binding site[4]. Moreover, the recombinantly produced ^{13}C, ^{15}N-labelled plectasin showed minimum inhibitory concentration (MIC) values against *Streptococcus pyogenes*, *Streptococcus pneumoniae* and *Staphylococcus*

aureus that are comparable to previously reported values[2,4](Figure 1E). These findings validate the use of the *E. coli* Shuffle® strain for the production of disulfide-containing antimicrobial peptides with conserved structure and activity.
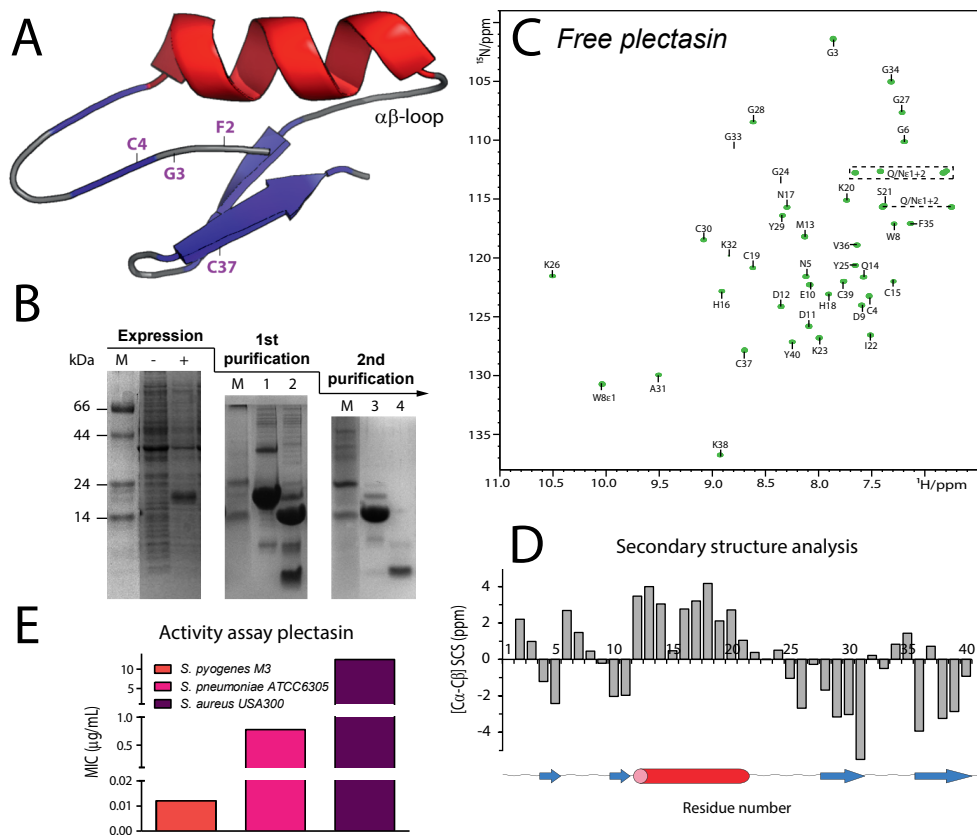
Figure 1. A) The peptide antibiotic plectasin kills bacteria by tightly binding and sequestering the peptidoglycan precursor lipid II. Previously reported studies identified the lipid II binding site of plectasin as F2, G3, C4 and mainly C37 (indicated in magenta). B) *Expression* SDS-PAGE analysis of protein expression induced with 0.5 mM IPTG for 4 hours at 37°C. Lane M contains protein marker, lane – negative control where no expression was induced and lane + the overexpression product of the petSUMO – plectasin plasmid (± 18 kDa). *1st purification* SDS-PAGE analysis of the purification of the recombinant fusion protein. Lane M contains marker, lane 1 contains the fusion protein after purification by affinity chromatography, lane 2 shows cleavage of SUMO from plectasin by SUMO protease (Ulp1). *2nd purification* SDS page analysis of purification of plectasin. Lane M contains marker, lane 3 and 4 contain fractions collected after gel filtration containing SUMO (±14 kDa) and plectasin (±4.4 kDa), respectively. C) Solution NMR 2D ^{15}N – ^{1}H spectrum of free plectasin, acquired at 900 MHz magnetic field (^{1}H-frequency). D) [Cα-Cβ] secondary chemical shifts (SCS) show the signature CSαβ fold of plectasin and an extended structural element in the N-terminal loop. Helical and extended residues are coloured in red and blue in the structure (1zfu[2]), respectively. E) Activity assay of plectasin with minimal inhibitory concentrations (MIC) of 0.012, 0.78 and 12.5 μg/mL for *S. pyogenes M3* (orange), *S. pneumoniae ATCC6305* (pink) and *S. aureus USA300*, respectively. Note that the measured MIC values were in good agreement with previously published data[2,4].

Dynamics measurements show conformational exchange for residues in αβ-loop

Next, we investigated the relaxation rates of ^{15}N nuclei of free plectasin in solution to probe the local dynamics of the unbound antibiotic peptide (Figure 2A-C). Residues G24 and G33 were discarded in the analysis due to very low peak intensities.

As expected, plectasin has a fairly rigid backbone which can be deduced from the high average heteronuclear NOE value of 0.76±0.09. This is clearly due to the presence of disulfide bridges that stabilise the characteristic fold of plectasin. Interestingly, while the R_1 rates are very uniform for plectasin, increased R_2 values and starkly enhanced R_2/R_1 ratios are observed for residues I22 and K23 of the aβ-loop which connects the helix and the first β-strand (Figure 2D). These data strongly suggest that the αβ-loop undergoes slow conformational exchange. Moreover, significant differences between the ^{15}N R_2 rates determined from both CPMG and $R_{1\rho}$ measurements were found for I22 and K23 further validating contributions from conformational exchange (Figure S1). Elevated R_2 rates and R_2/R_1 ratios were also detected for neighbouring residues H16 to S21 in the α-helix, suggesting that part of the helix is also involved in conformational exchange. These findings identify structural features of plectasin that display distinct motional behaviour that might be of critical importance for lipid II binding characteristics.
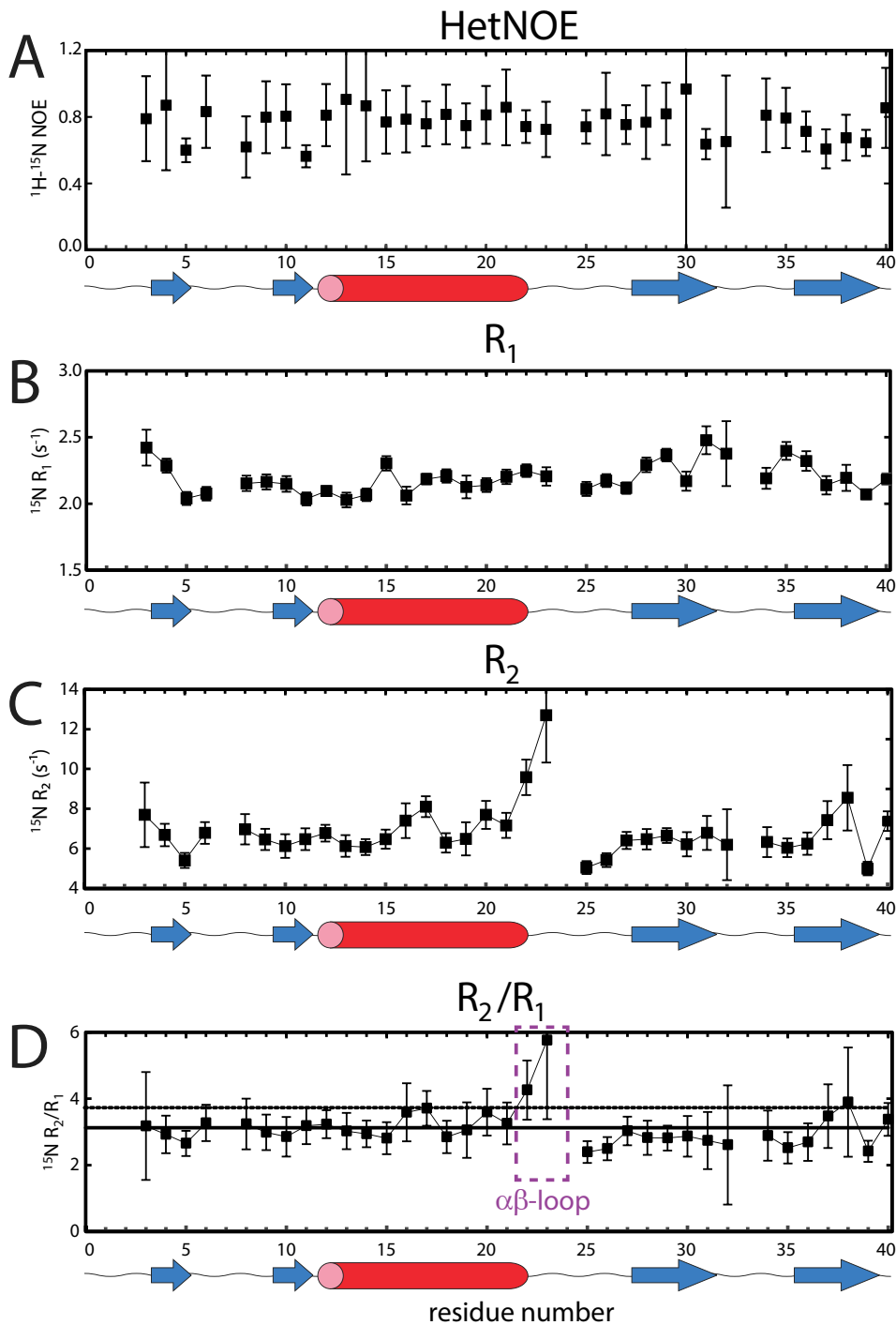
Figure 2. Solution NMR relaxation data showing A) Heteronuclear NOE (HetNOE), B) R_1, C) R_2, and D) R_2/R_1 values of free plectasin. The compact disulfide-bridge stabilised

plectasin is globally very rigid. However, unlike the rest of the peptide, residues of the αβ-loop showed highly increased R_2 relaxation rates and R_2/R_1 ratio, typically a sign for increased micro- to millisecond dynamics. Secondary structure elements are indicated on the bottom.

The plectasin – lipid II complex in lipid membranes as seen by ssNMR

We explored the plectasin – lipid II complex in lipid membranes using ssNMR spectroscopy. Therefore, we co-assembled the plectasin – lipid II complex at a 2:1 molar ratio in DOPC liposomes to ensure saturation of lipid II. Plectasin targets specifically lipid II with high affinity (binding constant $1.8 \cdot 10^{-7}$ mol)[4]. Indeed, we verified with fluorescence spectroscopy that plectasin strongly binds to our lipid II containing liposomes, whereas no binding could be detected to empty liposomes (Figure S2). Hence, our ssNMR spectra include only lipid II – bound plectasin. We first acquired a ^{1}H-detected dipolar-based spectrum of fully-protonated[17] ^{13}C, ^{15}N-labelled plectasin in complex with lipid II, acquired at fast (60 kHz) magic angle spinning (MAS) frequency (Figure 3A). The spectrum is well-resolved, and features signals as narrow as 0.19 ppm (Figure S3), implying a well-defined complex. We assigned bound plectasin using 3D CαNH, 3D Cα(CO)NH and CO(Cα)NH ssNMR experiments in combination with a 2D ^{13}C-^{13}C PARIS[18,19] experiment (Figure 3B, C) and our solution NMR chemical shifts. We could ambiguously assign 39 out of 40 residues (Table S2).

NMR chemical shifts are highly sensitive to changes in hydrogen bonding and peptide conformation. Therefore, comparing the chemical shifts of bound and free plectasin provides atomic-level information on the lipid II binding site (Figure 3D). Since plectasin is assumed to bind lipid II via hydrogen bonds[4], chemical shift perturbations (CSPs) of the amino protons (H^N) are of particular importance to locate binding spots. Based on strong CSPs, C37 was identified as the primary binding site for lipid II in micelles[4]. Indeed, the largest CSPs in membranes were also observed for C37. However, unlike previously published data, we observed stark chemical shift differences across the whole peptide, hence CSPs data only does not provide with solid evidence for the lipid II binding site. The chemical shift deviations between micelles and membranes also suggest that the CSP-based docking model[4] of the plectasin – lipid II complex might not reflect the physiologically relevant state. Besides C37, we also obtained high CSPs for G28 which has no role in lipid II binding in micelles. Remarkably, both G28 and C37 show stark heterogeneity, which can be readily deduced by the broad signals corresponding to the residues, implying that plectasin has a certain conformational plasticity to bind to lipid II in membranes. This could be an important feature to adapt to the subtle modifications that the pentapeptide-sugar moiety of lipid II experiences across bacterial strains[20]. Intriguingly, we also observe enhanced CSPs for D12 and K23 which virtually showed no CSPs

in the plectasin – lipid II complex in micelles[4]. Here also, these differences show that plectasin has a deviating mode of action in lipid membranes compared to micelles.

While H^N CSPs are sensitive to hydrogen bonding, CSPs of [Cα-Cβ] SCS report on conformational changes (Figure 3E). Globally, the ΔSCS profile that compares the structure of bound and unbound plectasin reveals that the CSαβ-fold of plectasin is conserved in the complex. As a direct effect of lipid II binding, the β-sheet is globally stabilised, as evidenced by the intensely negative [Cα-Cβ] ΔSCSs for residues C30 and A31, respectively. Remarkably, negative [Cα-Cβ] ΔSCSs for S21 and I22 (-0.77 and -1.39 ppm) show a conformational change in line with a shortening of the α-helix by two residues in the complex (Figure 3E, F). As a consequence, the αβ-loop shows large [Cα-Cβ] ΔSCSs from K23 to G27, signifying substantial conformational changes upon complex formation. Importantly, this result is in line with the strongly enhanced R_2/R_1 relaxation ratios observed in solution NMR for residues in the α-helix and the αβ-loop (Figure 2D), a typical sign for conformational plasticity.

2
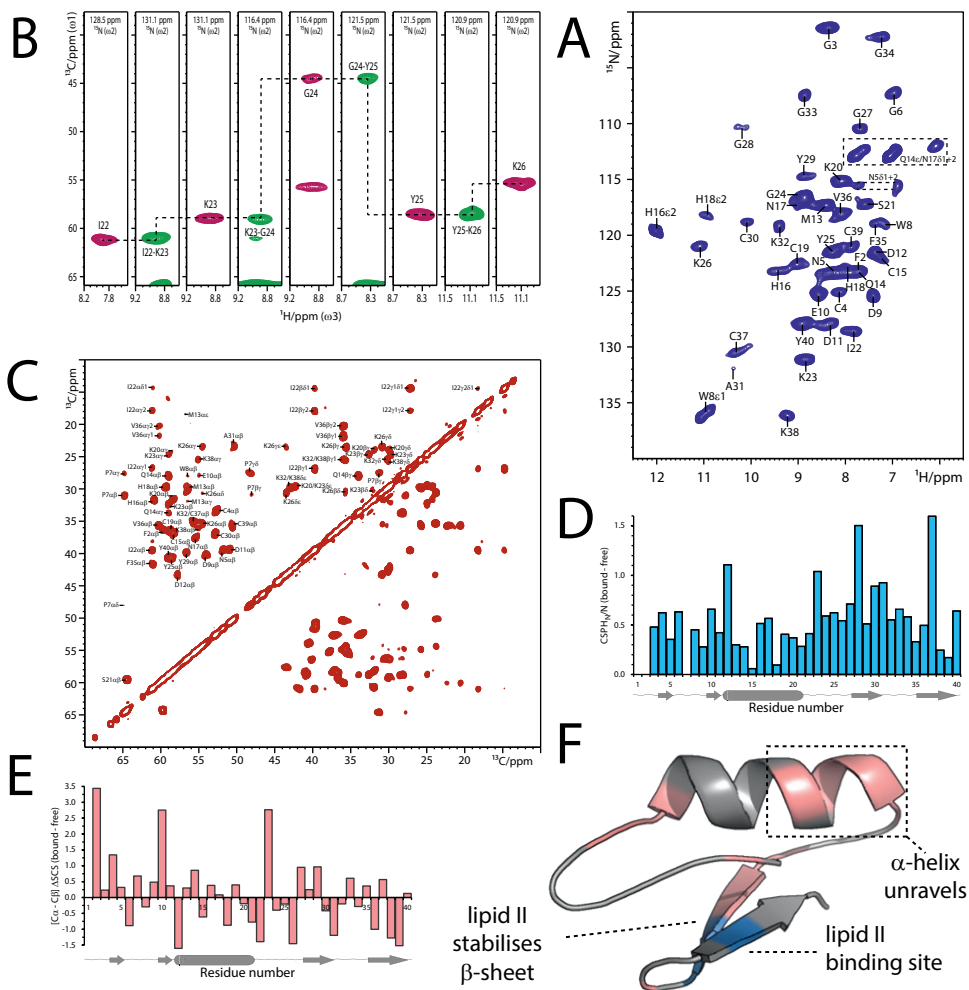
Figure 3. A) [1]H-detected 2D [15]N – [1]H spectrum of plectasin bound to lipid II in liposomes, acquired at 700 MHz magnetic field ([1]H-frequency) and 60 kHz MAS. Histidine side chain signals are back folded. B) ^{1}H-detected solid-state NMR assignments in lipid membranes of plectasin residues I22 – K26 of the αβ-loop in the lipid II – bound state. Strip plots are shown for 3D CαNH (magenta) and Cα(CO)NH (green) experiments. C) 2D [13]C – [13]C PARIS spectrum of the lipid II – bound plectasin acquired at 950 MHz, 18 kHz MAS and with 20 ms [13]C – [13]C mixing time D) Comparison of the chemical shifts of bound and free plectasin for the amino protons H[N]. E) Comparison of [Cα-Cβ] secondary chemical shifts (SCS) of bound and free plectasin. F) The influence of lipid II binding is illustrated on the plectasin structure. Blue and pink represent H[N] CSPs and [Cα-Cβ] ΔSCS, respectively.

Dynamics of plectasin in complex with lipid II

To further characterise the mode of action of plectasin, we measured the dynamics of the drug-receptor complex. Understanding the dynamics is of high importance for drug design, since conformational plasticity and the entropic contribution can be decisive for binding affinity[21]. Moreover, site-resolved dynamics studies can shed further light on the lipid II binding site. We measured site-resolved ^{15}N R_1 and $R_{1\rho}$ relaxation rates using ^1H-detected measurements at 60 kHz MAS (Figure 4A, B)[22,23]. These experiments report on fast nanosecond (R_1) and slow nano-to-microsecond ($R_{1\rho}$) motions. In general, the disulfide-stabilised plectasin is very rigid in the complex. The most rigid residues on both fast and slow timescales were G28, Y29, C37, and K38. This analysis shows a clear rigidification of the β-sheet in the lipid II bound state. As expected, loops, with G6, D9 and E10 of the N-terminal loop and G33 and G34 in the loop between the β-strands, showed increased conformational flexibility. In stark contrast, the relatively long αβ-loop I22 – G27 showed no enhanced dynamics and was virtually as rigid as the secondary structural elements. This was unexpected as no functional role has been described before for the αβ-loop. Surprisingly, the loop is neither near to the lipid II binding site nor is it close to the membrane in the published micelle model.
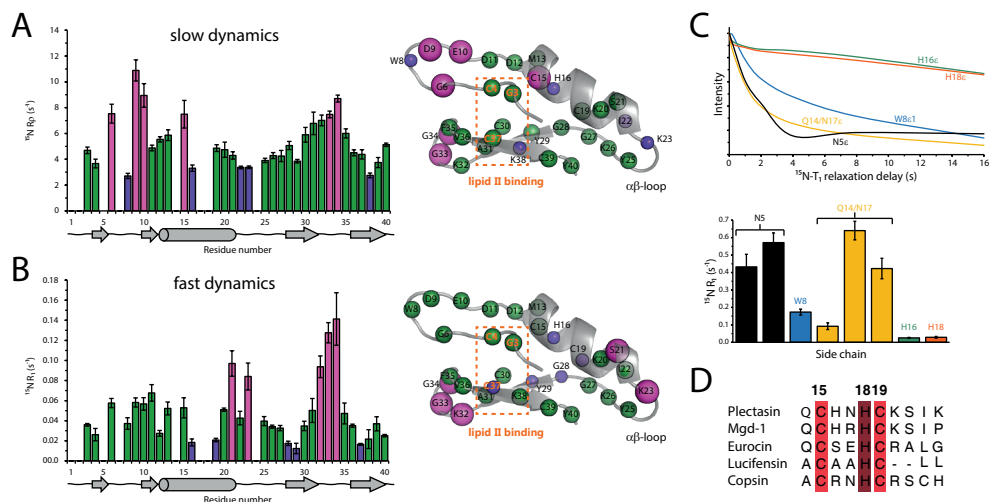
Figure 4. SSNMR dynamics of plectasin in complex with lipid II. A) ^{15}N $R_{1\rho}$ relaxation rates reporting on slow molecular motion, measured at 800 MHz and 60 kHz. Error bars show the standard error of the fit. Relaxation rates are illustrated on the structure of plectasin. Analysed residues are shown as color-coded spheres whose size is proportional to $R_{1\rho}$. B) ^{15}N R_1 rates, acquired at 800 MHz and 60 kHz MAS. The R_1 rates are illustrated on the structure. D) ^{15}N R_1 side chain dynamics. E) Alignment of lipid II binding CSαβ defensins. H18, among cysteine and glycine residues, is conserved among the CSαβ defensins.
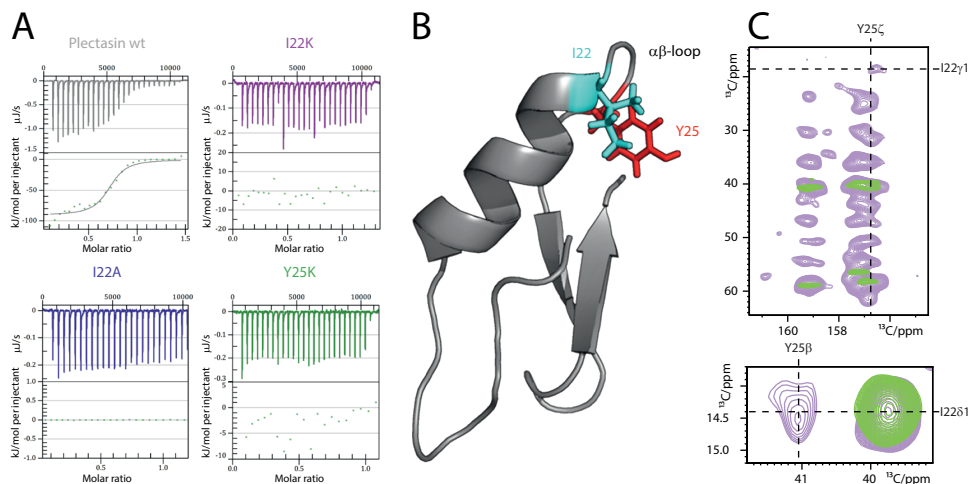
Figure 5. A) Isothermal Titration Calorimetry (ITC) data of plectasin wt (grey), I22K (purple), I22A (blue) and Y25K (green) with lipid II-doped DOPC vesicles. Data shows that I22 and Y25 mutants can no longer bind to lipid II. B) I22 and Y25 tightly interact to form a "stapler-like" conformation that is crucial for the activity of plectasin. C) ^{13}C-^{13}C spin diffusion spectra show clear interresidual contacts between I22 and Y25, validating our hypothesis on the tight interaction between these residues. Spectra were acquired at 950 MHz and 18 kHz MAS with 62 ms (green) and 600 ms (purple) mixing time.

To examine the functional aspect of the αβ-loop, we used mutational studies in combination with killing assays and Isothermal Titration Calorimetry (ITC). We mutated the long hydrophobic residues I22(A/K) and Y25(K). For each mutant, we verified the integrity of the CSαβ-fold with solution NMR (Figure S4A). Interestingly, all three mutations drastically reduced the activity of plectasin (Table S3). ITC data further showed that these mutants no longer bind to lipid II, clearly demonstrating the hitherto overlooked importance of this loop for the efficacy of plectasin (Figure 5A). Since the αβ-loop is not involved in membrane-anchoring, which we further confirm in Chapter 3, we therefore hypothesized that I22 and Y25 interact to form a "stapler-like" conformation that allosterically modulates the binding mode of plectasin (Figure 5B). Spin diffusion spectra, with long-mixing times, validate our hypothesis as we observed clear interactions between I22 and Y25 (Figure 5C). This is the first study to report on such "stapler-like" conformation in plectasin, and considering the high structural homology it is most likely conserved among the CSαβ defensins. We are currently thoroughly validating the stapling interaction with additional mutational studies.

The 2D NH spectra also enabled us to analyse side-chain dynamics (Figure 4C). The among CSαβ defensins conserved residue H18 has led to widespread assumption that it directly binds to residue E2 of the pentapeptide of lipid II, which was corroborated in docking studies[4], MD simulations[24] and mutational

studies[25]. All these studies assumed that H18 is positively charged, which strongly influenced the binding mode[24]. However, thus far, no experimental evidence is available that H18 is directly involved in lipid II binding, and the H18 side chain was unobservable in the plectasin – lipid II complex in micelles[4]. In liposomes, we clearly do observe histidine side chain signals (Figure S4B), which appear at 167 ^{15}N ppm. Strikingly, we did not observe an additional side chain signal for H18, which would typically appear at 170-190 ^{15}N ppm if indeed the side chain is protonated. Furthermore, the unprotonated ^{15}N signal was observed at ~230 ^{15}N ppm in CP spectra (data not shown), meaning that H18 is neutral in the complex at physiological pH[26] and not cationic as previously assumed. Hence, the previously reported structural data on the plectasin – lipid II complex are insubstantial. In our ^{15}N relaxation measurements (Figure 4C), the side chain signals of N5, W8, Q14 and N17 relaxed very rapidly (R$_1$ 0.09 – 0.64 s^{-1}), which is typical for fast-moving side-chains. However, both histidine side chains relaxed very slowly (R$_1$ 0.03 s^{-1}), implying that the stiffness of H16 and H18 is likely caused by a binding event. This is very much in agreement with previous mutational studies[25] where mutations of both H16 and H18 influenced the activity of plectasin. This came as a surprise, since H16 was not be identified as interaction partner in micelles[4]. The functional importance of both H16 and H18 suggests that both sides of the peptide must be involved in a binding event. However, only one side of the peptide can bind lipid II, since the side chains of H16 and H18 are pointing towards opposite directions. In Chapter 3, we discuss this more into detail and discover a novel secondary binding event.

Conclusions

Here, we have reported on the plectasin – lipid II complex in lipid membranes at the atomic level. Our data yield a critically refined view on the mode of action of plectasin in close-to-physiological conditions, which we expect to facilitate the design of a template for antimicrobials derived from plectasin and CSαβ defensins in general. Importantly, many of the binding features that we discovered were inaccessible in previous studies in micelles, highlighting the necessity to study small drugs such as antibiotics in native environment. Given the crucial need for high quality structural knowledge for drug design, we expect such ssNMR studies to become of vital importance to understand and improve lipid II binding antibiotics.

Materials and methods

Plasmid construction. The coding sequence of plectasin was obtained by gene splicing by overlap extension (gene SOEing)[27] and polymerase chain reaction (PCR) gene synthesis. For the latter, Klenow fragment is used to synthesise the double stranded DNA. Two primers were designed to amplify the plectasin gene (Table 1). Afterwards, PCR was performed with the fully synthesised gene sequence for the addition of 3' adenine overhangs by Taq DNA polymerase (ThermoFisher). Plectasin was cloned into the pET SUMO TA expression vector by TA overhang cloning according to the manufacturer's specifications (Figure 6). The resulting plasmid was sequenced to ensure the coding sequence of plectasin was correct and in-frame.

Table 1. Primer sequences used to acquire the full plectasin construct.

Primer	Primer sequence (5'- 3')
P$_1$	GGATTCGGTTGTAATGGACCCTGGGACGAGGATGACATGCAGTGCCATAATCATTGTAA ATCTATAAAAGGCTATAAGG
P$_2$	TCAATAGCACTTACAAACAAAACCGCCTTTCGCGCAATACCCTCCCTTATAGCCTTTTAT AGATTTACAATGATTATGGCAC
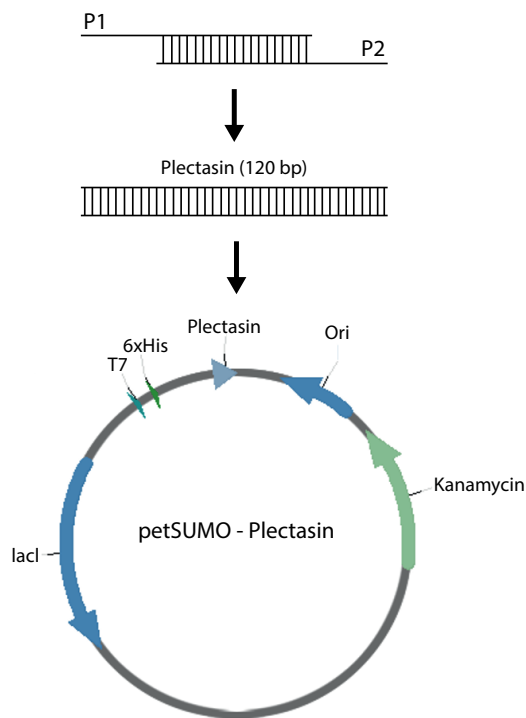
Figure 6. Schematic construct of the plectasin expression plasmid. Two partly overlapping primers were used to synthesize the full plectasin sequence which was subsequently cloned into the pET SUMO plasmid.

Sample preparation and purification. PET SUMO - plectasin was transformed into *E. coli* Shuffle® T7 cells (NEB) according to the manufacturer's specifications. Overexpression of the 6xHis-SUMO-plectasin fusion protein was accomplished following the protocol of [28,29] with some modifications. Expression of 6xHis-SUMO-plectasin was induced in 1L ^{13}C, ^{15}N-labelled M9 medium at OD 0.6 using 0.5 mM IPTG for a period of 4h at 37 °C. Cells were harvested by centrifugation at 4000 g at 4 °C for 30 min. Bacterial pellets were resuspended in lysis buffer (50 mM sodium phosphate, 150 mM NaCl, 25 mM imidazole and 1 mM β-mercaptoethanol, pH 8.0) supplemented with 200 µg/mL chicken egg white lysozyme and 1 µg/mL DNAse I. Cells were sonicated and cell debris was removed by centrifuging at 40 000 g for 30 min. The supernatant was filtered through a 0.45 µm filter. The 6xHis-SUMO-plectasin fusion protein was purified by affinity chromatography using pre-equilibrated Ni-NTA resins (Qaigen). The sample was applied to the resins and subsequently washed with 20 column volumes (CV) of wash buffer (50 mM sodium phosphate, 150 mM NaCl, 25 mM imidazole and 1 mM β-mercaptoethanol, pH 8.0 and eluted with 2 CV of elution buffer (50 mM phosphate buffer, 150 mM NaCl, 400 mM imidazole and 1 mM β-mercaptoethanol, pH 8.0). Afterwards, SUMO protease was added at a 1:1000

molar ratio to the purified fusion protein and incubated overnight at 4°C. Further purification of plectasin was accomplished by Size Exclusion Chromatography on a Superdex 30 Hiload 16/60 column at a flow rate of 2 mL/min with 50 mM sodium phosphate, 150 mL NaCl and 1 mM β-mercaptoethanol, pH 7.4. Fractions corresponding with pure plectasin were collected and concentrated to a desired concentration using a 3.5K cutoff Amicon Ultra filter unit (Millipore).

Site directed mutagenesis of plectasin. Mutagenesis of plectasin was performed as described in the QuickChange II Site-Directed Mutagenesis Kit (Agilent Technologies) manual. Primers were designed containing the desired mutation. The pET SUMO containing the plectasin gene was used as template. Reactions were thermocycled and digested with DpnI for 1h at 37 °C. *E. coli* DH5α cells were transformed with DpnI treated samples. Positive colonies were selected, plasmid DNA was isolated and sequenced.

Sample preparation for ssNMR measurements. Stock solutions of phospholipid 1,2-dioleoyl-sn-glycero-3-phosphocholine (DOPC) dissolved in chloroform (Avanti Polar Lipids) and lipid II carrying a heptaprenyl (C35) lipid tail (prepared as previously described[30]) in 2:1 chloroform/methanol were used for the preparation of the liposomes. For ssNMR measurements, the liposomes were prepared by first mixing the stock solutions of DOPC and lipid II to obtain 4 mol % (of total amounts lipids) lipid II in a glass test tube whereupon the solution was thoroughly dried under a nitrogen stream resulting in the formation of a thin lipid film layer on the bottom of the tube. Subsequently, plectasin in phosphate buffer (50 mM sodium phosphate, 150 mM NaCl and 1 mM β-mercaptoethanol, pH 7.4) was added to the film layer to a final molar ratio of 2:1 plectasin/lipid II. Liposomes with plectasin – lipid II complex were collected after ultracentrifugation at 100 000 g for 30 min at 4 °C. This sample preparation ensures that plectasin is present at both sides of the membrane, and thus is able to reach all the lipid II molecules in the vesicles. Subsequently, liposomes were directly centrifuged into 1.3 mm MAS rotors.

Solution NMR experiments. Solution NMR backbone assignments were performed with ^{13}C, ^{15}N-labelled unbound plectasin using 3D HNCα, 3D HNCαCβ, 3D HNCO and 3D CβCα(CO)NH experiments at 900 MHz magnetic field (^{1}H-frequency). Standard NMR pulse sequences from the Topspin sequence library were used for these experiments.

All relaxation experiments in solution with free plectasin were recorded at 600 MHz magnetic field at 298 K temperature. Heteronuclear ^{1}H-NOE and ^{15}N T_1 times were obtained using previously described pulse sequences[31]. The heteronuclear NOE was measured by recording spectra with and without the use of ^{1}H saturation prior to the experiment. Saturation of the amide protons was achieved by applying a series of 120° pulses on the amide protons. ^{15}N T_1

data sets were acquired using relaxation delays of 0.01, 0.05 (x2), 0.10, 0.20, 0.40 (x2), 0.70, 1.00 and 1.40 s. ^{15}N T$_2$ relaxation times were extracted from ^{15}N T$_{1rho}$ experiments performed as described previously[32]. During the relaxation period, an adiabatic spin-lock pulse of 1.9 kHz was applied with varying lengths of 4, 16 (x2), 32, 48, 80, 112 (x2), 128, 160, 208 and 256 ms. The following formula was then used to extract ^{15}N T^2 times from ^{15}N T$_{1\rho}$ times:

$$\frac{1}{T_{1\rho}} = \frac{1}{T_1}cos^2\theta + \frac{1}{T_2}sin^2\theta \tag{2.1}$$

with θ being the angle between the effective field and the static magnetic field. The T$_1$, T$_2$ and T$_{1\rho}$ trajectories were fit to single exponentials according to:

$$I = I^0 + e^{\frac{1}{T_1}} \tag{2.2}$$

SSNMR experiments. ^{1}H-detected 3D CαNH, 3D Cα(CO)NH and 3D CO(Cα)NH ssNMR experiments, using dipolar-based sequences as previously described[14], were carried out at 60 kHz MAS and magnetic fields of 700 MHz ^{1}H-frequency with a real temperature of about 308 K. All ^{1}H-detected experiments were performed using PISSARRO low-power decoupling in both direct and indirect dimensions[18]. Standard parameters were used for the low power decoupling (standard decoupling amplitude $v_{dec} = ^1/_4 \cdot v_{rot}$; pulse length $t_{dec} \sim 1/v_{dec}$; i.e., at 60 kHz MAS: $v_{dec} = 15$ kHz and $t_{dec} = 70$ µs). All pulse sequences are available from the authors upon request. For the ^{1}H-detected ^{15}N R$_1$ and R1$_\rho$ relaxation measurements, we used relaxation increments of 0, 5, 10, 20, 40, 80 and 120 ms to probe ^{15}N T$_{1\rho}$ relaxation; and 0, 1, 2, 4, 8 and 16 s to probe ^{15}N T1 relaxation. For the ^{15}N T$_{1\rho}$ measurements, we used the previously described pulse sequence[14] and a ^{15}N spinlock of 18 kHz.

The 2D PARIS[19] experiment was carried out at 950 MHz and 18 kHz MAS using a ^{13}C – ^{13}C mixing time of 20 ms. For the mixing period, we used the standard pulse-length of $^1/_2 \cdot \tau_{rot}$ and a ^{1}H-recoupling amplitude of 10 kHz, i.e., about half the MAS frequency.

Fluorescence experiments. DOPC vesicles for fluorescence measurements were generated by the extrusion technique[33] and were prepared with or without 2 mol % lipid II (referring to the total amount of lipids). Concentration of phospholipids was determined as inorganic phosphate after treatment with perchloric acid[34] by UV-VIS spectroscopy. Plectasin (50 mM sodium phosphate pH 7.4, 150 mM NaCl and 1 mM β-mercaptoethanol) was subsequently titrated with increasing concentrations of vesicles with or without lipid II. After addition of vesicles, the sample was left to incubate for 1 minute before fluorescence was measured. Tryptophan fluorescence was measured with excitation at 280 nm and emission was recorded between 300 and 400 nm both using a bandwidth of 5 nm. All measurements were performed with a Varian Cary Eclipse fluoresce

spectrophotometer. All fluorescence intensities were corrected for intensity caused by scattering by the liposomes.

Isothermal titration calorimetry (ITC). Small unilamellar vesicles (SUVs) of lipid II + DOPC lipids were prepared as described above. Plectasin (50 mM sodium phosphate, 150 mM NaCl and 1 mM β-mercaptoethanol, pH 7.2) and SUVs were degassed for 10 minutes prior to the ITC experiments. The chamber, with a maximal volume of 164 µL, was filled with plectasin and titrated with lipid II – doped DOPC liposomes at a rate of 1.96 µL/300 second with a constant syringe stirring rate of 300 rpm. All ITC measurements were performed at 37°C with a Low Volume NanoITC (TA Instruments). Data was analysed using the Nano Analyze Software (TA Instruments). Independent models were used for the fitting of the raw data.

MIC determinations. The antibacterial activity of plectasin mutants was determined according to the Clinical and Laboratory Standards Institute (CLSI) guidelines[35]. On polypropylene 96-well plates, plectasin mutants were serially diluted in cation-adjusted Mueller-Hinton broth (CAMHB). The colonies from overnight cultures on blood agar were suspended in CAMHB and turbidity was adjusted to 0.5 McFarland. The bacterial suspension was diluted 100 times in CAMHB before adding to the microplate (50 µL/well). For Streptococci strains, the broth was supplemented with 5% lysed horse blood. The plates were incubated at 37 °C with shaking (5% CO_2 was supplied for *Streptococci*) and investigated for bacterial growth after 16-20 h for *Staphylococci* and 24 h for *Streptococci*.

Supplementary information

Table S1. Solution NMR chemical shifts in ppm.

Residue	H^N	N	Cα	Cβ
G1				
F2			59.03	39.32
G3	7.86	101.40	44.35	
C4	7.52	123.24	52.87	34.79
N5	8.11	121.58	51.93	39.63
G6	7.19	110.13	42.66	
P7			64.21	31.07
W8	7.28	117.10	56.61	27.81
D9	7.59	124.01	53.78	40.66
E10	8.08	122.29	55.31	30.97
D11	8.09	125.82	52.31	40.95
D12	8.35	124.13	57.56	41.43
M13	8.13	118.20	57.49	31.31
Q14	7.57	121.63	58.93	28.62
C15	7.29	122.00	58.15	35.67
H16	8.91	122.83	60.77	31.84
N17	8.29	115.70	55.86	37.94
H18	7.90	123.07	59.80	29.47
C19	8.61	120.84	58.51	37.10
K20	7.73	115.11	58.06	31.51
S21	7.39	115.65	59.39	63.87
I22	7.51	126.56	60.70	37.94
K23	7.99	126.79	58.29	34.46
G24	8.36	113,91	44.83	
Y25	7.65	120.64	56.68	38.65
K26	10.50	121.55	55.89	34.74
G27	7.21	107.65	45.61	
G28	8.61	108.47	47.03	
Y29	8.33	116.39	55.94	40.09
C30	9.08	118.47	52.92	36.65
A31	9.50	129.93	50.72	22.58
K32	8.84	119.81	56.62	
G33	8,68	111,95	45.84	
G34	7.31	105.04	44.51	
F35	7.13	117.08	60.25	41.30
V36	7.63	118.91	60.66	35.48
C37	8.69	127.85	55.66	35.64
K38	8.92	136.75	54.59	34.00
C39	7.76	121.99	51.04	34.60
Y40	8.24	127.13	58.31	40.23
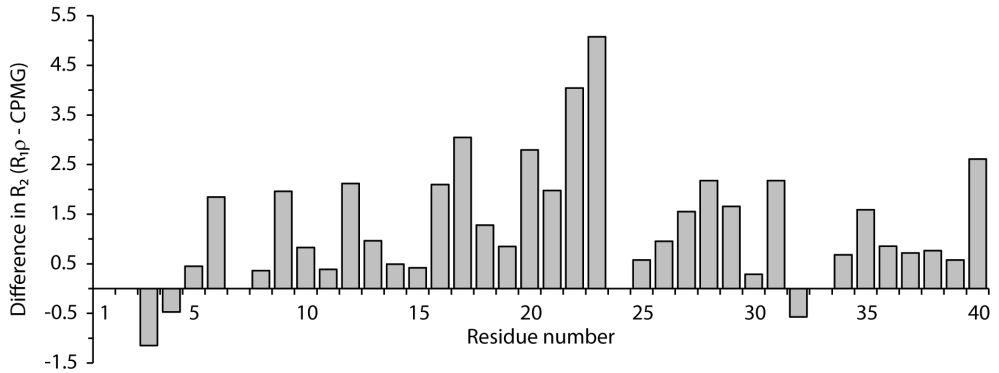
Figure S1. Difference between ^{15}N R_2 rate determined from both $R_{1\rho}$ and CPMG. High differences in R_2 rates are observed for residues I22 and K23 suggesting some kind of conformational flexibility in this region.
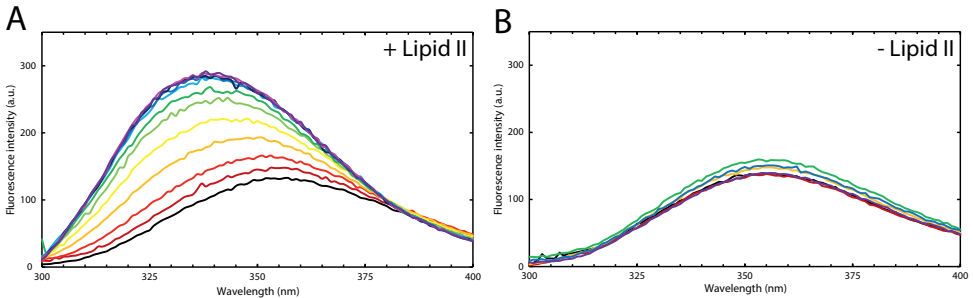
Figure S2. Intrinsic tryptophan fluorescence spectra of 1 µM plectasin titrated with A) DOPC liposomes doped with 2 mol % lipid II and B) DOPC liposomes only. In the presence of lipid II strong shifts in the fluorescence spectra are visible and demonstrate the tight interaction between plectasin and lipid II, i.e., the complex formation. In the absence of lipid II, however, no shifts are observable. The later clearly demonstrates that plectasin does not bind to DOPC liposomes in the absence of lipid II.

Table S2. SSNMR chemical shifts in ppm.

Residue	H^N	N	Cα	Cβ
G1				
F2	7.72	123.47	59.54	36.39
G3	8.34	101.44	44.59	
C4	8.10	124.73	52.86	33.43
N5	8.18	123.85	52.07	39.45
G6	6.90	107.32	41.77	
P7			64.88	31.06
W8	6.99	119.35	56.54	28.04
D9	7.41	125.39	53.82	40.22
E10	8.56	125.19	54.98	27.89
D11	8.32	128.12	51.14	39.42
D12	7.32	121.46	57.82	43.29
M13	8.39	117.30	56.70	30.22
Q14	7.71	123.19	59.16	27.99
C15	7.24	122.20	58.41	36.54
H16	9.41	123.36	61.03	31.72
N17	8.82	116.97	55.60	37.59
H18	7.81	123.18	59.16	29.71
C19	8.95	122.31	58.44	36.63
K20	8.10	115.19	58.04	31.68
S21	7.53	117.28	59.23	64.48
I22	7.80	128.45	61.14	39.77
K23	8.79	131.07	58.93	32.34
G24	8.83	116.44	44.43	
Y25	8.26	121.54	58.49	40.66
K26	11.04	120.90	54.54	35.34
G27	7.66	110.39	46.56	
G28	10.08	110.06	47.28	
Y29	8.77	114.67	56.71	39.89
C30	9.97	118.59	52.83	36.97
A31	10.36	132.28	50.35	23.40
K32	9.35	118.43	56.42	34.89
G33	8.85	107.73	46.45	
G34	7.21	102.17	44.23	
F35	7.25	119.09	61.06	41.75
V36	8.12	118.24	60.16	35.98
C37	10.14	130.40	55.81	35.22
K38	9.16	136.35	55.16	35.84
C39	7.84	121.02	50.76	35.84
Y40	8.87	128.09	58.94	40.73
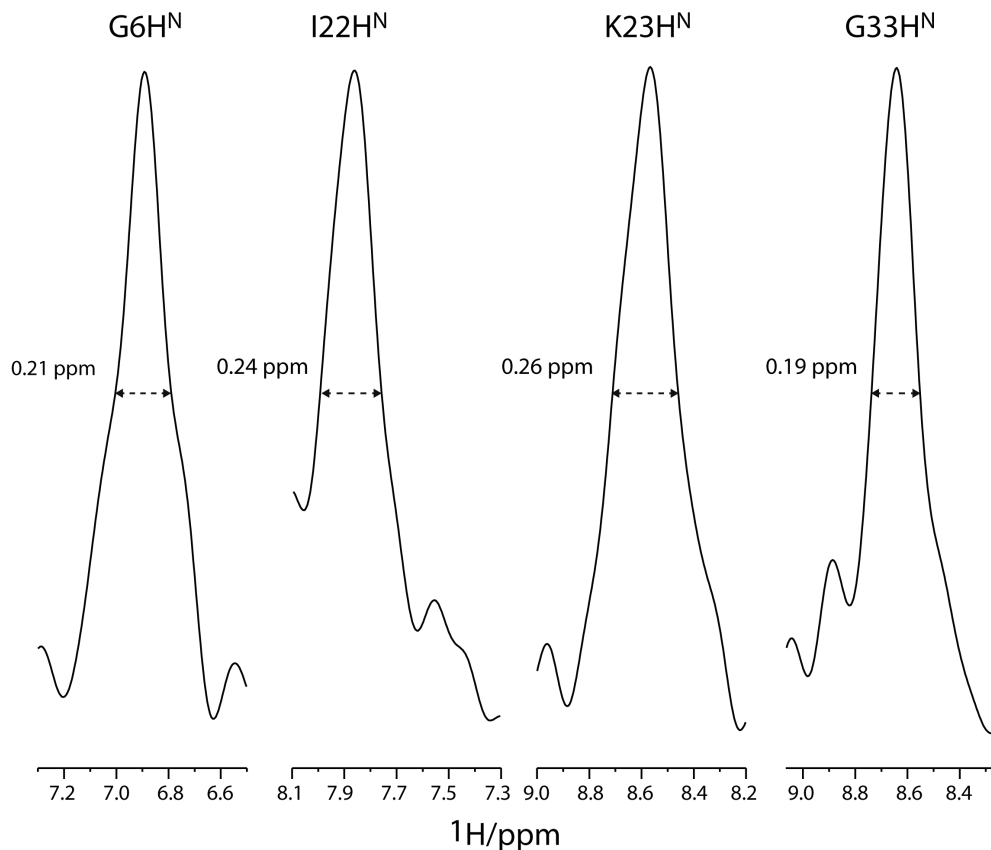
Figure S3. Cross-sections along the t_1 dimensions of the 2D NH spectrum of bound plectasin shown in the main text (Figure 3A). The cross-sections were extracted without application of a window-function in the ^1H dimension.

Table S3. Activity assays (MIC in µg/mL). I22 and Y25 mutants lose all activity towards the tested strains.

Mutant	*S. aureus* *USA300*	*S. simulans*	*S. pneumoniae* *ATCC6305*	*S. pyogenes*
Plectasin wt	12.5	0.78	≤0.78	≤0.012
I22A	>50	/	/	>25
I22K	>50	>50	>50	>25
Y25K	>50	>50	>50	>25
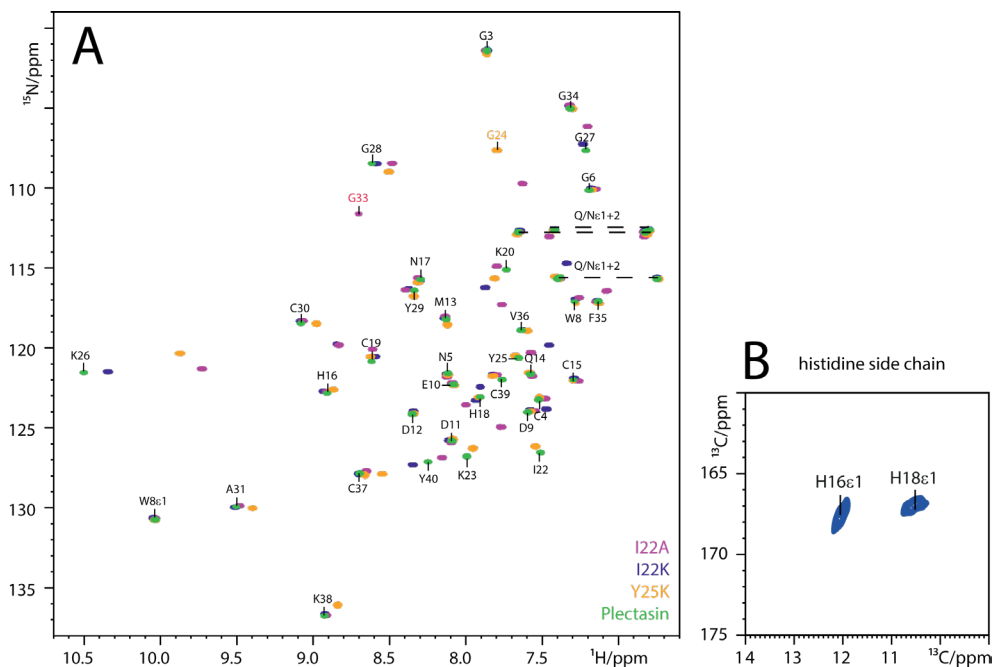
Figure S4. A) Overlay of solution NMR 2D ^{1}H-^{15}N HSQC spectra of plectasin wt (green) with mutants I22A (magenta), I22K (blue) and Y25K (yellow). Data demonstrate that the CSαβ-fold is maintained in the mutants. All data were acquired at 900 MHz. B) Side chain of H16 and H18 are both visible in our 2D NH spectrum. Spectrum was measured at 800 MHz at 60 kHz.

References

1   O'neill, J. Antimicrobial resistance: tackling a crisis for the health and wealth of nations. *Rev. Antimicrob. Resist* **20**, 1-16 (2014).

2   Mygind, P. H. *et al.* Plectasin is a peptide antibiotic with therapeutic potential from a saprophytic fungus. *Nature* **437**, 975 (2005).

3   Breukink, E. & de Kruijff, B. Lipid II as a target for antibiotics. *Nature reviews Drug discovery* **5**, 321 (2006).

4   Schneider, T. *et al.* Plectasin, a fungal defensin, targets the bacterial cell wall precursor Lipid II. *Science* **328**, 1168-1172 (2010).

5   Hsu, S.-T. D. *et al.* The nisin–lipid II complex reveals a pyrophosphate cage that provides a blueprint for novel antibiotics. *Nature structural & molecular biology* **11**, 963 (2004).

6   Cochrane, S. A. *et al.* Antimicrobial lipopeptide tridecaptin A1 selectively binds to Gram-negative lipid II. *Proceedings of the National Academy of Sciences* **113**, 11561-11566 (2016).

7   Ling, L. L. *et al.* A new antibiotic kills pathogens without detectable resistance. *Nature* **517**, 455 (2015).

8   Müller, A., Klöckner, A. & Schneider, T. Targeting a cell wall biosynthesis hot spot. *Natural product reports* **34**, 909-932 (2017).

9   Wilmes, M. & Sahl, H.-G. Defensin-based anti-infective strategies. *International Journal of Medical Microbiology* **304**, 93-99 (2014).

10   Østergaard, C., Sandvang, D., Frimodt-Møller, N. & Kristensen, H.-H. High cerebrospinal fluid (CSF) penetration and potent bactericidal activity in CSF of NZ2114, a novel plectasin variant, during experimental pneumococcal meningitis. *Antimicrobial agents and chemotherapy* **53**, 1581-1585 (2009).

11   Jing, X.-L. *et al.* High-level expression of the antimicrobial peptide plectasin in Escherichia coli. *Current microbiology* **61**, 197-202 (2010).

12   Linser, R. *et al.* Proton-detected solid-state NMR spectroscopy of fibrillar and membrane proteins. *Angewandte Chemie International Edition* **50**, 4508-4512 (2011).

13   Agarwal, V. *et al.* De Novo 3D Structure Determination from Sub-milligram Protein Samples by Solid-State 100 kHz MAS NMR Spectroscopy. *Angewandte Chemie International Edition* **53**, 12253-12256 (2014).

14   Medeiros-Silva, J. *et al.* 1H-Detected Solid-State NMR Studies of Water-Inaccessible Proteins In Vitro and In Situ. *Angewandte Chemie International Edition* **55**, 13606-13610 (2016).

15   Wang, Y. & Jardetzky, O. Probability-based protein secondary structure identification using combined NMR chemical-shift data. *Protein Science* **11**, 852-861 (2002).

16   Oeemig, J. S. *et al.* Eurocin, a new fungal defensin structure, lipid binding, and its mode of action. *Journal of Biological Chemistry* **287**, 42361-42372 (2012).

17   Weingarth, M. *et al.* Quantitative analysis of the water occupancy around the selectivity filter of a K+ channel in different gating modes. *Journal of the American Chemical Society* **136**, 2000-2007 (2014).

18   Weingarth, M., Bodenhausen, G. & Tekely, P. Low-power decoupling at high spinning frequencies in high static fields. *Journal of Magnetic Resonance* **199**, 238-241 (2009).

19   Weingarth, M., Bodenhausen, G. & Tekely, P. Broadband carbon-13 correlation spectra of microcrystalline proteins in very high magnetic fields. *Journal of the American Chemical Society* **131**, 13937-13939 (2009).

20   Münch, D. & Sahl, H.-G. Structural variations of the cell wall precursor lipid II in Gram-positive bacteria—Impact on binding and efficacy of antimicrobial peptides. *Biochimica et Biophysica Acta (BBA)-Biomembranes* **1848**, 3062-3071 (2015).

21   Teague, S. J. Implications of protein flexibility for drug discovery. *Nature reviews Drug discovery* **2**, 527 (2003).

22   Lewandowski, J. R., Sass, H. J. r., Grzesiek, S., Blackledge, M. & Emsley, L. Site-specific measurement of slow motions in proteins. *Journal of the American Chemical Society* **133**, 16762-16765 (2011).

23   Schanda, P., Meier, B. H. & Ernst, M. Quantitative analysis of protein backbone dynamics in microcrystalline ubiquitin by solid-state NMR spectroscopy. *Journal of the American Chemical Society* **132**, 15957-15967 (2010).

24   Witzke, S., Petersen, M., Carpenter, T. S. & Khalid, S. Molecular dynamics simulations reveal the conformational flexibility of lipid ii and its loose association with the defensin plectasin in the staphylococcus aureus membrane. *Biochemistry* **55**, 3303-3314 (2016).

25   Chen, H. *et al.* Design and pharmacodynamics of recombinant NZ2114 histidine mutants with improved activity against methicillin-resistant Staphylococcus aureus. *AMB Express* **7**, 46 (2017).

26   Li, S. & Hong, M. Protonation, tautomerization, and rotameric structure of histidine: a comprehensive study by magic-angle-spinning solid-state NMR. *Journal of the American Chemical Society* **133**, 1534-1544 (2011).

27   Horton, R. M., Cai, Z., Ho, S. N. & Pease, L. R. Gene splicing by overlap extension: tailor-made genes using the polymerase chain reaction. *Biotechniques* **8**, 528-535 (1990).

28   de Jong, R. N., Daniëls, M. A., Kaptein, R. & Folkers, G. E. Enzyme free cloning for high throughput gene cloning and expression. *Journal of structural and functional genomics* **7**, 109-118 (2006).

29   Folkers, G., van Buuren, B. & Kaptein, R. Expression screening, protein purification and NMR analysis of human protein domains for structural genomics. *Journal of structural and functional genomics* **5**, 119-131 (2004).

30   Breukink, E. *et al.* Lipid II is an intrinsic component of the pore induced by nisin in bacterial membranes. *Journal of Biological Chemistry* **278**, 19898-19903 (2003).

31   Farrow, N. A. *et al.* Backbone dynamics of a free and a phosphopeptide-complexed Src homology 2 domain studied by 15N NMR relaxation. *Biochemistry* **33**, 5984-6003 (1994).

32   Peng, J. W., Thanabal, V. & Wagner, G. 2D heteronuclear NMR measurements of spin-lattice relaxation times in the rotating frame of X nuclei in heteronuclear HX spin systems. *Journal of Magnetic Resonance (1969)* **94**, 82-100 (1991).

33   Hope, M., Bally, M., Webb, G. & Cullis, P. Production of large unilamellar vesicles by a rapid extrusion procedure. Characterization of size distribution, trapped volume and ability to maintain a membrane potential. *Biochimica et Biophysica Acta (BBA)-Biomembranes* **812**, 55-65 (1985).

34   Rouser, G., Fleischer, S. & Yamamoto, A. Two dimensional thin layer chromatographic separation of polar lipids and determination of phospholipids by phosphorus analysis of spots. *Lipids* **5**, 494-496 (1970).

35   Hecht, D. W. *et al. Methods for Antimicrobial Susceptibiluty Testing of Anaerobic Bacteria: Approved Standard*. (Clinical and Laboratory Standards Institute Wayne, PA, 2007).

CHAPTER 3

The mode of action of plectasin in
membranes

Chapter 3 is a follow-up on Chapter 2 and includes the latest insights into the mode of action of plectasin in lipid membranes. The reader is referred to Chapters 1 and 2 for an introduction on the plectasin – lipid II complex.

In Chapter 2 we have characterized plectasin in the free state, and bound to lipid II in the presence of membranes. In Chapter 3 we study the plectasin – lipid II interface at greater detail, including oligomerization and ion binding properties of plectasin that were not reported before.

The plectasin – lipid II complex interface and membrane topology

Plectasin is the first identified CSαβ defensin to target lipid II[1], which is composed of a sugar-pentapeptide head group that is connected to an isoprenoid tail through a pyrophosphate (PPi) group. Plectasin is assumed to target the irreplaceable PPi group and the pentapeptide of lipid II. However, no experimental data could be acquired for this interaction thus far. Here, we use solid-state NMR (ssNMR) to define the plectasin – lipid II complex interface in membranes.

First, we performed a ^{31}P CP ssNMR experiment in liposomes to probe if plectasin targets the PPi group of lipid II. Indeed, in the presence of plectasin we observe stark CSPs of the PPi signals of lipid II, strongly suggesting that plectasin directly binds to the PPi group (Figure 1A). This finding was validated by a 2D HP ssNMR spectrum which showed clear contacts between the amino protons of plectasin and the PPi group (Figure 1B). These amino protons would match G28 or C37, confirming that the β-strand of plectasin coordinates the PPi group. Note that the strong signal at 8.0 ^{1}H ppm most likely relates to the NAc group of MurNAc which is in close proximity to the PPi group.

Figure 1. Plectasin binds to the pyrophosphate and the sugar-pentapeptide headgroup. A) 1D ^{31}P CP spectra of lipid II in liposomes with (purple) and without (grey) plectasin, measured at 500 MHz and 15 kHz MAS. PPi signals show stark CSPs in the presence of plectasin. B) 2D ^{1}H-^{31}P CP spectrum of the plectasin – lipid II complex. Interfacial contacts were observed that could correspond to the amino protons of G28 and C37. Spectrum was recorded at 800 MHz, 60 kHz and 2.5 ms transfer time. C) Dipolar-based ^{13}C-^{13}C PARIS spectrum of ^{15}N,^{13}C-lipid II bound to unlabelled plectasin shows that both sugars and part of the pentapeptide are rigid and most likely involved at the complex interface. The lipid II sugar-pentapeptide headgroup could be fully assigned. Spectrum was measured at 700 MHz and 42 kHz MAS. D) The C-terminus of lipid II is flexible and does not interact with lipid II.

Next, we aimed to define the interaction between plectasin and the sugar-pentapeptide headgroup. To achieve this, we successfully produced ^{15}N,[13]C-labelled lipid II, which is expected to be a significant contribution for structural studies on drug – lipid II complexes. To determine the role of the sugar-pentapeptide headgroup, we recorded a 2D ^{13}C-^{13}C dipolar-based ssNMR experiment, which is sensitive to rigid residues only, of ^{15}N,[13]C-lipid II in complex with ^{14}N,[12]C-plectasin. We observed strong signals for MurNAc and GlcNAc, suggesting that both sugars directly participate in the complex (Figure 1C). This is further corroborated by the 2D NH ssNMR spectra which demonstrate that plectasin binds to lipid I, which lacks GlcNAc, but forms a rather disordered complex (Figure S1A). This coincides with the big hit in binding affinity that was previously reported[1], meaning that GlcNAc is critical for the formation of a stable complex.

While residues A1 – A4 of the pentapeptide were detected in the dipolar-based spectrum, alanine 5 could not be observed suggesting an enhanced mobility towards the C-terminus of the pentapeptide (Figure 1D). Indeed, scalar-based 2D NH (Figure S1B, C) and [13]C-^{13}C TOSBY spectra (data not shown) confirmed that residues 4 and 5 have increased dynamics, clearly indicating that the C-terminus does not operate at the complex interface. As expected, residues A1 and E2 do not appear in scalar-based spectra, meaning that both residues are rigid and potentially involved in a binding event. This is in line with the fact that amidation of residue E2, which reduces the charge of the PGN network, decreases the efficacy of plectasin[2]. Hence, the charge of residue E2 is of critical importance for the activity of plectasin. Residue K3 appears in both dipolar- and scalar based spectra, suggesting that it has some degree of flexibility and is most likely not involved in binding. We validated this by comparing binding of plectasin to Gram-negative lipid II, which possesses a meso-diaminopimelic acid (mDAP) residue instead of a lysine at the 3-position in the pentapeptide. Only marginal differences were observed in ssNMR spectra of plectasin bound to mDAP-lipid II and lys-lipid II (Figure S1D, E), which agrees with the moderate mobility observed in residue K3, implying that it has no role in complex interactions. Notably, while the pentapeptide domain gave well-defined signals in the dipolar-based spectrum, we observed signal heterogeneity in the sugar region, for instance in GlcNAc-C1, suggesting some plasticity at the binding interface.

A 2D ^{13}C-^{13}C ssNMR experiment on ^{15}N,[13]C-plectasin in complex with ^{15}N,[13]C-lipid II enabled us to pinpoint the complex interface. We observed several unambiguous interfacial contacts that relate to E2 of the pentapeptide and Y40 of plectasin, further confirming that E2 is indeed directly involved in complex formation (Figure 2A). For the sugars, we repeatedly observe ambiguous contacts in line with correlations to F2, W8, H16, H18, Y25, Y29 and F35 (Figure

2A-C). Interestingly, we obtained one faint unambiguous interfacial contact between residue H16 and GlcNAc, implying that H16 directly binds to GlcNAc.

$^{15}N,^{13}C$-plectasin + $^{15}N,^{13}C$-lipid II / $^{15}N,^{13}C$-plectasin + $^{14}N,^{13}C$-lipid II
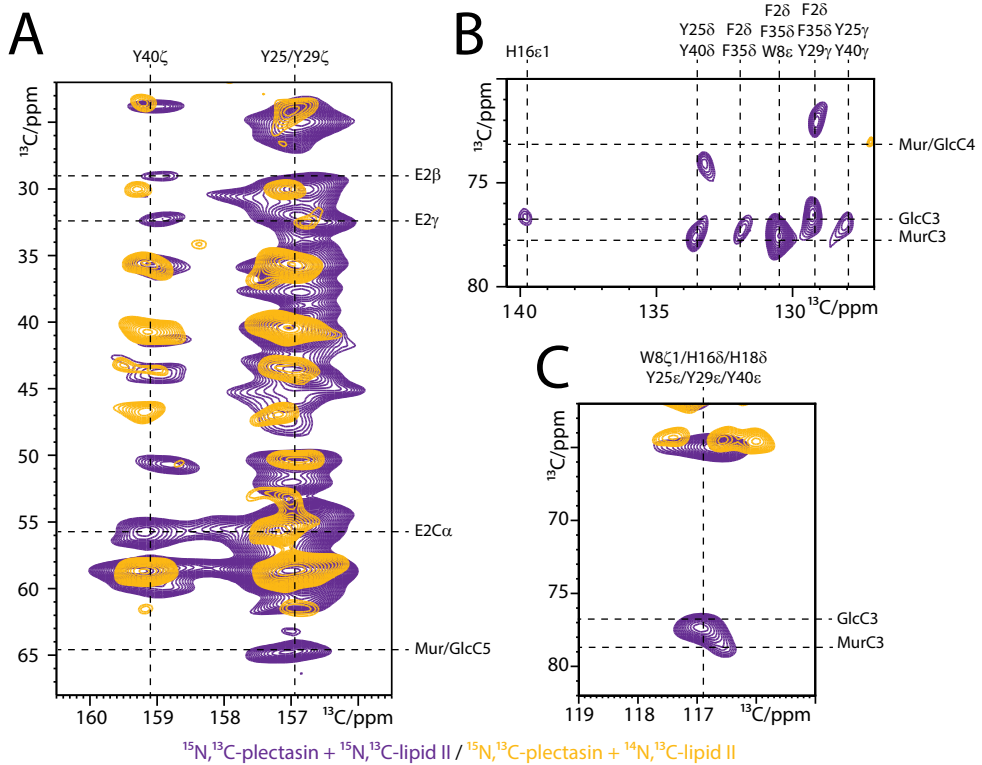
Figure 2. The role of the sugar-pentapeptide head group. Cut-outs of a ^{13}C-^{13}C spin diffusion spectrum of ^{15}N, ^{13}C-plectasin in complex with unlabelled (yellow) and $^{15}N,^{13}C$-labelled lipid II (purple). Unambiguous interfacial contacts show that Y40 directly binds to residue E2 of the pentapeptide (A). Multiple contacts were also found between plectasin and the sugars, confirming involvement of the sugars in the complex interface (A, B and C). Measurements on the complex with unlabelled and labelled lipid II were performed on 900 and 700 MHz, respectively, and 16 kHz MAS.

Our ssNMR data reveal that the previously reported plectasin – lipid II complex model, where the conserved residue H18 was shown to be the primary binding site for E2, must me incorrect. Moreover, H18 was assumed to be positively charged, which is important for the binding mode of plectasin. Thus far, no experimental data could further support these assumptions. In Chapter 2, we have clearly demonstrated that H18 is not charged in lipid membranes. Altogether, we have identified residue Y40 as interaction site for the pentapeptide. Furthermore, our findings confirmed that both sugars are directly involved at the complex interface. Unfortunately, signals of MurNAc and GlcNAc largely overlapped, hence we could not unambiguously identify key residues that target the sugars, with the exception of H16. In the future, we will

produce lipid II where only one of the sugars will be isotope labelled. This will reduce the ambiguity in our binding interface analysis.

Next, we investigated the membrane topology of plectasin, which is fundamental to our understanding of plectasin – lipid II interactions. While the topology has already been investigated in micelles[1], our study demonstrates that the complex is different in a natural membrane environment. SSNMR spectroscopy provides a unique approach to obtain peptide – membrane topological information in physiologically relevant media.

Here, we conducted T_2-edited 2D ^{1}H(H)^{13}C experiments[3], with a ^{1}H-^{1}H mixing time of 5 ms, on the plectasin – lipid II complex to define the orientation of plectasin on the membrane (Figure 3A-C). The corresponding experiments rely on magnetization transfer from mobile water or lipid ^{1}H to the rigid antibiotic via a short dipolar transfer step and hence will enable us to pinpoint residues that partition in the water and lipid phases. The 2D spectrum unambiguously shows that the backbone of residues N5, P7, W8 and A31 – F35, and side chains of V36 are lipid exposed. Intriguingly, all obtained unambiguous contacts are related to the hinge in the N-terminal loop (N5 – W8) and the loop that connects the two β-strands (A31 – V36). Thus far, our NMR data suggest that these loops partition into the membrane, whereas the hydrophobic residues of the αβ-loop do not act as membrane-anchors and are exposed to the water phase (Figure 3D). Interestingly mutations in N5 to either lysine or arginine subtly improved the activity of plectasin, suggesting that the membrane-anchoring interface is an interesting hotspot for the rational design of plectasin (Table S1). It should be noted that residues such as M13 and N17, which seem neither involved in lipid II nor in membrane-anchoring, do not affect the activity of plectasin.

For most of our ssNMR experiments, we have assembled the plectasin – lipid II complex in zwitterionic DOPC liposomes. However, the lipid bilayer of Gram-positive bacteria is largely characterized by anionic lipids[4]. To ascertain the effect of anionic lipid bilayer, we assembled the plectasin – lipid II complex in DOPG liposomes and recorded a 2D NH spectrum (Figure 3E). Only subtle changes in chemical shifts were observed, with the largest differences in the cationic residues K23 and K32 (Figure S1D) which may both contact the lipids headgroups. (Figure 3A-D). Therefore, our data implies that the membrane composition does not affect the mode of action of plectasin.
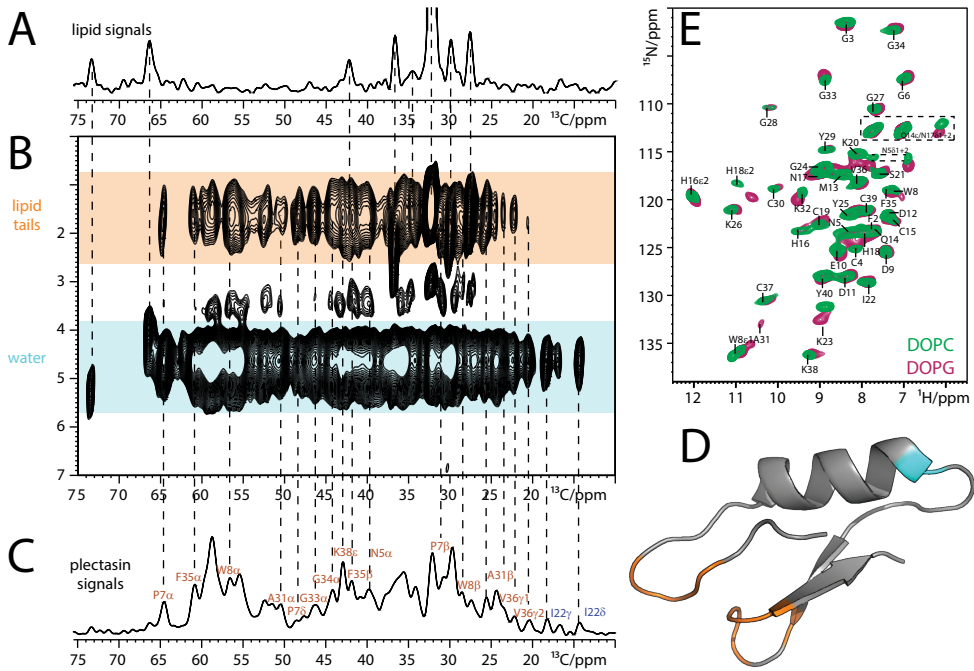
Figure 3. The orientation of plectasin on lipid membranes. A) 1D T_2-edited ^{1}H(H)^{13}C solid-state NMR spectrum of ^{15}N,^{13}C-plectasin – lipid II complex, recorded at 700 MHz using a T_2 delay of 2.5 ms to de-phase signals of the complex. ^{1}H-^{1}H mixing was set at zero to prevent magnetization transfer to the rigid complex. Remaining signals show lipids. B) 2D T_2-edited ^{1}H(H)^{13}C spectrum of ^{15}N,^{13}C-plectasin bound to lipid II, measured at 700 MHz using a T_2 delay of 2.5 ms and 5 ms ^{1}H-^{1}H mixing time. C) ^{13}C CP spectrum of the complex, acquired at 700 MHz using 200 µs contact time. D) NMR based illustration of water (blue) and lipid (orange) exposed residues. E) Overlay of 2D NH ss NMR spectra of lipid II – bound plectasin in DOPC (green) and DOPG (magenta) liposomes. Both spectra were measured at 700 MHz and 60 kHz MAS.

Plectasin oligomerises in the lipid II bound state

Previous studies reported that plectasin binds to lipid II in a 1:1 stoichiometry[1]. However, this finding was established using a soluble truncated lipid II version in micelles, i.e., in non-physiological conditions. To determine the stoichiometry in membranes, we co-assembled plectasin with lipid II at molar ratios of 0:1, 0.5:1, 1:1 and 2:1 and measured ^{31}P CP ssNMR spectra to evaluate the ^{31}P PPi signals of lipid II. The signal intensity of the PPi group was determined and was used to derive a binding curve (Figure 4A). Our ^{31}P NMR titration shows that the 1:1 stoichiometry is conserved in membranes.

We have previously shown that both H16 and H18 side chains are unusually rigid in the complex (Chapter 2, Figure 4C), most likely caused by a binding

event. Additionally, previous mutational studies[5] showed that H16 and H18 modulate the antimicrobial activity of plectasin. Interestingly, the side chains of H16 and H18 are pointing towards opposite directions (Figure S2A). It is therefore unlikely that both residues are involved in lipid II binding. A second, thus far, unknown binding event could provide an explanation for the observed enhanced rigidity. Our hypothesis is that plectasin oligomerizes upon lipid II binding with either H16 or H18 at the dimerization interface.

In order to directly probe oligomerization events, we mixed uniformly ^{15}N-labelled plectasin with uniformly ^{13}C-labelled plectasin[6]. Magnetization transfer between ^{15}N and ^{13}C can only be established if the distance between the two nuclei is less than 5 Å (Figure 4B). Here, we mixed an equimolar ratio of ^{15}N-plectasin and ^{13}C-plectasin that we subsequently co-assembled with 0.5 mol % lipid II, which is similar to the estimated amount of lipid II in bacteria (0.1 – 1 mol %)[7]. Hence, our experimental design is physiologically relevant. Moreover, using a small concentration of lipid II avoids false positives caused by crowding effects rather than specific oligomerization events. However, such a low lipid II concentration requires highly sensitive methods such as Dynamic Nuclear Polaization (DNP), which can significantly improve the signal intensity of biomolecules[8-10].

First, we recorded a series of 1D ^{15}N(HH)^{13}C DNP spectra, which can be interpreted as ssNMR "FRET-like" experiments, with ^{1}H-^{1}H magnetization transfer times that enable magnetization transfer from ^{15}N nuclei to ^{13}C nuclei (Figure 4B, C). We obtained a DNP enhancement ε of 53 (Figure 4E). Interestingly, we observed pronounced transfer to ^{13}C nuclei, demonstrating that plectasin oligomerizes upon lipid II binding (Figure 4C). We can also rule out contributions from plectasin that is not bound to lipid II or natural abundance contributions (Figure S2B, C). We would like to emphasize that this is the first study to report on self-association of plectasin upon lipid II binding, which could be a mechanism that is conserved among the CSαβ defensins[11,12] to target lipid II. Again, this further highlights the necessity of studying such drugs in physiologically relevant media, since oligomerization of plectasin was not observed in micelles[1]. Further studies will be necessary to establish the precise higher-order architecture of the plectasin-lipid II complex.

As a next step, we investigated the plectasin – plectasin interface using a 2D ^{15}N(HH)^{13}C experiment (Figure 4D). Due to line broadening of signals at cryogenic temperatures, we could not identify unambiguous interfacial interactions. Nonetheless, we observed several contacts that we can assign to a group of residues, which gives us more insight into the dimerization interface. It comes as no surprise that we observe an interfacial contact that relates to histidine side chains, strongly indicating that indeed either H16 or H18 is close to the dimerization interface. We also detect lysine side chains in the

dimerization interface, visible from the back folded signals around 75 ppm in the ^{15}N plane. Furthermore, we obtained multiple correlations with aromatic signals of around 128.8-141.2 ^{13}C ppm.
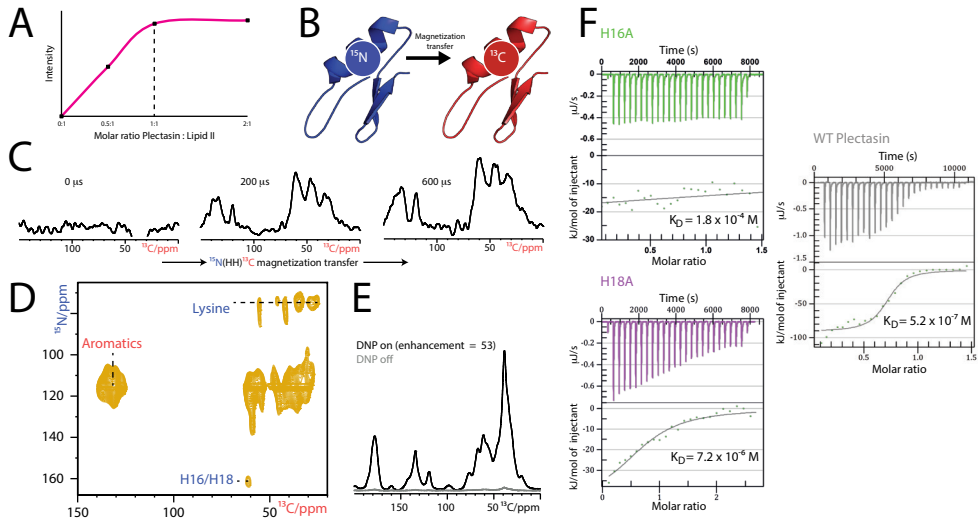

Figure 4. Stoichiometry of plectasin in membranes. A) ^{31}P ssNMR spectra were recorded of plectasin co-assembled with lipid II at molar ratios of 0:1, 0.5:1, 1:1 and 2:1. ^{31}P PPi signals intensities were evaluated and used to derive a binding curve, which clearly indicates a 1:1 stoichiometry. B) An equimolar ratio of ^{15}N-plectasin and ^{13}C-plectasin were mixed to probe if plectasin self-associates. C) A series of 1D NHHC spectra with increasing ^{1}H-^{1}H magnetization transfer times applied to the complex containing mixed-labelled plectasin. Spectra were acquired at 400 MHz DNP, 8 kHz MAS, and 100 K. D) 2D ^{15}N(HH)^{13}C spectrum of ^{15}N, ^{13}C mixed labelled plectasin in complex with lipid II measured at 400 MHz DNP, 8 kHz MAS and 100 K. E) ^{13}C CP spectra of lipid II – bound plectasin with (black) and without (grey) DNP enhancement ε 53. F) Isothermal Titration Calorimetry (ITC) data for H16 and H18 mutants obtained in DOPC liposomes. Both H16 and H18 mutants drastically influence the binding affinity of plectasin.

Our findings strongly suggest that one histidine is involved in oligomerisation, whereas the other participates in lipid II binding. To establish the roles of both histidine residues, we measured the binding affinity of H16 and H18 mutants using Isothermal Titration Calorimetry (ITC) (Figure 4F). Interestingly, we found weaker binding affinities for both histidine mutants, with a K_D of $1.8 \cdot 10^{-4}$ and $7.2 \cdot 10^{-6}$ M for H16 and H18 mutants, respectively. The much bigger hit in binding affinity in the H16 mutant implies that H16 directly binds to lipid II, whereas H18 is rather involved at the plectasin – plectasin interface. This would be in line with the interfacial contact that we previously observed between H16 and GlcNAc. At the moment of writing, we are employing 1D ^{15}N(HH)^{13}C experiments on plectasin H16 and H18 mutants to further corroborate our

findings.

To further investigate the newly discovered oligomerization property of plectasin, we co-assembled plectasin with lipid II at a 0.5:1, 1:1, and 2:1 molar ratio in lipid membranes and acquired 2D ^{15}N-^{1}H spectra (Figure 5A). Overall, the two spectra look very similar with the exception of residues C4, N5, W8, D12, H16, G28, Y29, C30, A31, C37, K38 and C39 (Figure 5B), which have either disappeared or significantly shifted, implying that these residues show different conformations depending on the molar ratio of plectasin and lipid II. Interestingly, these residues are either directly involved at the complex interface or in membrane-anchoring. Hence, we assume that in case of excess of lipid II plectasin binds as a monomer, but rather as an oligomer when there is an equimolar amount of the drug and target. ^{15}N $R_{1\rho}$ bulk relaxation measurements further support our hypothesis where plectasin shows higher dynamics in a 0.5:1 molar ratio compared to a 1:1 molar ratio of plectasin:lipid II (Figure 5C), consistent with a smaller, more flexible complex at a 0.5:1 ratio. Note that there is no difference in dynamics between the 1:1 and 2:1 molar ratio complex, further validating that plectasin indeed binds lipid II in an equimolar ratio.
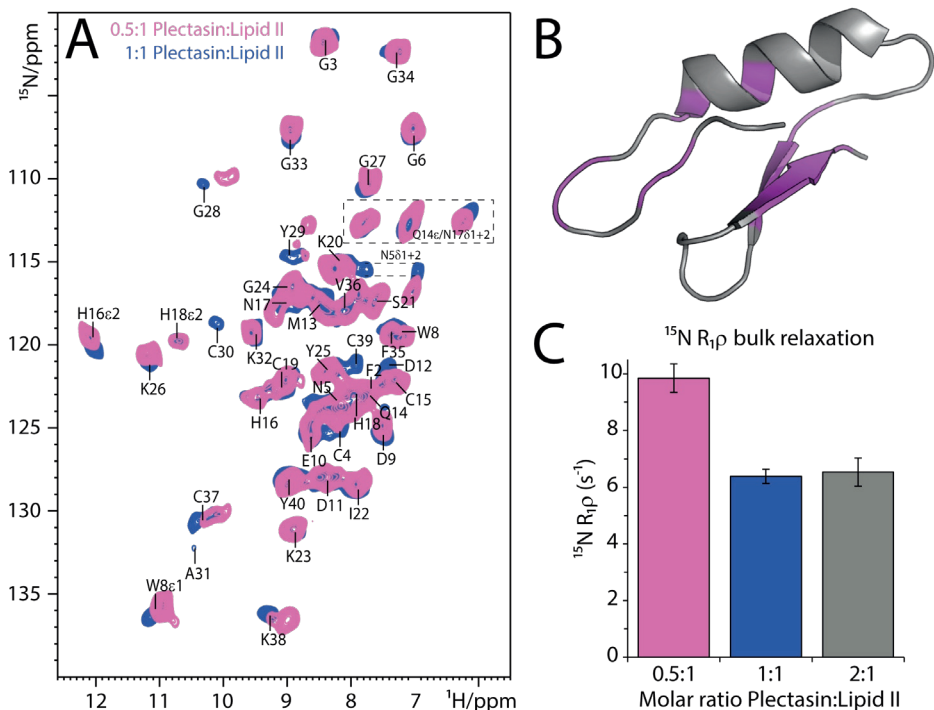
Figure 5. Molar ratio of plectasin:lipid II modulates mode of action of plectasin.
A) ^{1}H-detected 2D ^{15}N-^{1}H spectral overlay of 0.5:1 and 1:1 molar ratio of plectasin:lipid II shown in magenta and blue, respectively. Spectra were acquired at 700 MHz, 60 kHz MAS, and about 300 K sample temperature. B) Residues that are involved in lipid II

binding and membrane anchoring show significant differences in the two different molar ratios. C) ^{15}N R$_{1\rho}$ bulk relaxation rates of 0.5:1 (magenta), 1:1 (blue) and 2:1 (grey) molar ratio of plectasin:lipid II.

Plectasin binds to divalent ions

Interestingly, one previous study reported a marked influence of divalent ions such as calcium (Ca^{2+}) and magnesium (Mg^{2+}) on the microbicidal activity of plectasin[13]. However, no molecular explanation was provided, and a potential role of ions was not considered in the study. Unlike other CSαβ defensins, plectasin possesses a curious negative patch D9 – E10 – D11 – D12 with unknown structural or functional role. We hypothesized that this negative patch directly binds divalent ions.

In order to determine if plectasin interacts with divalent ions, we measured solution NMR spectra of free plectasin in the presence of manganese (Mn^{2+}) ions. Manganese ions are, besides biologically relevant[14], also paramagnetic, meaning that they can affect NMR signals. These paramagnetic effects can manifest in either enhanced relaxation rates, chemical shifts or both, and rely heavily on the distance between the nuclei and ion[15]. Such data can therefore be used to pinpoint the ion-binding interface. A solution NMR spectral overlay of free plectasin with and without Mn^{2+} ions demonstrates that Mn^{2+} indeed affects relaxation rates in plectasin as the intensity of multiple signals is reduced (Figure 6A). This clearly supports the idea of plectasin interacting with divalent ions. A small patch of residues, including the negative patch E10 – D12 and C30 – F35, were fully quenched by Mn^{2+} ions implying that these residues directly contact the ion (Figure 6B, C). Altogether, we have discovered, for the time ever, a novel feature of plectasin that should be taken into consideration in the rational design of plectasin derivatives.

To probe the effect of a divalent ion on the complex, we co-assembled plectasin with lipid II in the presence of Ca^{2+} and measured 2D NH ssNMR experiments (Figure 6D). Our ssNMR data show that Ca^{2+}, and most likely other divalent ions, does not interfere with complex formation given the small observed differences in spectra of the complex with and without Ca^{2+}. The largest differences between the two samples are indeed observed in residues that are at the ion-binding interface. Thus far, as this finding is very preliminary, it is still poorly understood what the biological contribution is of the ion. Further research is a must in order to underline if the ion participates in the complex or if it rather interferes with the binding of plectasin to lipid II to a certain degree.
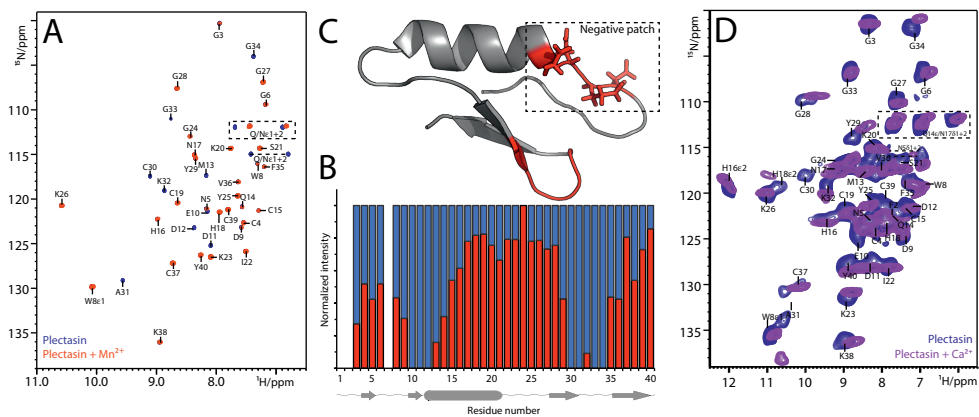
Figure 6. Plectasin binds to divalent ions. A) Solution NMR 2D ^{15}N-^{1}H spectral overlay of free plectasin with (red) and without (blue) Mn^{2+} ions measured at 600 MHz. B) Normalized signal intensity of plectasin with (red) and without (blue) Mn^{2+} ions. Residues E10 – D12, C30, A31, G34 and F35 were fully quenched, implying that these residues are in direct contact with the ion. C) NMR based illustration of the ion-binding interface of plectasin. D) 2D ^{15}N-^{1}H spectral overlay of lipid II bound plectasin in presence (purple) and absence (blue) of Ca^{2+}. Spectra were acquired at 60 kHz MAS and 700 MHz.

Conclusions

Our ssNMR study provides high-resolution insights into the mode of action of plectasin in physiologically relevant conditions. Using a unique approach with isotope-labelled lipid II we have refined our understanding on the plectasin – lipid II complex interface and identified key residues that are involved at the interface. Along the same line, we have discovered that plectasin oligomerizes upon lipid II binding, which could be a shared mechanism among CSαβ defensins. As demonstrated in this work, the previously published complex model[1] did not capture the correct interaction interface. In addition, we have discovered interesting novel features of plectasin that may be particularly important for drug design studies. These insights could be relevant for lipid II targeting CSαβ defensins in general.

Materials and methods

Sample preparation. Plectasin and the plectasin – lipid II complex samples were prepared according to the described protocol in Chapter 2. ^{15}N, ^{13}C-lipid II was extracted from *Micrococcus flavus* grown on ^{15}N,^{13}C-labelled rich medium. Lipid II was subsequently purified by anion exchange chromatography (S2).

For the ^{15}N(HH)^{13}C experiments, ^{14}N,^{13}C-plectasin was mixed with ^{15}N,^{12}C-plectasin at equimolar amounts. The peptide solution was subsequently mixed with 0.5 mol % lipid II-containing DOPC liposomes as described in the previous chapter.

SSNMR experiments. 2D ^{1}H-detected ssNMR experiments were performed with 1.3 mm rotors at 60 kHz MAS at 16.4 and 18.8 T (700 and 800 MHz ^{1}H frequency, Bruker Biospin). All experiments were performed using dipolar based sequences. For all cross-polarization (CP) steps, ramped contacts (10-20%) were used. The last transfer step from ^{15}N to ^{1}H was kept short (600 – 800 ms). PISSARO[16] low-power (15 kHz decoupling amplitude, 70 ms pulse length) decoupling was used in all indirect and direct detection periods.

All ^{13}C-detected experiments were performed with 3.2 mm rotors. 2D ^{13}C-^{13}C dipolar based experiments were performed with PARIS[17] recoupling at 700 and 950 MHz at 18 kHz MAS. The PARIS recoupling amplitude was 10 kHz for mixing times of 20 – 600 ms and we used the standard phase inversion time of $^1/_2 \cdot \tau_{rot}$. SPINAL[18] was used in both indirect and direct detection periods.

The T_2 – edited 2D ^{1}H(H)^{13}C experiment[19,20] was performed at 700 MHz with 16.5 MAS at 300 K temperature. A T_2 relaxation filter of 2.5 ms was used. Magnetization from mobile lipids and water molecules was transferred to the rigid antibiotic with 5 ms ^{1}H-^{1}H magnetization transfer and subsequently transferred to ^{13}C nuclei of plectasin with a short CP (200 ms) CP step.

All DNP enhanced ^{15}N(HH)^{13}C experiments were carried out at 400 MHz, 8 kHz MAS and 100 K. For the 2D experiment, we used very short (80 ms) for the second and third CP step and a ^{1}H-^{1}H spin diffusion time of 200 ms.

Supplementary information
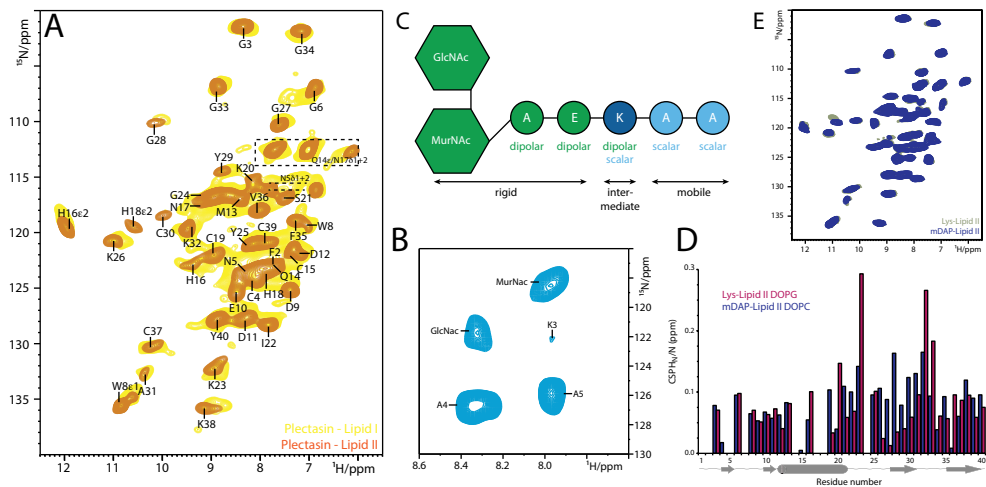
Figure S1. A) 2D NH ssNMR spectral overlay of plectasin bound to lipid I (yellow) and lipid II (orange). Plectasin still binds in the absence of GlcNAc, but forms a disordered complex as can be deduced from the increased spectral heterogeneity. Samples were measured in DOPG liposomes. B) Scalar-based NH HSQC of plectasin in complex with ^{15}N,^{13}C-lipid II shows intense signals for residues A4 and A5, suggesting an enhanced mobility towards the C-terminus of the lipid II pentapeptide. C) SSNMR based illustration regarding the mobility of lipid II. D) CSPs showing the effect of mDAP-lipid II and the membrane composition on the complex with plectasin. E) 2D NH spectra of plectasin bound to lys-lipid II (grey) and mDAP-lipid II (blue) show no differences, implying that residue K3 does not modulate the binding mode of plectasin.

Table S1. Activity assay (MIC in µg/mL) including different plectasin mutants.

Mutant	S. aureus USA300	S. simulans	M. flavus	S. pneumoniae ATCC6305
Plectasin wt	12.5	0.78	25	≤0.78
N5R	3.13	≤0.39	3.13	≤0.78
N5K	6.25	≤0.39	6.25	≤0.78
M13A	6.25	1.56	12.5	≤0.78
N17A	6.25	0.78	12.5	≤0.78
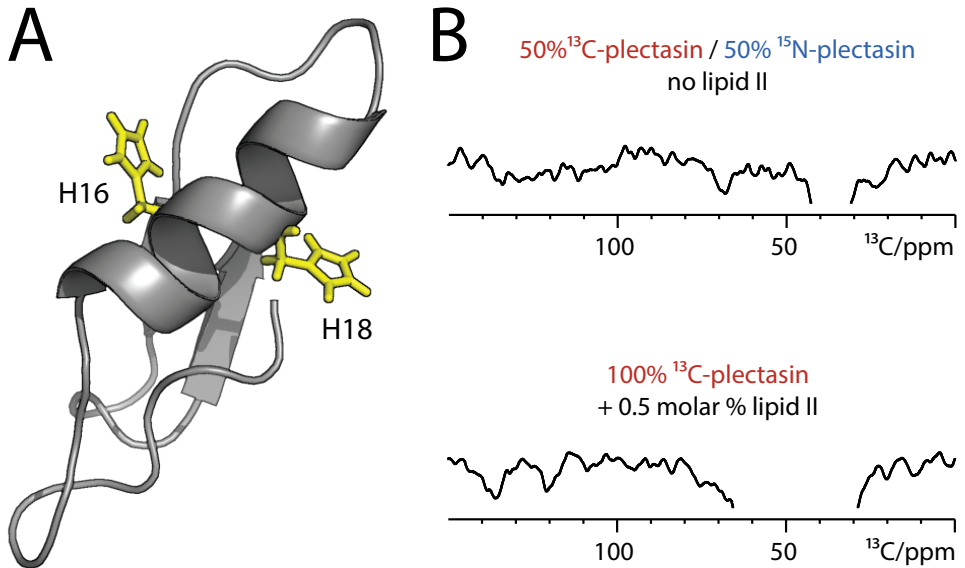
Figure S2. A) The side chains of H16 and H18 are facing opposite directions, hence only one histidine can be involved in lipid II binding. The other histidine could potentially participate in a second, thus far, unknown binding event. B) ^{15}N(HH)^{13}C DNP-ssNMR experiments on ^{15}N, ^{13}C mixed labelled plectasin in absence of lipid II (upper panel) and uniformly ^{13}C-plectasin with lipid II (lower panel) showed no signals. Hence, we can rule out contributions from plectasin that is not bound to lipid II or natural abundance contributions.

References

1   Schneider, T. *et al.* Plectasin, a fungal defensin, targets the bacterial cell wall precursor Lipid II. *Science* **328**, 1168-1172 (2010).

2   Münch, D. *et al.* Identification and in vitro analysis of the GatD/MurT enzyme-complex catalyzing lipid II amidation in Staphylococcus aureus. *PLoS pathogens* **8**, e1002509 (2012).

3   Huster, D., Yao, X. & Hong, M. Membrane protein topology probed by 1H spin diffusion from lipids using solid-state NMR spectroscopy. *Journal of the American Chemical Society* **124**, 874-883 (2002).

4   Ratledge, C. & Wilkinson, S. G. *Microbial lipids*. Vol. 2 (Academic Pr, 1988).

5   Chen, H. *et al.* Design and pharmacodynamics of recombinant NZ2114 histidine mutants with improved activity against methicillin-resistant Staphylococcus aureus. *AMB Express* **7**, 46 (2017).

6   Etzkorn, M., Böckmann, A., Lange, A. & Baldus, M. Probing molecular interfaces using 2D magic-angle-spinning NMR on protein mixtures with different uniform labeling. *Journal of the American Chemical Society* **126**, 14746-14751 (2004).

7   Kramer, N. E. *et al.* Resistance of Gram-positive bacteria to nisin is not determined by lipid II levels. *FEMS microbiology letters* **239**, 157-161 (2004).

8   Bajaj, V. S., Mak-Jurkauskas, M. L., Belenky, M., Herzfeld, J. & Griffin, R. G. Functional and shunt states of bacteriorhodopsin resolved by 250 GHz dynamic nuclear polarization–enhanced solid-state NMR. *Proceedings of the National Academy of Sciences* **106**, 9244-9249 (2009).

9   Voinov, M. A. *et al.* Cysteine-specific labeling of proteins with a nitroxide biradical for dynamic nuclear polarization NMR. *The journal of physical chemistry B* **119**, 10180-10190 (2015).

10   Kaplan, M. *et al.* EGFR dynamics change during activation in native membranes as revealed by NMR. *Cell* **167**, 1241-1251. e1211 (2016).

11   Oeemig, J. S. *et al.* Eurocin, a new fungal defensin structure, lipid binding, and its mode of action. *Journal of Biological Chemistry* **287**, 42361-42372 (2012).

12   Essig, A. *et al.* Copsin, a novel peptide-based fungal antibiotic interfering with the peptidoglycan synthesis. *Journal of Biological Chemistry* **289**, 34953-34964 (2014).

13   Yang, Y. *et al.* Characterization of recombinant plectasin: solubility, antimicrobial activity and factors that affect its activity. *Process biochemistry* **46**, 1050-1055 (2011).

14   Frieden, E.   (ACS Publications, 1985).

15   Jaroniec, C. P. Structural studies of proteins by paramagnetic solid-state NMR spectroscopy. *Journal of Magnetic Resonance* **253**, 50-59 (2015).

16   Weingarth, M., Bodenhausen, G. & Tekely, P. Low-power decoupling at high spinning frequencies in high static fields. *Journal of Magnetic Resonance* **199**, 238-241, doi:10.1016/j.jmr.2009.04.015 (2009).

17   Weingarth, M., Demco, D. E., Bodenhausen, G. & Tekely, P. Improved magnetization transfer in solid-state NMR with fast magic angle spinning. *Chemical Physics Letters* **469**, 342-348 (2009).

18   Fung, B. M., Khitrin, A. K. & Ermolaev, K. An improved broadband decoupling sequence for liquid crystals and solids. *Journal of Magnetic Resonance* **142**, 97-101 (2000).

19   Doherty, T. & Hong, M. 2D 1H-31P solid-state NMR studies of the dependence of inter-bilayer water dynamics on lipid headgroup structure and membrane

peptides. *J Magn Reson* **196**, 39-47, doi:10.1016/j.jmr.2008.10.001 (2009).

20   Weingarth, M. *et al.* Supramolecular Structure of Membrane-Associated Polypeptides by Combining Solid-State NMR and Molecular Dynamics Simulations. *Biophys J* **103**, 29-37, doi:10.1016/j.bpj.2012.05.016 (2012).

3

CHAPTER 4

Design parameters of tissue engineering scaffolds at atomic scale

Abstract

Stem cell behaviour is critically regulated by the material properties of the surrounding extracellular matrix, which has important implications for the design of tissue engineering scaffolds that act as biomimetic stem cell substrates and offer fascinating applications in regenerative medicine. However, our understanding of stem cell scaffolds is strongly limited because our knowledge of their material properties is confined to nanoscopic-to-macroscopic length scales. Here, we present a solid-state NMR approach that provides atomic scale information on complex stem cell substrates at near physiological conditions and at natural isotope abundance. Using a series of self-assembled peptidic scaffolds designed for nervous tissue regeneration, we introduce the molecular order and assembly degree as new critical design parameters for stem cell scaffolds, and we show at atomic scale how scaffold assembly degree, mechanics, and homogeneity correlate with favorable stem cell behaviour. Furthermore, integration of solid-state NMR data with molecular dynamics simulations reveals a highly ordered fibril structure as the most favourable stem cell scaffold. Altogether, our approach provides a high-resolution perspective that could critically improve the design of tissue engineering scaffolds and other self-assembled biomaterials.

Introduction

Stem cells respond to their microenvironment that provides critical cues for their migration, differentiation, and proliferation[1-5]. The regulatory interplay between stem cells and their native extracellular matrix has important implications for the design of biomimetic tissue engineering scaffolds, with potentially exciting applications in regenerative medicine that could lead to a paradigm shift in therapeutic treatments[6-10]. In order to improve our capabilities in engineering tissues, in-depth understanding of properties of stem cell substrates is essential[2,4,10-12]. Furthermore, it has been recognized by cell biologists that designer matrices and a better understanding of these matrices are critical for progress in translational research with stem cells and organoids[13].

Commonly, nano- or macroscale biophysical tools are used for the characterisation of biomimetic stem cell substrates[3]. However, information at the atomic scale is very scarce, although such information could critically improve the design of stem cell substrates, and enable to distinguish materials that exhibit similar properties on higher length scales[5]. Indeed, atomic scale information could enable stem cell substrates with optimized biomechanical parameters[14,15], improved exposure of functional motifs[16], better cross-linking strategies[10,17], tuned nanotopography[18], or the inclusion of stimuli-responsive elements[19].

In this work, we discover novel design parameters for neural tissue scaffolds using solid-state Nuclear Magnetic Resonance (ssNMR), a technique that enables the characterisation of soft matter at atomic-level and at close-to physiological conditions. We studied a series of peptidic hydrogels that were designed to self-assemble into biocompatible scaffolds for the treatment of spinal cord injury (SCI)[20], a damage for which no medical cure is available, yet a growing body of evidence suggests that biomechanical cues can guide SCI repair[21,22]. The peptides display variants of the bone marrow homing peptide 1 (BMHP1) functional motif that stimulates interactions with neural stem cells, and some peptides feature an N-terminal biotin tag to foster self-assembly (Table 1). The most favourable hydrogels showed attractive self-healing properties, stimulated human neural stem cell (hNSC) viability and differentiation *in vitro*, and showed regenerative potential *in vivo* in a rodent model of SCI[20].

Here, using an NMR approach that works at natural isotope abundance and enables the fast screening of complex materials, we present decisive molecular determinants that directly correlate with hNSC viability. Highly astonishingly, we demonstrate that the homogeneity and the self-assembly degree of the tissue scaffold are critical new design parameters for stem cell viability. Moreover, using an advanced ssNMR setup that works with as little as

60 nmol of unlabelled material, we succeed to understand how supramolecular structures of stem cell substrates relate to favourable functional properties, which we correlate to macroscopic AFM and rheology data. Altogether, our study presents ssNMR as a broadly applicable high-resolution technique to gauge tissue engineering scaffolds that, in combination with other methods, enables a holistic characterisation of stem cell substrates from the atomic to the macroscopic length scale.

Mechanical characterisation at atomic scale

We prepared a series of self-organized BMHP1-peptide hydrogels at a concentration of 3% w/v (Table 1). First, we analysed the mechanical properties of the highly hydrated samples using high-resolution ssNMR. Therefore, we quantified the rigid and dynamic fractions of the hydrogels using one-dimensional (1D) so-called dipolar NMR experiments (i.e., experiments that rely on the presence of dipolar couplings between ^{1}H and ^{13}C) that detect immobile molecular components, and scalar NMR experiments that report on mobile components with pronounced fast pico-to-nanosecond dynamics that do not form stable, large assemblies (Figure 1A, B).

Remarkably, our experiments, which were performed without synthetic ^{13}C-isotope enrichment, revealed clear mechanical differences between the hydrogels. The hydrogels formed by peptides 2 (dubbed hydrogel 2) and B26 gave intense scalar spectra and virtually no dipolar signal. This implies that peptides in these two hydrogels are *highly mobile*, weakly associated, and do not form larger aggregates. We confirmed that the scalar spectra of the hydrogels relate to fast tumbling small assemblies or free peptides by solution NMR measurements of free peptides that yielded exactly the same signals (Figure S1). In stark contrast, the biotinylated hydrogels B3, B15, and B24 gave intense dipolar spectra and very faint scalar signals, implying high rigidity and high assembly-degrees. Intriguingly, the rigid hydrogels B15 and especially B24 performed best in cell viability assays in which the BMHP1-derived scaffolds were used as substrates to culture hNSC, a well-standardized source of somatic human stem cells for *in vitro* testing of peptidic biomaterials[20,23,24], while the mobile hydrogels exhibited no significant difference to the negative control (Figure 2). Thereby, our data strongly suggest that the appropriate mechanical stiffness at the molecular level of the hydrogel is a crucial functional factor.

Remarkably, only in hydrogel B24, the best performing stem cell substrate, virtually all scalar signals completely disappeared. In addition, the aromatic Phe5 sidechain in the middle of the peptides, which mutational studies suggest to be a hot spot for peptide assembly, is only completely rigidified in scaffold B24[25]. This implies that all peptides are firmly assembled in hydrogel B24, which strongly suggests being favourable for the culturing of hNSC, and which

we investigate below in detail.

The build of the peptides in the scaffold.

Name	Peptide Sequence	ssNMR analysis (hydrogel)
2	Acetyl-GGGPFSSTKT-CONH2	highly mobile
B3	Biotin-GGGPFSSTKT-CONH2	rigid
4	Acetyl-WGGGPFSSTKT-CONH2	mobile
B15	Biotin-GGGAFSSTKT-CONH2	rigid
B24	Biotin-GGGAFASTKT-CONH2	rigid
B26	Biotin-GGGPFASTKT-CONH2	highly mobile
30	Acetyl-WGGGAFASTKT-CONH2	mobile
31	Acetyl-WGGGAFSSTKT-CONH2	mobile

Table 1. List of BMHP1-derived peptides and ssNMR analysis of the hydrogel-mechanics. The hydrogel classification is based on the signal intensities in Figure 1. *Rigid* hydrogels give intense dipolar and faint scalar signals, respectively, while *mobile* hydrogels give faint dipolar and intense scalar signals. Hydrogels 2 and B26 were classified as *highly mobile* because they showed by far the strongest scalar and no or vanishingly small dipolar signals.
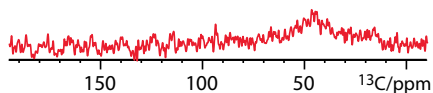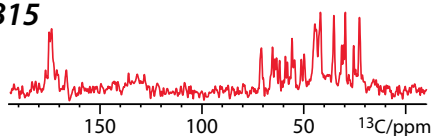
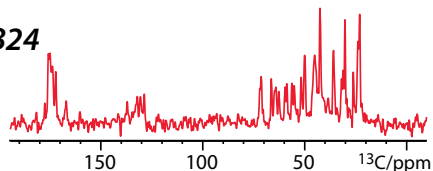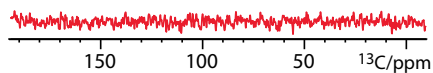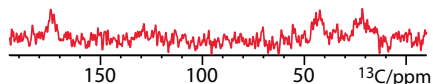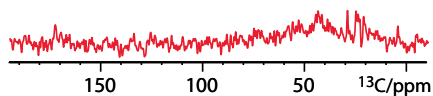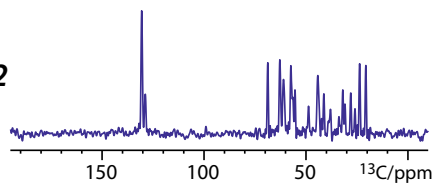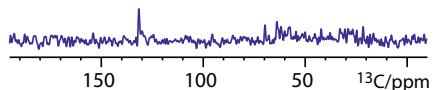4

A *dipolar (rigid)*

2
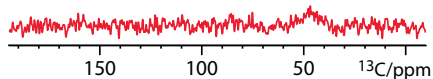
B3
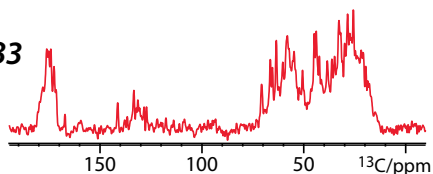
4

B15

B24

B26

30

31

B *scalar (mobile)*

2

B3

4
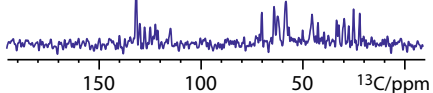
B15
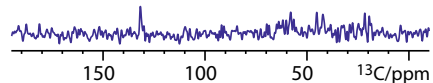
B24
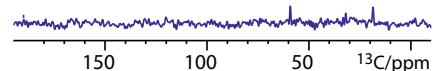
B26

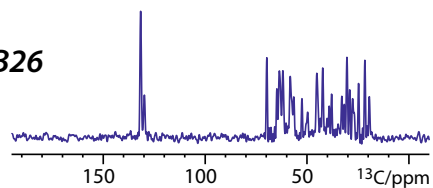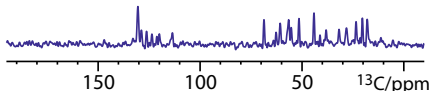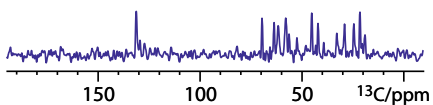30

31

Figure 1. The mechanical properties of the hydrogels at atomic scale. A) ^{13}C-detected dipolar cross-polarization ssNMR spectra that characterise the immobile fraction of the hydrogels. B) ^{13}C-detected scalar INEPT ssNMR spectra that characterise dynamic molecular components with fast nanosecond motion and large amplitudes. All spectra were acquired at 500 MHz, 10 kHz magic angle spinning (MAS), and at 280 K sample temperature.
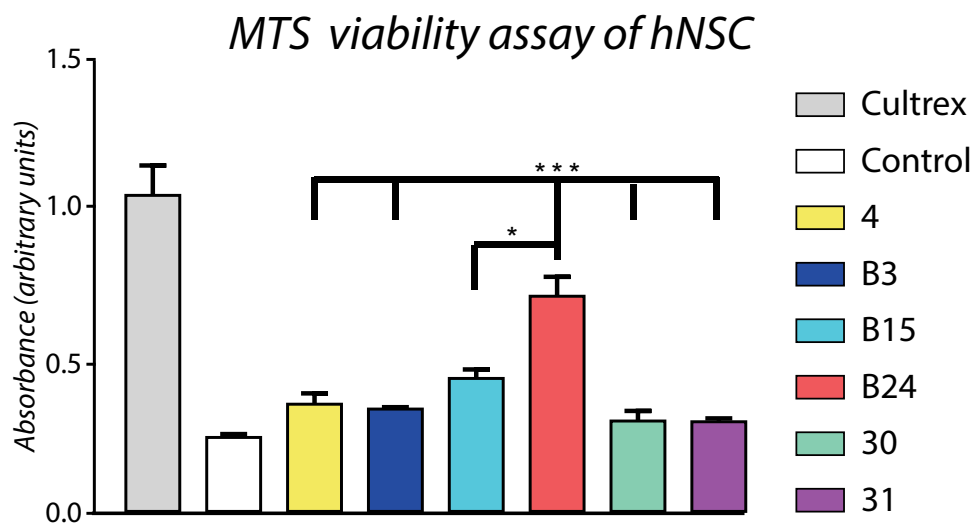
Figure 2. MTS viability assay of hNSC seeded on BMHP1-peptide hydrogels. Results, comprising Cultrex and bare plastic-surface (control), showed significant differences between hydrogel B24 compared to other peptide hydrogels (***p<0.001) and control (not shown in the graph). Cultrex showed significant differences against all samples (***p<0.001, not shown). Scaffolds B3, 4, 30 and 31 exhibited no significant cell viability difference to the negative control. The error bars show the standard deviation. Figure adapted from Gelain et al.[20]

As a next step, we investigated the impact of the molecular build on the functional properties. Therefore, we sought to quantitatively assign the NMR chemical shifts, which are delicate reporters of peptide conformation[26]. However, quantitative chemical shift assignments of solid-like decameric peptides with complex tags critically require two-dimensional (2D) spectra. Unfortunately, such spectra usually necessitate isotope enrichment, which drastically limits the applicability of NMR because of severely increased material costs and the high complexity to label certain materials. Here, we demonstrate extensive proton and carbon assignments of solid-like hydrogels at natural isotope abundance and physiological temperatures using a ^{1}H-detected ssNMR setup that strongly increases signal sensitivity and requires less than 75 mg (60 nmol) of unlabelled peptide[27-35]. To best of our knowledge, this is the first time that ^{1}H-detected ssNMR was successfully used to quantitatively assign solid-like peptide hydrogels at natural abundance, something that suggests being a highly

promising technique to quantify such materials in the future.

We acquired a ^{1}H-detected dipolar 2D ^{13}C-^{1}H correlation spectrum of scaffold B24 at 800 MHz magnetic field and 60 kHz MAS (Figure 3A). We carefully verified that the signal positions were exactly the same at 15 and 60 kHz MAS, demonstrating that the scaffold is not modulated by the sample spinning frequency (Figure S2). The 2D ^{13}C-^{1}H spectrum exhibited a very favourable spectral resolution and we could readily identify most of the signals by their characteristic chemical shifts. Such fingerprint signals were the G1-3 CαHα, Phe5 CβHβ, Ser7 CβHβ, alanine/threonine CαHα, and CβHβ. The Ser7 CαHα signal could be unambiguously identified by comparison with hydrogel B15 that has two serine residues and features a much stronger signal at 57 ^{13}C ppm. We could also assign the biotin-tag, which provided detailed insights into its molecular role in the hydrogel. A comparison with solution NMR spectra of free B24 peptides shows significant chemical shift perturbations of more than one ppm for several biotin carbons (C2, C3, C6, and C9) (Figure S3)[36], demonstrating that biotin changes its conformation in the hydrogel. These data imply that biotin is actively involved in the self-assembly procedure and most likely rigidly packed in the hydrophobic core, agreeing with the critical role of biotin for the formation of rigid hydrogels (Figure 1). With these extensive assignments, we were able to determine the conformation of the assembled B24 peptides at high-resolution (Figure 3B, C). This analysis revealed that residues A4-F5-A6-S7-T8-K9 adopt β-strand conformation in hydrogel B24, while residue T10 has reduced β-strand propensity. Note that the free peptide B24 adopts random coil structure (Figure S4).

The order of the scaffold as a novel design parameter

With the help of our detailed structural knowledge of B24, we sought to understand the build of the other, functionally less favourable hydrogels. Particularly, we hypothesized that further, thus far ignored, material properties exist which critically influence the use of hydrogels as hNSC substrates. Indeed, while an appropriate rigidity (usually between 100 and 1.000 Pa at the macroscale) is important for neural tissue engineering scaffolds[37], rigidity is clearly not the only decisive factor: while hydrogels B3, B15, and B24 all showed high rigidity in ssNMR spectra, B15/B24 outperformed hydrogel B3 in cell viability assays (Figure 2)[20]. We decided to acquire dipolar spectra for a selection of five hydrogels (2, B3, B15, B24, 30) at a very high magnetic field of 950 MHz, which strongly improves NMR spectral quality (Figure 3E). Indeed, at 950 MHz, we succeeded to quantitatively understand the molecular build of the hydrogels, and we demonstrate that the sample homogeneity and assembly degree are new material property of striking importance.

At 950 MHz, hydrogels B15 and B24 yield very similar dipolar spectra with many remarkably sharp (<0.3 ^{13}C ppm) signals, demonstrating that both scaffolds are highly ordered and adopt extended conformations from residues Ala4 to Thr10. However, while B24 shows virtually no sign of heterogeneity, a number of B15 signals such as Lys9 and Thr10 in the functional C- terminus are broadened (Figure 3D). Especially the critical residue Phe5 shows increased heterogeneity for both Cα (0.58 and 0.34 ^{13}C ppm in B15 and B24, respectively) and Cβ (0.66 and 0.21 ^{13}C ppm in B15 and B24, respectively). Intriguingly, the increased disorder of Phe5 correlates with residual scalar signal of Phe5 in B15 and the reduced assembly degree of B15 (Figure 1), while all peptides are assembled in the extraordinarily homogeneous scaffold B24. Surprisingly, our 950 MHz data reveal that scaffold B3 is a polymorph (Figure 3E) that consists of i) a dominant ordered conformation with sharp signals (0.3-0.4 ^{13}C ppm) and ii) a multitude of unstructured peptides that give very broad signals. The polymorphism of B3 is readily visible by the broad signal feed and the signals in the spectral region below 20 ^{13}C/ppm that corresponds to unstructured peptides and is empty in B15/B24. Most likely, the heterogeneity of B3 results from the proline residue in the middle of the peptide, which impedes the formation of ordered supramolecular structures, and which is replaced by an alanine in B15 and B24. The observed sample heterogeneity can either relate to static molecular disorder and/or slowly exchanging conformations. Notably, the functional C-terminal BMHP1 motif that fosters stem cell contacts changes from β-strand to coil conformation in hydrogel B3, as we can unambiguously determine from the lower chemical shifts of Thr8β/Thr10β (70.9/70.4 and 72.1/71.4 ^{13}C ppm in B3 and B24, respectively) and the much higher shifts of Lys9Cα (54.8 and 51.7 ^{13}C ppm in B3 and B24, respectively). Most importantly, the reduced secondary structuring and decreased order that we observe in scaffold B3 and other stem cell scaffolds (see below) correlate with less favourable functional properties (Figure 2). Future atomic-scale studies with other designer stem cell scaffolds would be highly insightful to gauge and generalise our findings[13].
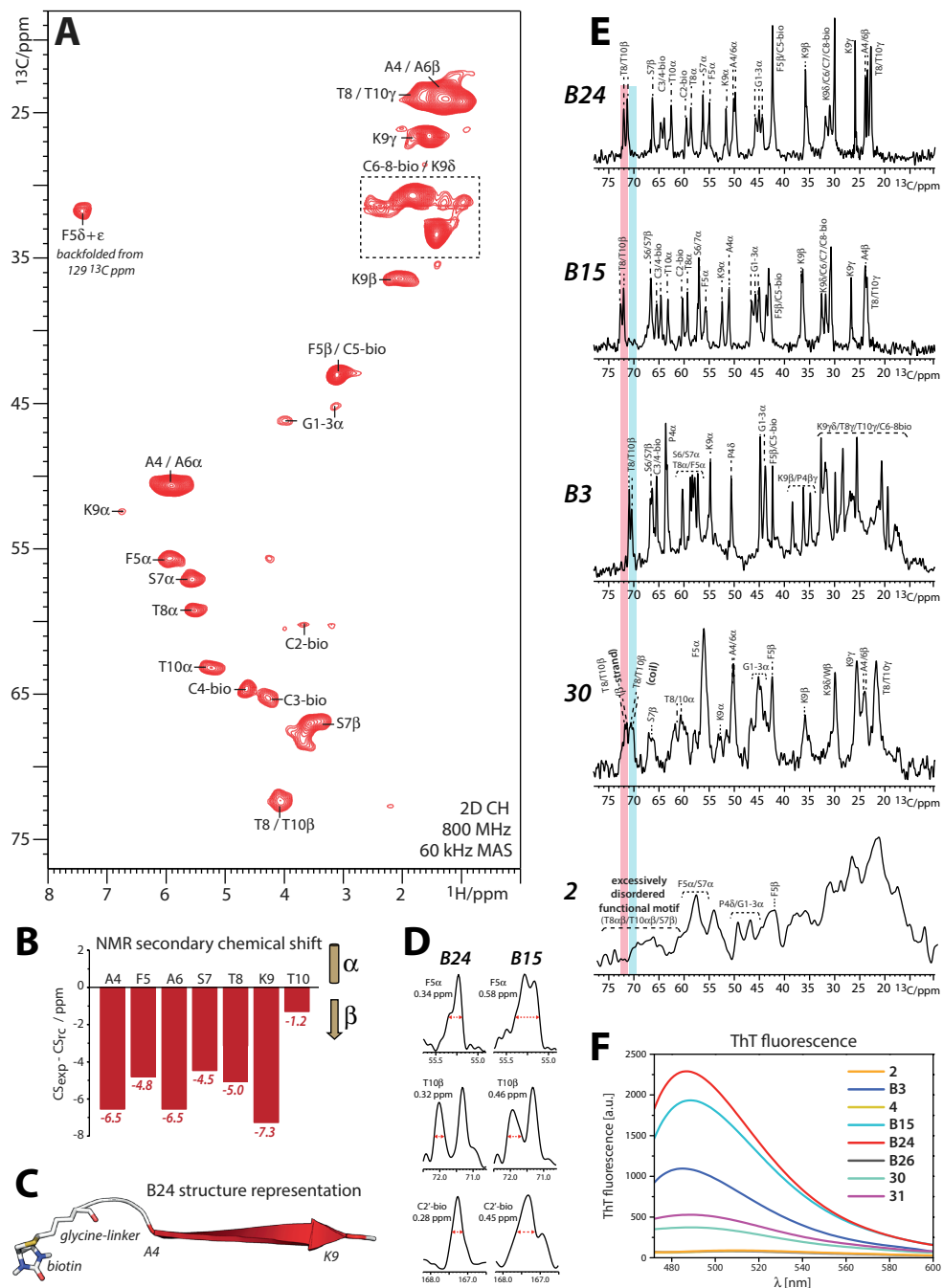
**Figure 3. The conformation and dispersity of the assembled peptides at high-resolution.** A) ^{1}H-detected 2D ^{13}C-^{1}H spectrum of hydrogel B24 at natural abundance, acquired at 800 MHz using 60 kHz MAS and 305 K sample temperature. B) [Cα-Cβ] secondary chemical shift (SCS)[26] analysis reveals pronounced β-strand conformation

for residues A4-T10. C) Structural representation of the assembled peptide B24 derived from ssNMR. D) Cross-sections of ^{13}C dipolar signals of B24 (left panel) and B15 (right). The linewidth at half-height is indicated. E) SSNMR spectra of hydrogels 2, B3, B15, B24, and 30 acquired at 950 MHz using 15 kHz MAS. 30.000 signals were accumulated for the rigid hydrogels (B3, B15, B24), and 180.000 accumulations for the mobile hydrogels 30 and the very mobile hydrogel 2. Spectra were processed with exponential line-broadening (10 Hz for B3, B15, B24; 30 Hz for hydrogel 30; 200 Hz for hydrogel 2). The red and blue bars mark threonine residues in extended and coiled structures, respectively. F) ThT fluorescence measurements of the hydrogels.

We also acquired dipolar spectra at 950 MHz for the mobile hydrogel 30 and the highly mobile hydrogel 2 in order to understand the molecular properties of the small rigid fractions of these scaffolds with low assembly degrees (Figure 3E). Since the rigid fractions are the minor fractions in mobile and very mobile hydrogels, we required drastically longer measurement times (180.000 signal accumulations/sample, i.e., 5 days for each sample) in order to obtain clear dipolar signals. Signals of hydrogel 30 were generally much broader than for B24, which relates to a markedly increased heterogeneity of the assembly. Intriguingly, as can be unambiguously deduced from the doubling of Thr8β/Thr10β signals and the characteristic chemical shifts of these signals[38], hydrogel 30 exhibits both coiled and extended conformations for the functionally critical C-terminus. The substantial disorder of the C-terminus is also readily visible from the Ser7β signal, which is more than four times wider in hydrogel 30 than in B24 (1.43 and 0.34 ^{13}C ppm in hydrogels 30 and B24, respectively). This situation is even more pronounced for in dipolar spectra of the highly mobile hydrogel 2. While the assembly domain in hydrogel 2 around Phe5 features starkly broadened yet still discernible signals, the functional C-terminus (residues Ser7, Thr8, and T10) is extremely disordered and almost broadened beyond detection. Thereby, our quantitative ssNMR analysis demonstrates that the peptide heterogeneity correlates with lower assembly degree, i.e., with more intense scalar signals (Figure 4). This conclusion is confirmed by ThT measurements that very clearly show that increasing homogeneity/order of the ssNMR spectra goes hand in hand with an increase in ThT fluorescence, i.e., with an increase in stable β-structured assemblies (Figure 3F). Most importantly, peptide order directly correlates with favorable functional properties (Figure 2). Altogether, these findings demonstrate that the conformational homogeneity and the assembly degree are novel, vital functional factors for peptidic tissue engineering scaffolds. Interestingly, the recently reported fibers assembled from the gel-forming MAX1 peptide also show an intriguing homogeneity with a single molecular conformation[39], and these assemblies also exhibit remarkable mechanical bulk stability[40].
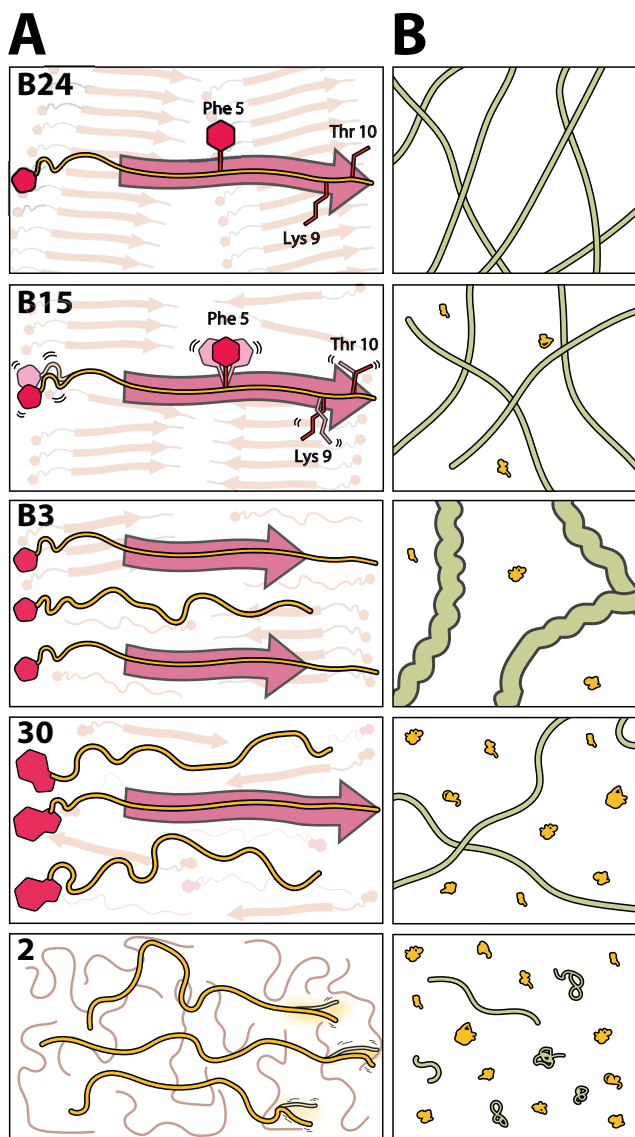
Figure 4. Structuring and assembly from ssNMR. A) Illustration of the building blocks that form fibers and large assemblies. Illustration is based on the dipolar ssNMR data reported in this study. B) The assembly degree of the hydrogels; derived from comparative dipolar and scalar ssNMR data. Strings illustrate fibers that give dipolar NMR signals, while the yellow shapes relate to small assemblies that give scalar signals. The relative thickness of the fibers was derived from AFM data (see below).
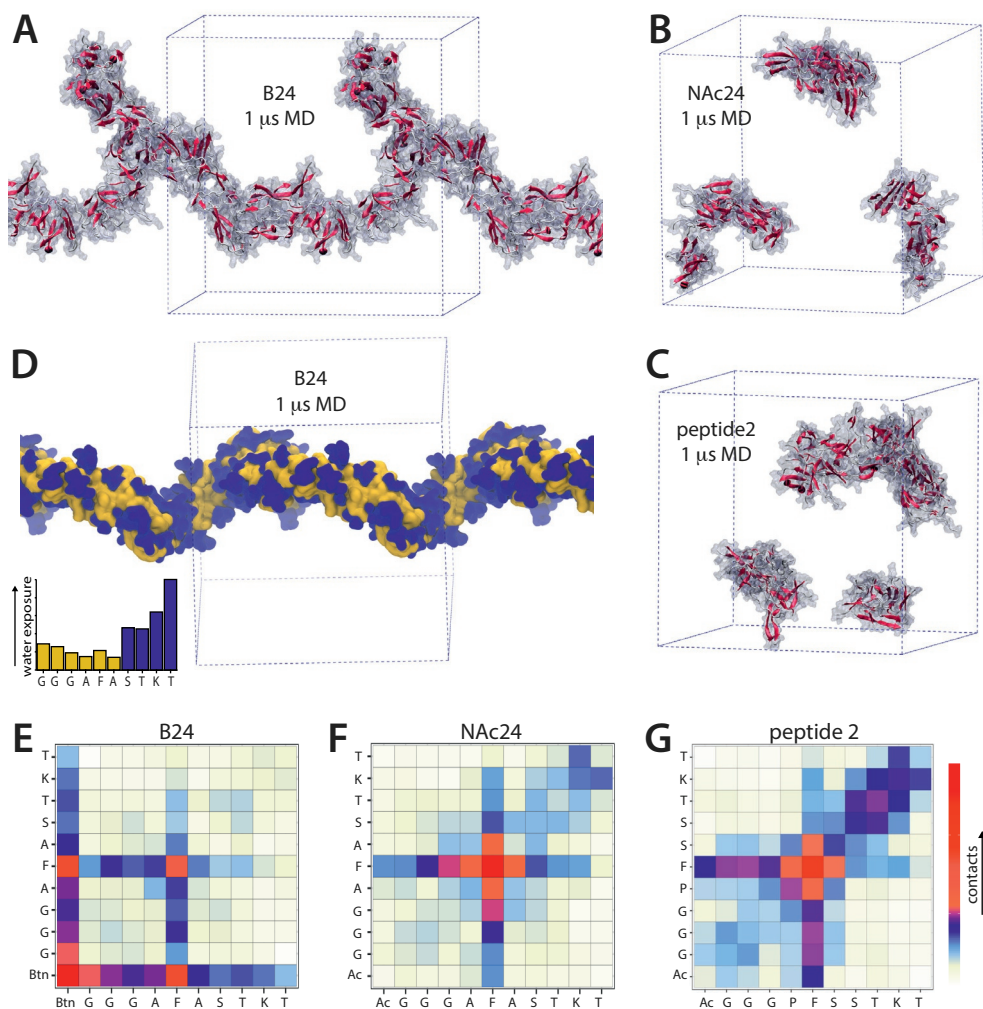
The supramolecular organisation of the scaffolds

To gain insights into the global arrangement and self-assembly pathway of the hydrogels, we sought to use long and large-scale restrained atomistic molecular dynamics (MD) simulations (see Supporting Information for details). Initially, we focused on the functionally most favourable hydrogel B24.[41,42] In order to steer the assembly behaviour, we integrated the ssNMR secondary structure information into the MD simulation via TALOS+[43], a widely used software that derives torsional angles from chemical shifts. We simulated the self-organization of one hundred B24 peptides that were initially randomly distributed in a water-filled box. The peptides rapidly formed smaller clusters within 50 ns. Interestingly, due to the preference for β-strand conformation and their amphiphilic nature, the peptides mostly assemble to extended formations (Figure S5). These stretched clusters then unite to an elongated fiber-like construct reminiscent of the flat B24 fibers previously observed by AFM[20]. The resulting fibrous assembly spans through the entire simulation box and exhibits a high β-strand content (Figure 5A), in line with ssNMR data.

Next, we analysed the fiber organisation. A molecular contact map (Figure 5E) shows that biotin and Phe5 are the two major intermolecular hot-spots. These data demonstrate that the aromatic rings engage in intense π-stacking, and that Phe5 and biotin are mutually packed into the core of scaffold B24, which agrees well with our ssNMR results (Figures 1 and 3), and matches with X-ray powder diffraction data[25]. Intriguingly, the functional C-terminus is substantially less involved in peptide-peptide interactions, and hence available to engage in contacts with cellular receptors. Indeed, a calculation of the water exposure shows that hydrophobic N-terminus is buried in the fiber core, while the C-terminal BMHP1 motif forms the functional surface (Figure 5C).

To understand the role of biotin, we replaced biotin by an acetyl-tag and performed another simulation of similar size and duration. Furthermore, we did a similar simulation for peptide 2. Interestingly, the acetylated peptides also aggregated to smaller cluster that, however, did not stably combine to longer fiber-like constructs (Figure 5B, D). This observation strongly suggests that biotin critically stimulates the transition from small stretched cluster to elongated fibers, which agrees well with our ssNMR data and explains why we see substantially weaker dipolar signals for peptide 2 and all peptides without a biotin-tag. Remarkably, in the biotin-less peptides 2 and NAc24, the functional C-terminus is much more strongly involved in packing interactions, which is presumably detrimental for its availability as focal point for cellular contacts (Figure 5F, G). In particular, for peptide 2, the C-terminus shows wide latitude of intermolecular interactions, explaining the strong broadening of the peptide 2 C-terminus in NMR spectra (Figure 3E). Remarkably, residue Pro4 in peptide 2 increases the disorder, which matches with the polymorphism in hydrogel B3

that features a proline at the same position(Figure 3D).

Figure 5. The supramolecular organization. A) B24 fiber-like assembly after 1 μs of restrained atomistic MD simulation. B) Replacing the biotin-tag by an acetyl-tag markedly reduces the self-organization tendency. C) Peptide 2 also shows reduced self-organization tendency. D) The functional C-terminus (S7-T8-K9-T10, shown in blue) is surface-accessible in the B24 fiber-assembly. The N-terminal residues G1-F6 and biotin are coloured in yellow. The insert shows the water-exposure derived from the MD simulation. E) Residual contact matrix derived from the B24 simulation using a 5 Å cut-off distance. F) Same as E), but for the N-acetylated peptide 24. G) Same as E), but for peptide 2.

Comparison to morphological and rheological properties

Finally, we sought to relate our atomistic insights to morphological and viscoelastic properties. Morphological hydrogel properties are typically studied with AFM. AFM data show that the highly ordered hydrogels B15 and B24 indeed exhibit a markedly different morphology compared to the heterogenous or mobile hydrogels (Figure 6A and Figure S6). Only peptides B15 and B24 assemble into flat tabular fibers, while B3 and the other peptides formed twisted fibers/protofibrils or more complex structures, which agrees with previous studies[20]. Interestingly, the height of 1.7 - 2.1 nm that we measured with AFM for the B24 fibers (Figure 6B) matches well to the height of the simulated B24 fiber-like assembly, which corroborates that our MD simulation is representative for the fiber formation. Our AFM data also showed that, compared to peptide B3, B15 and B24 self-organize into a more homogeneous network of nano-fibers. Such a dense three-dimensional fiber-network better resembles the typical features of the native proteins of the extracellular matrix[44], and this may be one of the reasons why hydrogels B15 and B24 are more suitable as proregenerative substrates. In agreement with our ssNMR data, hydrogel 2 only formed sparse nano-dots but no fibers, while hydrogel 30 showed a much lower fiber density (Figure S5). Intriguingly, B15 and B24 give basically the same AFM morphologies at the nano-scale, however, while atomic scale ssNMR data show critical differences.
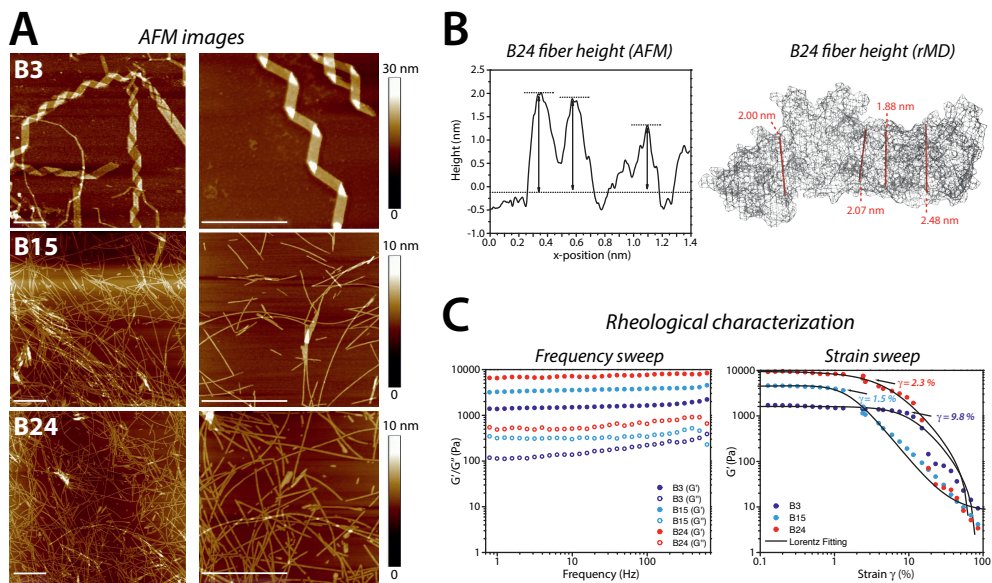
Figure 6. Morphological and rheological characterization. A) AFM analysis. Peptide B3 assembles into shorter twisted protofibrils, while peptides B15 and B24 form long tabular fibers (scale bar 1μm). B) *(left panel)* AFM height measurement of scaffold

B24 ranging from 1.7 nm to 2.1 nm. (*right panel*) We observed similar heights the B24 fiber in restraint MD (rMD) simulation. C) *(left panel)* Rheological characterization of solutions of assembled peptides B3, B15, and B24 were monitored by frequency sweep tests (0.1-1000 Hz) at low strains (1%). The assemblies showed typical hydrogel-like profiles featuring a predominant elastic solid-like behavior (G', solid dots), as compared with the viscous component (G", empty dots). *(right panel)* In strain-to-failure tests, hydrogels B15 and B24 are less prone to deformation than B3.

Rheological measurements of the storage (G') and loss (G") moduli are commonly used to characterise viscoelastic and mechanical properties of hydrogels. Here, G' reflects the stiffness, while G" represents the energy dissipated during the oscillatory test and correlates with the liquid-like response of the hydrogel. The ratio between G' and G" provides insights into the viscoelastic profile, i.e., whether a material behaves as an elastic solid (G'>G") or a viscous liquid (G'<G")[45]. The assemblies of peptides B3, B15, and B24 showed typical hydrogel-like profiles, featuring a predominantly elastic solid-like behavior (G') relative to the viscous component (G") (Figure 6C, left panel), matching with our previous studies[20]. In contrast, the assemblies formed by peptides 2, 4, B26, 30, and 31 showed substantially lower G' values, implying softer hydrogels and a weaker tendency to assemble (Figure S7). These data agree very well with our quantitative ssNMR analysis (Table 1, Figures 1, 3E, 4).

We were particularly interested to compare the three rigid hydrogels in order to explore if the polymorphism of scaffold B3 is reflected in rheological properties. In comparison to B3 (G' value of 1526 Pa), hydrogels B15 and B24 showed more pronounced solid-like properties with an elastic shear modulus G' of 3606 Pa and 7131 Pa, respectively. Next, we performed strain-to-failure tests in order to assess the hydrogels failure when subjected to a linear strain progression (Figure 6C, right panel). In line with its lower G' value, B3 showed a strain-to-failure value of 9.8% (corresponding to a stress-to-failure of 13.24 Pa), while hydrogels B15 and B24 exhibited markedly less deformation before failure (1.5% and 2.3%, respectively) together with higher stress-to-failure values (89.07 Pa and 228.3 Pa, respectively). Notably, these results suggest that the higher stability of hydrogels B15/B24 relates to their much higher molecular order that we observe with ssNMR. Here, the higher bulk mechanical stability of hydrogels B15/B24 likely relates to an optimal molecular packing, maximizing interresidual and intermolecular contacts[40], while the packing is compromised in disordered samples, which can be associated with reduced mechanical stability[46]. Altogether, we demonstrate that ssNMR, AFM, and rheology provide highly complementary insights at different length scales into the material and functional properties of tissue engineering scaffolds.

Conclusions

Here, we have integrated solid-state NMR and MD simulations to characterise the mechanical, topological, and molecular properties of tissue engineering scaffolds at atomic scale. Importantly, thanks to modern ^{1}H-detected ssNMR methods that we apply here on tissue engineering scaffolds for the first time to best of our knowledge, our approach works without synthetic isotope enrichment and thereby enables studies at low costs and with hard-to-label materials such as cross-linkers or chemical modifications. On the example of functionalised hydrogels for the treatment of SCI, we were able to relate material and molecular parameters to the viability of hNSC. Intriguingly, we established that the complete assembly of all peptides to a highly ordered matrix is highly favourable for hNSC survival. Thereby, the assembly degree as novel design parameters. Moreover, for the first time, we demonstrate that the molecular homogeneity of the scaffold relates to favourable functional properties. The order of the stem cell scaffold presumably enables an optimal exposure of the functional BMHP1 motif that fosters beneficial interactions with hNSC[20], while the exposure of the BMHP1 motif is suboptimal in disordered scaffolds due to a distribution of favourable and unfavourable conformations. In the functionally most beneficial hydrogels, homogeneity is achieved by the removal of prolines from the BMHP1 motif. This is a particular noteworthy finding, given that collagen, the major fibrillar protein of the natural extracellular matrix, has a high content in proline (~10 %)[47] yet features only moderate adhesion and differentiation potential for NSC *in vitro*[48]. Interestingly, pioneering solid-state NMR studies of bone collagen and cartilage[47,49-57] show that prolines are involved in expansion joints that confer flexibility to collagen fibers[58], which is vital for the functional mechanics of these native tissues. This finding would suggest that different cell types require different material properties at the atomic length scale, opening the door to future investigations of novel biomaterials dedicated for other targeted tissues. Finally, we like to emphasize that the correlations of scaffold homogeneity and assembly degree with favourable functional properties are *de novo* findings that do not relate to previous studies. Moreover, while it is well known that the mechanical properties of stem cell scaffolds correlate with the functional performance of biological and designer matrices[5], we show here, for the first time ever, that the rigidity at the molecular level also correlates with function. This is an important new finding, given that macroscopic characterizations of material properties only provide an average over atomistic, nanoscopic, and microscopic scales. Eventually, we also like to underscore that previous microscopic biophysical characterizations did not succeed to quantify the molecular differences of the stem cell scaffolds discussed in this study[20]. The latter clearly speaks in favour of ssNMR as a powerful additional tool to understand the properties of designer matrices at physiological conditions. Thereby, the integration of microscopic and macroscopic data with atomistic

ssNMR data promises a markedly enhanced and holistic understanding of the material properties of designer stem cell matrices.

In this regard, the future challenge is to characterise tissue engineering scaffolds in the presence of stem cells at the atomic length scale. Here, ssNMR, in combination with advanced detection, enhancement, and sample preparation schemes for complex cellular samples such as dynamics nuclear polarization[53,59-61], ultrafast MAS[28], and ^{19}F-labelling[62,63] could be an ideal tool to enhance our knowledge on interactions between stem cells and their substrates at physiological conditions, and to generally improve our understanding of the composition of bone and tissue materials. Altogether, on the example of peptic hydrogels designed for neural tissue regeneration, we have presented a broadly applicable approach to study tissue engineering scaffolds at the atomic length scale.

Materials and methods

Sample preparation. Peptides were synthesized by solid-phase Fmoc-based chemistry on Rink amide 4-methyl-benzhydrylamine resin (0.5 mmol g^{-1} substitution) by using the Liberty-Discovery (CEM) microwave automated synthesizer. Peptides were subsequently purified via Waters binary HPLC apparatus.[20] The peptides for NMR analyses were dissolved in distilled water (GIBCO) at a concentration of 3% (w/v). After 24h, 10% (v/v) of PBS (Ca^{2+}/Mg^{2+} free) was added to the samples. For the solution NMR measurements of unassembled peptides, we diluted peptide solutions to a final concentration of 1.5 mM corresponding to <0.2 % (w/v), far below the ~1 % (w/v) critical concentration at which peptides show self-assembly.

NMR experiments. ^{13}C-detected dipolar cross-polarization (CP)[64,65] and scalar INEPT[66] 1D ssNMR experiments to probe the rigid and mobile fractions of the BMHP1-derived peptide-hydrogels were carried out in a magnetic field of 500 MHz ([1]H-frequency) with 10 kHz MAS at a sample temperature of 280 K. Samples were spun in 3.2 mm zirconia rotors (Bruker Biospin). ^{13}C-detected CP experiments at 950 MHz magnetic field were performed with 15 kHz MAS at 278 K sample temperature. SPINAL[67] was used for heteronuclear proton decoupling at both 10 and 15 kHz MAS. All ^{13}C-detected CP experiments were initially optimised on ^{13}C-labelled histidine, and the obtained parameters were then used for the hydrogels without further optimisation and using a ^{1}H to ^{13}C CP magnetization transfer time of 1 ms for all samples. A [1]H-detected dipolar 2D heteronuclear [13]C[1]H correlation experiment was performed at 800 MHz magnetic with 60 kHz MAS and a real temperature of approximately 305 K. The contact times for the first a second CP steps in the 2D experiments were 1.2 and 0.32 ms, respectively. A recycle delay of 0.81 s was used, together with 3.1 ms evolution time in the indirect dimension, and a total of 1600 scans was acquired.

Low-power PISSARRO[68] decoupling (15 kHz ^{1}H-amplitude) was used during all acquisition periods. The MISSISSIPPI scheme was used for water suppression[69].

Solution NMR experiments were performed at 750 and 900 MHz magnetic field. Solutions of peptides 4, 30, and B24 were assigned using 2D CH HSQC, 2D HH COSY and 2D HH TOCSY experiments. Moreover, we performed a 2D CH HSQC experiment on a biotin solution.

In vitro assays. Human neural stem cells (hNSC) were obtained in agreement with the guidelines of European Medicines Agency (EMA) and Agenzia Italiana del Farmaco (AIFA).[70] hNSC were expanded and cultured into 96 multiwells for seven days in vitro (7DIV).[20] Briefly, 40 μl of the peptide solutions previously dissolved in distilled water were placed in each well, then cell culture medium was gently added to obtain soft hydrogels covering the overall bottom well surface. After 30 mins, cell culture medium was replaced with new one. Cultrex-BME® substrate and untreated-bottom well surface were used as positive and negative controls, respectively. At 7DIV, tetrazolium compound MTS (Promega) was used to evaluate cell viability. MTS solution was added to the culture media at concentration of 20% and incubated for 1 h at 37°C. The absorbance, directly related to the number of viable cells, was detected at 490 nm by using Vmax microplate reader (Molecular Devices, Sunnyvale, CA). Data (n=5) were processed using GraphPad Prism7 software and evaluated through one-way ANOVA followed by Tukey post test. Statistical significance was accepted $p<0.05$.

Molecular Dynamics simulations. All the simulations were performed in GROMACS version 4.6.3[71], using the GROMOS 53a6 force field[72] and a temperature of 300 K together with a 2 fs timestep. For the starting configuration, one hundred peptide molecules were placed into a cubic box with an edge length of 140 Å, and subsequently solvated with SPC water molecules. Furthermore, 100 mmol of Na$^+$ and Cl$^-$ ions were added to the system, yielding a total atom number of >266000 for each the B24 and NAc24 simulation systems. Following position-restrained minimization and equilibration of the system, each system was simulated for 1 microsecond. During the production run, we used torsional angle restraints that were derived from our ssNMR chemical shift assignments with the TALOS+ software[73]. The analysis of the water exposure and contact matrix was done with GROMACS tool g_mindist and an in-house script written in R, respectively. A 5 Å cut-off distance was used for both the water exposure and the contact matrix. The water exposure was averaged over the last 50 ns of the MD simulation and was weighted by the number of heavy atoms.

Rheological Tests. Rheological properties of assembled nanostructures were carried out using a stress-controlled AR-2000ex Rheometer (TA instruments). A truncated cone-plate geometry (acrylic truncated diameter, 20 mm; angle, 1°; truncation gap, 34 μm) was used. All measurements were obtained at

25°C using a Peltier cell in the lower plate of the instrument to control the temperature during each test. All samples were tested one day after dissolution at a concentration of 1% (w/v). To monitor the sol-gel transition, frequency sweep experiments were recorded as a function of angular frequency (0.1-1000 Hz) at a fixed strain of 1%. Strain sweeps were performed on samples from 0.01% to a maximum strain of 1000% to determine the limit of the linear viscoelastic region and, therefore, the maximum strain to which the sample can be tested. Each experiment was performed in triplicate. Data were processed using Origin™ 8 software.

Atomic force microscopy analysis. AFM images were captured in tapping mode by a Multimode Nanoscope V (Digital Instrument, Veeco; resonance frequency 300 kHz, nominal tip radius of curvature 10 nm, forces constant 40 N/m)[20]. Briefly, all peptides were dissolved in distilled water the day prior to imaging. Right before the analysis, peptides solutions were diluted to a final concentration of 0.001% (w/v) and deposited on a freshly cleaved mica surface. Samples (2µl each) were kept on the mica for 2 min at RT and subsequently rinsed with distilled water to remove loosely bound peptides. Samples were ready for imaging after 30min of evaporation. 100 different nanofibers of approximately 10 independent fields per sample were characterized[20].

Thioflavin T (ThT) Spectroscopy Assay. The self-assembly of the peptides to β-sheet fibril structures was analyzed by ThT binding assays. Briefly, ThT stock solution was prepared by adding 8 mg of ThT to 10 mL phosphate buffer (10 mM phosphate, 50 mM NaCl, pH 7) and filtered through a 0.2 µm syringe filter. Right before the analysis, 1 mL of ThT stock solution was diluted into 50 mL of phosphate buffer (working solution). Peptides at 1% (w/v) were mixed with ThT working solution (1:0.5 v/v) and stirred for 5 min. ThT binding was recorded with an Infinite M200 PRO plate reader (Tecan) with λ_{ex} = 440 nm (5 nm bandpass) and λ_{em} = 482 nm (10 nm bandpass), over 60 s at 25 °C, with 5 s shaking before each test. Measurements were performed in triplicate, normalized by ThT fluorescence alone, and processed with Origin8 software.

Supplementary information

Figure S1. Mobile peptides in dynamic hydrogels are not part of the assembly.
Overlay of scalar NMR spectra of A) peptide 30 and B) peptide 4 in their free/monomeric
soluble form (in blue) and their hydrogel form (in red). Spectra of soluble monomeric

peptides were acquired with solution NMR and highly diluted peptide solutions, while scalar ssNMR spectra were acquired with INEPT. The spectral comparison demonstrates that mobile peptides in hydrogels do not take part in larger assembly.
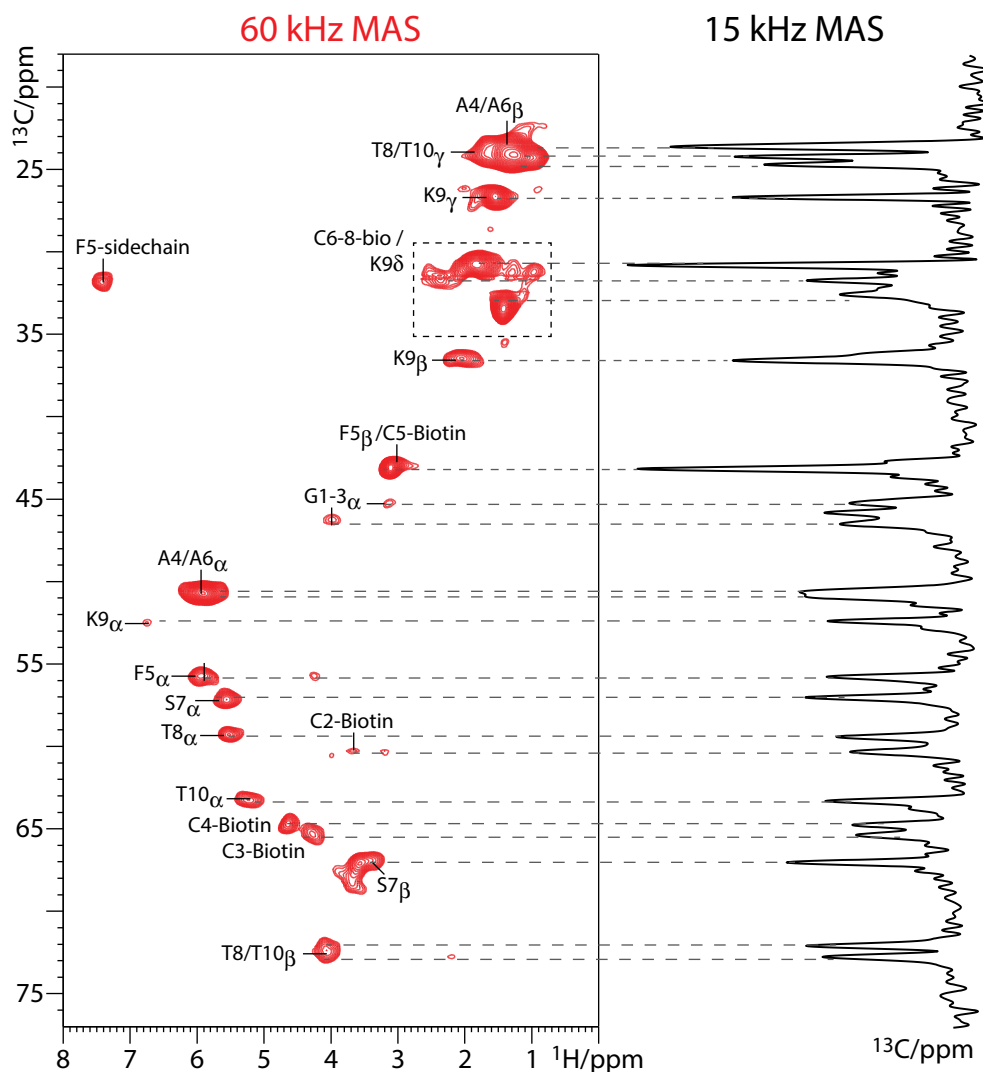
Figure S2. The chemical shifts of hydrogel B24 are the same at 15 and 60 kHz MAS. *(Left)* 2D CH spectrum of scaffold B24 acquired at 60 kHz MAS. *(Right)* ^{13}C CP spectrum of hydrogel B24 hydrogel acquired at 15 kHz MAS. The carbon-signal positions are precisely conserved at 60 kHz MAS. Note that certain signals of CH_2 groups are broadened at 60 kHz due to strongly coupled proton-spins. This is the reason for the low signal intensity of the Cα signals of the glycines.
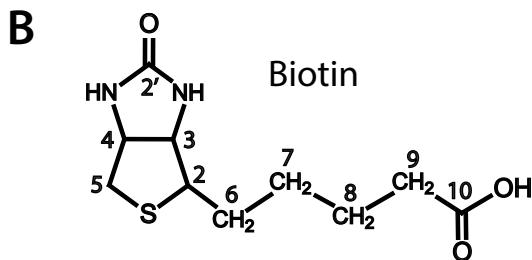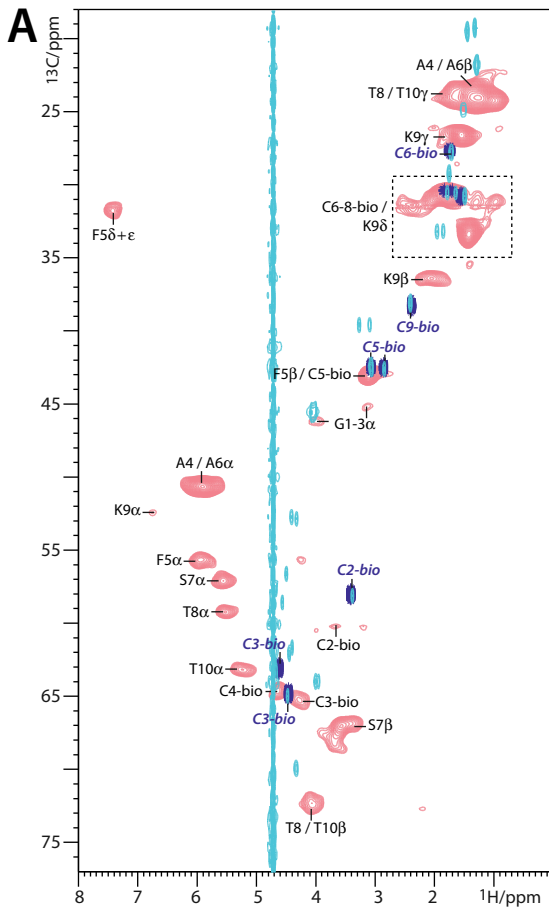
Figure S3. The biotin-tag changes its conformation in the assembled state. A) Overlay of 2D CH spectra of a diluted solution of peptide B24 (in cyan), a solution of biotin (in dark blue), and the fully-assembled hydrogel B24 (in red). Clear chemical shift changes for several biotin carbons can be observed between the diluted and assembled state of the peptide, demonstrating a conformation change of biotin upon forming hydrogel B24. B) Chemical structure of biotin. Nomenclature and biotin-carbon assignments based on Ref. ([36]).
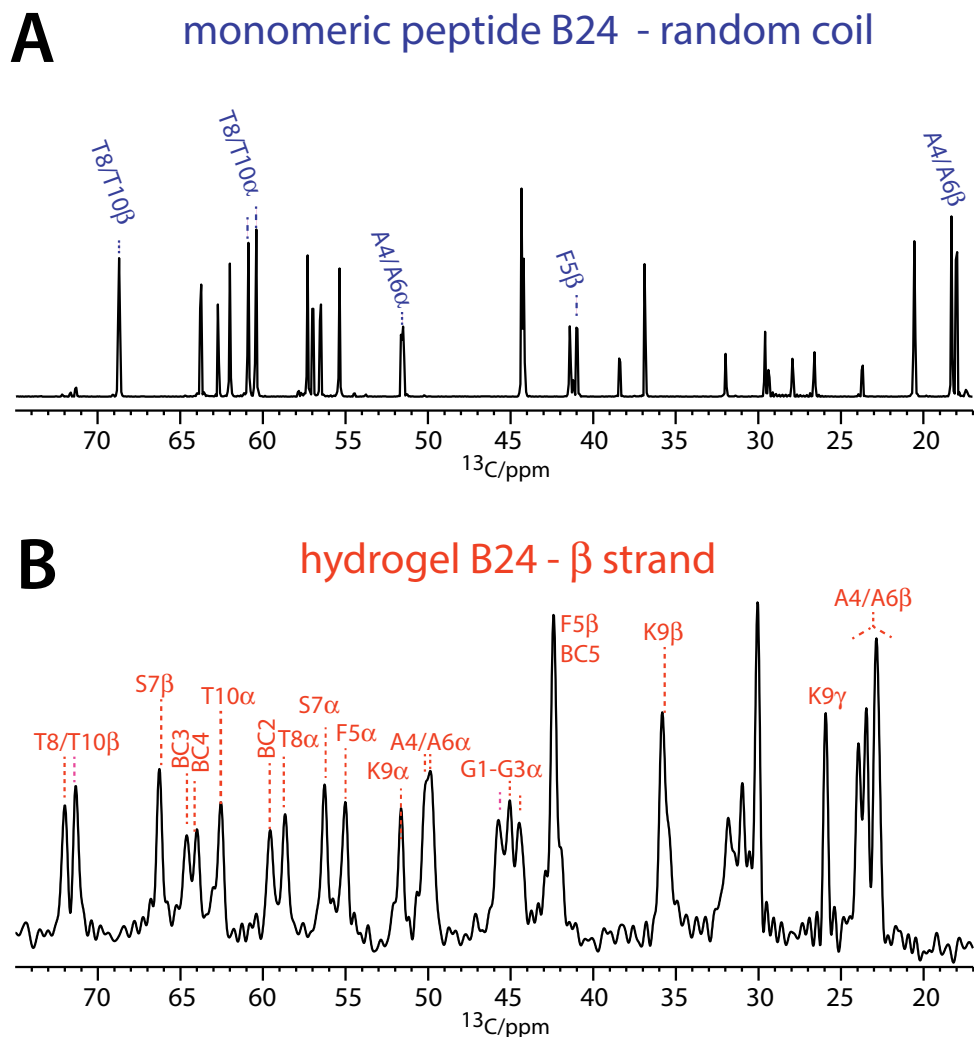
Figure S4. Peptide B24 changes its conformation from random coil to extended upon hydrogel formation. A) Solution NMR spectrum of a monomeric solution of peptide B24. The random coil character of the peptide is readily deducible from chemical shifts of A4/A6 and T8/T10 which are characteristic for unstructured peptides/proteins.[38] B) SSNMR ^{13}C CP spectrum of hydrogel B24. A secondary chemical shifts analysis[38] (see Figure 3B of the main text) clearly demonstrates that the peptide conformation changes towards β-strand conformation in the hydrogel. Biotin-carbon signals are abbreviated as BC.
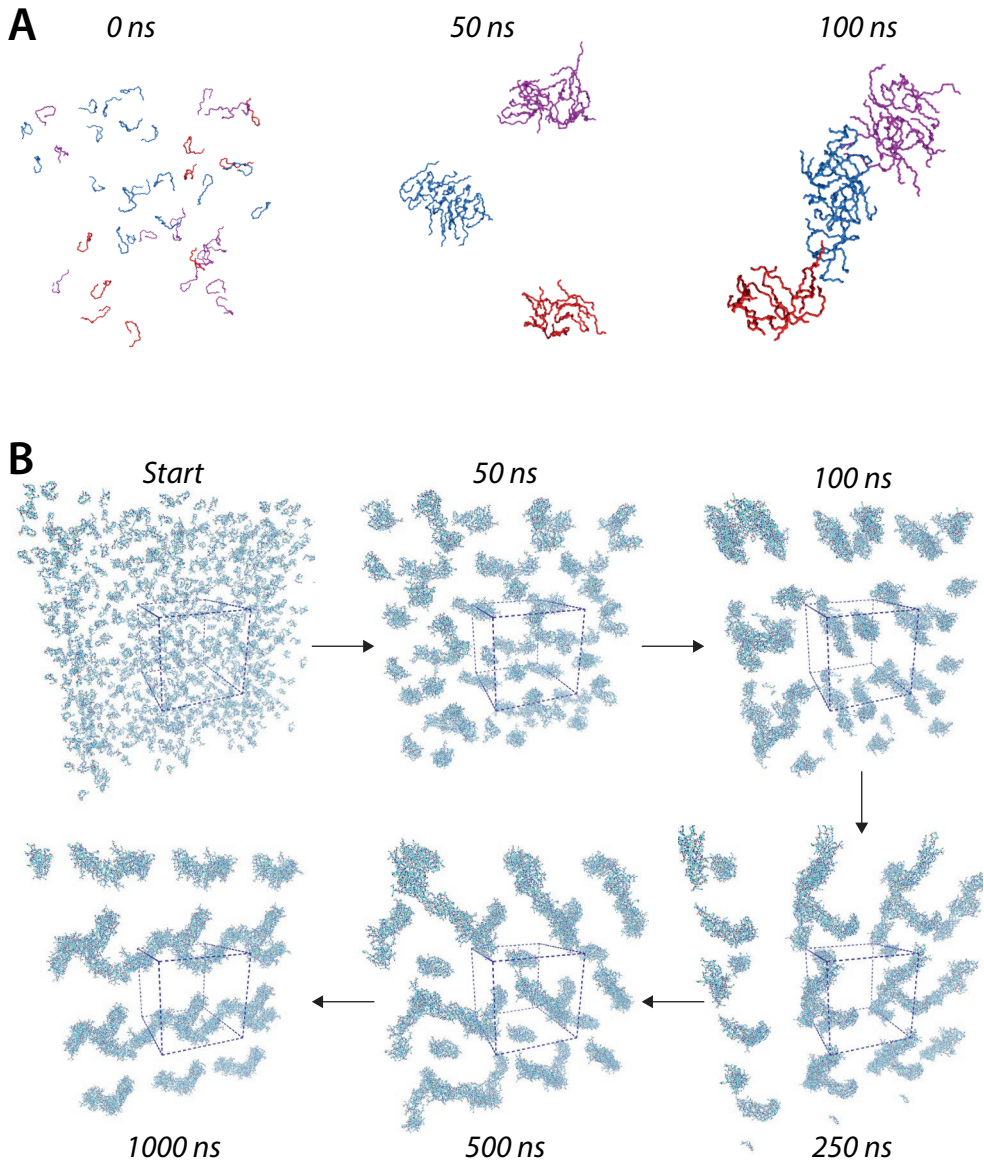
Figure S5. Assembly pathway of peptide B24 in a restrained atomistic MD simulation. All snapshots were obtained from a 1 ms restrained atomistic MD simulation of 100 B24 peptides that were initially randomly placed in a water-filled periodic box. A) Snapshots of B24 peptides, illustrating the preference to assemble into smaller elongated rod-like clusters that then assemble to larger fibers. B) Assembly of B24 peptides. Snapshots taken after 0, 50, 100, 250, 500, and 1000 ns of MD simulation.
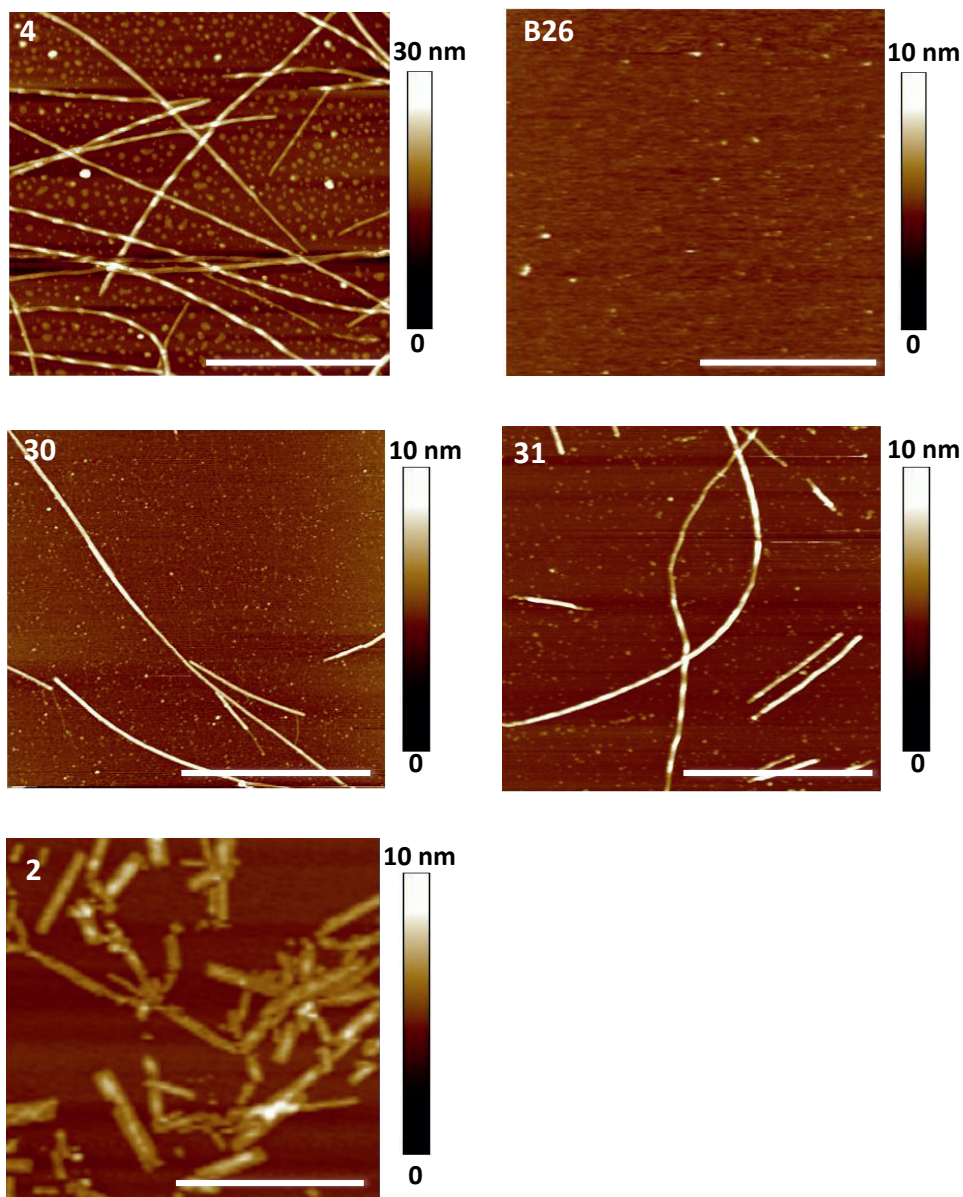
Figure S6. AFM morphological analysis of the mobile hydrogels 2, 4, B26, 30, and 31. Atomic force microscopy images of assembled peptides 2, 4, 30, 31, and the biotinylated B26. Twisted nanofibers are formed by hydrogels 4, 30, and 31, with highest densities for peptide 4. Peptide 2 does not form fibers but relatively sparse nano-dots. B26 does not allow for the assembly of ordered aggregates, leaving room for random dotted aggregates only. Scale bars 1μm.
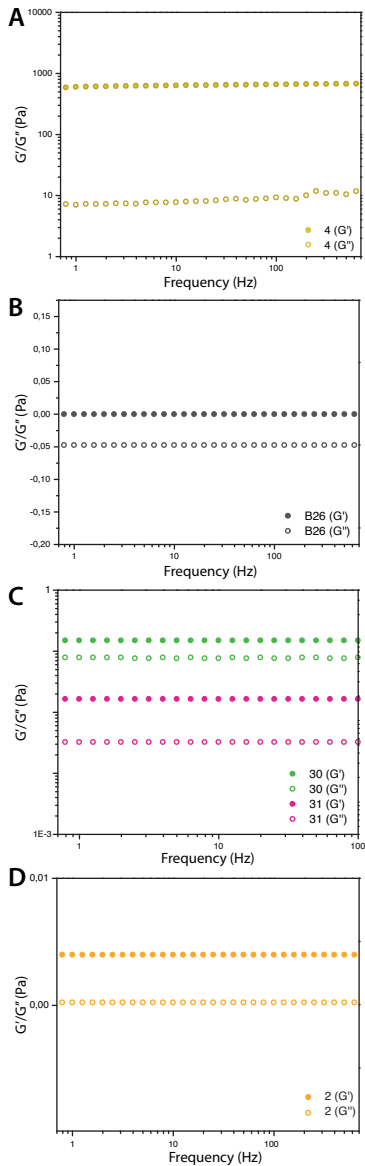
Figure S7. Rheological properties of the mobile hydrogels 2, 4, B26, 30, and 31. Frequency-sweep tests of different self-assembling peptides. A) Peptide 4 displayed typical features of a solid hydrogel (G'~700 Pa), although the G' value is much lower than for hydrogels B3, B15, and B24 (see Figure 6 of the main text). B) The sparse, random aggregates of B26 seen in AFM were mirrored by a G' equal to zero and a by negative G'', both unquestionable indicators of absent scaffold formation. C) Peptides 30 and 31 showed small values of G', highlighting very soft hydrogel formation (G'<1). D) Peptide 2 exhibits an even lower G' value, indicating an even softer hydrogel.

References

1   Scadden, D. T. The stem-cell niche as an entity of action. *Nature* **441**, 1075-1079, doi:10.1038/nature04957 (2006).

2   Vining, K. H. & Mooney, D. J. Mechanical forces direct stem cell behaviour in development and regeneration. *Nat Rev Mol Cell Bio* **18**, 728-742, doi:10.1038/nrm.2017.108 (2017).

3   Smith, L. R., Cho, S. & Discher, D. E. Stem Cell Differentiation is Regulated by Extracellular Matrix Mechanics. *Physiology* **33**, 16-25, doi:10.1152/physiol.00026.2017 (2018).

4   Shin, J. W. & Mooney, D. J. Improving Stem Cell Therapeutics with Mechanobiology. *Cell Stem Cell* **18**, 16-19, doi:10.1016/j.stem.2015.12.007 (2016).

5   Guilak, F. *et al.* Control of Stem Cell Fate by Physical Interactions with the Extracellular Matrix. *Cell Stem Cell* **5**, 17-26, doi:10.1016/j.stem.2009.06.016 (2009).

6   O'Brien, F. J. Biomaterials & scaffolds for tissue engineering. *Mater Today* **14**, 88-95, doi:Doi 10.1016/S1369-7021(11)70058-X (2011).

7   Mao, A. S. & Mooney, D. J. Regenerative medicine: Current therapies and future directions. *Proc Natl Acad Sci U S A* **112**, 14452-14459, doi:10.1073/pnas.1508520112 (2015).

8   Hussey, G. S., Dziki, J. L. & Badylak, S. F. Extracellular matrix-based materials for regenerative medicine. *Nat Rev Mater* **3**, 159-173, doi:10.1038/s41578-018-0023-x (2018).

9   Yang, L. *et al.* A biodegradable hybrid inorganic nanoscaffold for advanced stem cell therapy. *Nat Commun* **9**, 3147, doi:10.1038/s41467-018-05599-2 (2018).

10   Brandl, F., Sommer, F. & Goepferich, A. Rational design of hydrogels for tissue engineering: impact of physical factors on cell behavior. *Biomaterials* **28**, 134-146, doi:10.1016/j.biomaterials.2006.09.017 (2007).

11   Gazit, E. Self-assembled peptide nanostructures: the design of molecular building blocks and their technological utilization. *Chem Soc Rev* **36**, 1263-1269, doi:10.1039/b605536m (2007).

12   Adler-Abramovich, L. & Gazit, E. The physical properties of supramolecular peptide assemblies: from building block association to technological applications. *Chem Soc Rev* **43**, 6881-6893, doi:10.1039/c4cs00164h (2014).

13   Gjorevski, N. *et al.* Designer matrices for intestinal stem cell and organoid culture. *Nature* **539**, 560-564, doi:10.1038/nature20168 (2016).

14   Halperin-Sternfeld, M., Ghosh, M., Sevostianov, R., Grigoriants, I. & Adler-Abramovich, L. Molecular co-assembly as a strategy for synergistic improvement of the mechanical properties of hydrogels. *Chem Commun* **53**, 9586-9589, doi:10.1039/c7cc04187j (2017).

15   Stock, P. *et al.* Unraveling Hydrophobic Interactions at the Molecular Scale Using Force Spectroscopy and Molecular Dynamics Simulations. *Acs Nano* **11**, 2586-2597, doi:10.1021/acsnano.6b06360 (2017).

16   Alberti, K. *et al.* Functional immobilization of signaling proteins enables control of stem cell fate. *Nat Methods* **5**, 645-650, doi:10.1038/nmeth.1222 (2008).

17   Zhu, J. & Marchant, R. E. Design properties of hydrogel tissue-engineering scaffolds. *Expert Rev Med Devices* **8**, 607-626, doi:10.1586/erd.11.27 (2011).

18   Bettinger, C. J., Zhang, Z. T., Gerecht, S., Borenstein, J. T. & Langer, R. Enhancement of in vitro capillary tube formation by substrate nanotopography. *Adv Mater* **20**, 99-+, doi:10.1002/adma.200702487 (2008).

19   Smith, D. J. *et al.* A multiphase transitioning peptide hydrogel for suturing

ultrasmall vessels. *Nature Nanotechnology* **11**, 95-+, doi:10.1038/Nnano.2015.238 (2016).

20   Gelain, F. *et al.* BMHP1-Derived Self-Assembling Peptides: Hierarchically Assembled Structures with Self-Healing Propensity and Potential for Tissue Engineering Applications. *Acs Nano* **5**, 1845-1859, doi:10.1021/nn102663a (2011).

21   Franze, K., Janmey, P. A. & Guck, J. Mechanics in neuronal development and repair. *Annu Rev Biomed Eng* **15**, 227-251, doi:10.1146/annurev-bioeng-071811-150045 (2013).

22   Schlussler, R. *et al.* Mechanical Mapping of Spinal Cord Growth and Repair in Living Zebrafish Larvae by Brillouin Imaging. *Biophys J* **115**, 911-923, doi:10.1016/j.bpj.2018.07.027 (2018).

23   Gelain, F., Horii, A. & Zhang, S. Designer self-assembling peptide scaffolds for 3-d tissue cell cultures and regenerative medicine. *Macromol Biosci* **7**, 544-551, doi:10.1002/mabi.200700033 (2007).

24   Gelain, F., Bottai, D., Vescovi, A. & Zhang, S. Designer self-assembling peptide nanofiber scaffolds for adult mouse neural stem cell 3-dimensional cultures. *PloS one* **1**, e119, doi:10.1371/journal.pone.0000119 (2006).

25   Silva, D. *et al.* Synthesis and characterization of designed BMHP1-derived self-assembling peptides for tissue engineering applications. *Nanoscale* **5**, 704-718, doi:10.1039/c2nr32656f (2013).

26   Wang, Y. & Jardetzky, O. Probability-based protein secondary structure identification using combined NMR chemical-shift data. *Protein Sci* **11**, 852-861, doi:10.1110/ps.3180102 (2002).

27   Chevelkov, V., Rehbein, K., Diehl, A. & Reif, B. Ultrahigh resolution in proton solid-state NMR spectroscopy at high levels of deuteration. *Angew Chem Int Edit* **45**, 3878-3881, doi:10.1002/anie.200600328 (2006).

28   Mroue, K. H. *et al.* Proton-Detected Solid-State NMR Spectroscopy of Bone with Ultrafast Magic Angle Spinning. *Sci Rep-Uk* **5**, doi:ARTN 1199110.1038/srep11991 (2015).

29   Stanek, J. *et al.* NMR Spectroscopic Assignment of Backbone and Side-Chain Protons in Fully Protonated Proteins: Microcrystals, Sedimented Assemblies, and Amyloid Fibrils. *Angew Chem Int Ed Engl* **55**, 15504-15509, doi:10.1002/anie.201607084 (2016).

30   Medeiros-Silva, J. *et al.* (1) H-Detected Solid-State NMR Studies of Water-Inaccessible Proteins In Vitro and In Situ. *Angew Chem Int Ed Engl* **55**, 13606-13610, doi:10.1002/anie.201606594 (2016).

31   Sinnige, T., Daniels, M., Baldus, M. & Weingarth, M. Proton Clouds to Measure Long-Range Contacts between Nonexchangeable Side Chain Protons in Solid-State NMR. *J Am Chem Soc* **136**, 4452-4455, doi:10.1021/ja412870m (2014).

32   Retel, J. S. *et al.* Structure of outer membrane protein G in lipid bilayers. *Nat Commun* **8**, 2073, doi:10.1038/s41467-017-02228-2 (2017).

33   Vasa, S. K., Rovo, P. & Linser, R. Protons as Versatile Reporters in Solid-State NMR Spectroscopy. *Accounts Chem Res* **51**, 1386-1395, doi:10.1021/acs.accounts.8b00055 (2018).

34   Tolchard, J. *et al.* Detection of side-chain proton resonances of fully protonated biosolids in nano-litre volumes by magic angle spinning solid-state NMR. *J Biomol Nmr* **70**, 177-185, doi:10.1007/s10858-018-0168-3 (2018).

35   Mance, D. *et al.* An Efficient Labelling Approach to Harness Backbone and Side-Chain Protons in (1) H-Detected Solid-State NMR Spectroscopy. *Angew Chem Int Ed Engl* **54**, 15799-15803, doi:10.1002/anie.201509170 (2015).

36   Bradbury, J. H. & Johnson, R. N. Assignment of the C-13 Nmr-Spectrum of Biotin.

J Magn Reson **35**, 217-222 (1979).

37   Caprini, A. *et al.* A novel bioactive peptide: assessing its activity over murine neural stem cells and its potential for neural tissue engineering. *New biotechnology* **30**, 552-562 (2013).

38   Wang, Y. J. & Jardetzky, O. Probability-based protein secondary structure identification using combined NMR chemical-shift data. *Protein Sci* **11**, 852-861, doi:10.1110/ps.3180102 (2002).

39   Nagy-Smith, K., Moore, E., Schneider, J. & Tycko, R. Molecular structure of monomorphic peptide fibrils within a kinetically trapped hydrogel network. *P Natl Acad Sci USA* **112**, 9816-9821, doi:10.1073/pnas.1509313112 (2015).

40   Nagy-Smith, K. *et al.* Molecular, Local, and Network-Level Basis for the Enhanced Stiffness of Hydrogel Networks Formed from Coassembled Racemic Peptides: Predictions from Pauling and Corey. *Acs Central Sci* **3**, 586-597, doi:10.1021/acscentsci.7b00115 (2017).

41   Rad-Malekshahi, M. *et al.* The Supramolecular Organization of a Peptide-Based Nanocarrier at High Molecular Detail. *J Am Chem Soc* **137**, 7775-7784, doi:10.1021/jacs.5b02919 (2015).

42   Frederix, P., Patmanidis, I. & Marrink, S. J. Molecular simulations of self-assembling bio-inspired supramolecular systems and their connection to experiments. *Chem Soc Rev* **47**, 3470-3489, doi:10.1039/c8cs00040a (2018).

43   Shen, Y., Delaglio, F., Cornilescu, G. & Bax, A. TALOS+: a hybrid method for predicting protein backbone torsion angles from NMR chemical shifts. *Journal of biomolecular NMR* **44**, 213-223 (2009).

44   Geckil, H., Xu, F., Zhang, X. H., Moon, S. & Demirci, U. Engineering hydrogels as extracellular matrix mimics. *Nanomedicine-Uk* **5**, 469-484, doi:10.2217/Nnm.10.12 (2010).

45   Saracino, G. A., Cigognini, D., Silva, D., Caprini, A. & Gelain, F. Nanomaterials design and tests for neural tissue engineering. *Chem Soc Rev* **42**, 225-262, doi:10.1039/c2cs35065c (2013).

46   Lamour, G. *et al.* Mapping the Broad Structural and Mechanical Properties of Amyloid Fibrils. *Biophys J* **112**, 584-594, doi:10.1016/j.bpj.2016.12.036 (2017).

47   Schiller, J. & Huster, D. New methods to study the composition and structure of the extracellular matrix in natural and bioengineered tissues. *Biomatter* **2**, 115-131, doi:10.4161/biom.20866 (2012).

48   Gelain, F., Lomander, A., Vescovi, A. L. & Zhang, S. G. Systematic studies of a self-assembling peptide nanofiber scaffold with other scaffolds. *J Nanosci Nanotechno* **7**, 424-434, doi:10.1166/jnn.2007.154 (2007).

49   Jelinski, L. W., Sullivan, C. E. & Torchia, D. A. 2H NMR study of molecular motion in collagen fibrils. *Nature* **284**, 531-534 (1980).

50   Huster, D., Schiller, J. & Arnold, K. Comparison of collagen dynamics and isolated fibrils by solid-state in articular cartilage NMR Spectroscopy. *Magnet Reson Med* **48**, 624-632, doi:10.1002/mrm.10272 (2002).

51   Huster, D. Solid-State NMR Studies of Collagen Structure and Dynamics in Isolated Fibrils and in Biological Tissues. *Annu Rep Nmr Spectro* **64**, 127-159, doi:10.1016/S0066-4103(08)00004-5 (2008).

52   Zhu, P. Z. *et al.* Time-Resolved Dehydration-induced Structural Changes in an Intact Bovine Cortical Bone Revealed by Solid-State NMR Spectroscopy. *J Am Chem Soc* **131**, 17064-+, doi:10.1021/ja9081028 (2009).

53   Chow, W. Y. *et al.* NMR Spectroscopy of Native and in Vitro Tissues Implicates PolyADP Ribose in Biomineralization. *Science* **344**, 742-746, doi:10.1126/science.1248167 (2014).

54   Chow, W. Y. *et al.* Essential but sparse collagen hydroxylysyl post-translational modifications detected by DNP NMR. *Chem Commun (Camb)* **54**, 12570-12573, doi:10.1039/c8cc04960b (2018).

55   Goldberga, I., Li, R. & Duer, M. J. Collagen Structure-Function Relationships from Solid-State NMR Spectroscopy. *Accounts Chem Res* **51**, 1621-1629, doi:10.1021/acs.accounts.8b00092 (2018).

56   Mroue, K. H. *et al.* High-Resolution Structural Insights into Bone: A Solid-State NMR Relaxation Study Utilizing Paramagnetic Doping. *J Phys Chem B* **116**, 11656-11661, doi:10.1021/jp307935g (2012).

57   Xu, J. D., Zhu, P. Z., Morris, M. D. & Ramamoorthy, A. Solid-State NMR Spectroscopy Provides Atomic-Level Insights Into the Dehydration of Cartilage. *J Phys Chem B* **115**, 9948-9954, doi:10.1021/jp205663z (2011).

58   Chow, W. Y. *et al.* Proline provides site-specific flexibility for in vivo collagen. *Sci Rep-Uk* **8**, doi:ARTN 1380910.1038/s41598-018-31937-x (2018).

59   Kaplan, M. *et al.* EGFR Dynamics Change during Activation in Native Membranes as Revealed by NMR. *Cell* **167**, 1241-+, doi:10.1016/j.cell.2016.10.038 (2016).

60   Medeiros-Silva, J. *et al.* High-resolution NMR studies of antibiotics in cellular membranes. *Nat Commun* **9**, doi:ARTN 396310.1038/s41467-018-06314-x (2018).

61   Narasimhan, S. *et al.* DNP-Supported Solid-State NMR Spectroscopy of Proteins Inside Mammalian Cells. *Angew Chem Int Edit*, doi:10.1002/anie.201903246 (2019).

62   Roos, M., Wang, T., Shcherbakov, A. A. & Hong, M. Fast Magic-Angle-Spinning (19)F Spin Exchange NMR for Determining Nanometer (19)F-(19)F Distances in Proteins and Pharmaceutical Compounds. *J Phys Chem B* **122**, 2900-2911, doi:10.1021/acs.jpcb.8b00310 (2018).

63   Wang, M. *et al.* Fast Magic-Angle Spinning F-19 NMR Spectroscopy of HIV-1 Capsid Protein Assemblies. *Angew Chem Int Edit* **57**, 16375-16379, doi:10.1002/anie.201809060 (2018).

64   Pines, A., Gibby, M. G. & Waugh, J. S. Proton-Enhanced Nmr of Dilute Spins in Solids. *J Chem Phys* **59**, 569-590, doi:Doi 10.1063/1.1680061 (1973).

65   Schaefer, J. & Stejskal, E. O. C-13 Nuclear Magnetic-Resonance of Polymers Spinning at Magic Angle. *J Am Chem Soc* **98**, 1031-1032, doi:DOI 10.1021/ja00420a036 (1976).

66   Morris, G. A. & Freeman, R. Enhancement of Nuclear Magnetic-Resonance Signals by Polarization Transfer. *J Am Chem Soc* **101**, 760-762, doi:DOI 10.1021/ja00497a058 (1979).

67   Fung, B. M., Khitrin, A. K. & Ermolaev, K. An improved broadband decoupling sequence for liquid crystals and solids. *J Magn Reson* **142**, 97-101, doi:DOI 10.1006/jmre.1999.1896 (2000).

68   Weingarth, M., Bodenhausen, G. & Tekely, P. Low-power decoupling at high spinning frequencies in high static fields. *J Magn Reson* **199**, 238-241, doi:10.1016/j.jmr.2009.04.015 (2009).

69   Zhou, D. H. & Rienstra, C. M. High-performance solvent suppression for proton detected solid-state NMR. *J Magn Reson* **192**, 167-172, doi:10.1016/j.jmr.2008.01.012 (2008).

70   Mazzini, L. *et al.* Human neural stem cell transplantation in ALS: initial results from a phase I trial. *Journal of translational medicine* **13**, 17, doi:10.1186/s12967-014-0371-2 (2015).

71   Hess, B. GROMACS 4: Algorithms for highly efficient, load-balanced, and scalable molecular simulation. *Abstr Pap Am Chem S* **237** (2009).

4

72   Oostenbrink, C., Villa, A., Mark, A. E. & Van Gunsteren, W. F. A biomolecular
        force field based on the free enthalpy of hydration and solvation: The GROMOS
        force-field parameter sets 53A5 and 53A6. *J Comput Chem* **25**, 1656-1676,
        doi:10.1002/jcc.20090 (2004).

73   Shen, Y., Delaglio, F., Cornilescu, G. & Bax, A. TALOS plus : a hybrid method for
        predicting protein backbone torsion angles from NMR chemical shifts. *J Biomol
        Nmr* **44**, 213-223, doi:10.1007/s10858-009-9333-z (2009).

CHAPTER 5

Shifts in the selectivity filter dynamics cause modal gating in K$^+$ channels

Abstract

   Spontaneous activity shifts at constant experimental conditions represent a widespread regulatory mechanism in ion channels. The molecular origins of these modal gating shifts are poorly understood. In the K^+ channel KcsA, a multitude of fast activity shifts that emulate the native modal gating behaviour can be triggered by point-mutations in the hydrogen bonding network that controls the selectivity filter. Using solid-state NMR and long molecular dynamics simulations in a variety of KcsA mutants, here we show that modal gating shifts in K^+ channels are caused by large shifts in the channel dynamics that strongly perturb the selectivity filter equilibrium conformation. Furthermore, we reveal a drastically different motional and conformational selectivity filter landscape in a mutant that mimics voltage-gated K^+ channels, which provides a foundation for an improved understanding of eukaryotic K^+ channels. Altogether, our results provide a high-resolution perspective on some of the complex functional behaviour of K^+ channels.

Introduction

Potassium (K⁺) channels are of fundamental importance for the functioning of excitable cells[1]. They allow selective and rapid flux of K⁺ across the cell membrane through a central pore, which is regulated by the interplay between a cytoplasmic activation gate and an extracellular C-type inactivation gate known as selectivity filter. The selectivity filter sequence TVGYG is highly conserved, and its backbone carbonyl-groups together with the threonine hydroxyl group line up to form the five K⁺ coordination sites (S0-S4)[2,3].

Extensive crystallographic studies in the well-accepted model K⁺ channel KcsA showed that C-type inactivation is governed by a complex hydrogen bond network behind the selectivity filter[4,5]. Residue E71 is at the centre of this network, and modulates the selectivity filter by coordinating to the backbone of Y78 and, mediated via a water molecule, the D80 as well as the W67 side chains (Figure 1A). While W67 and D80 are highly conserved in K⁺ channels, E71 is commonly replaced by a valine or isoleucine in eukaryotes (Figure 1B), which is assumed to critically modulate selectivity filter gating. Indeed, electrophysiological measurements showed that point-mutations at E71 lock the KcsA channel into different, natively occurring gating modes, which are best represented by a high-open probability (E71A), a low-open probability (E71I), and a high-frequency flicker (E71Q) mode[6]. Random shifts between such gating modes, known as "modal gating shifts", were observed in various eukaryotic and prokaryotic K⁺ channels, and are a widespread regulatory mechanism of channel activity[4,7-11]. Yet, despite their broad functional importance, the structural correlates and triggers of modal gating shifts are unknown. Modal gating shifts were suggested to relate to selectivity filter rearrangements, however, a series of X-ray structures of E71X mutants showed no changes in the filter (RMSD relative to WT KcsA is <0.25 Å)[6] despite the marked functional heterogeneity of these mutants. Curiously, for the E71A mutant, a well-established model to study K⁺ channel gating[12,13], a second, strongly different filter conformation of uncertain functional relevance was crystallised[4,14]. Besides the lack of clarity on the selectivity filter conformation, it was further assumed that changes in the filter dynamics could cause modal gating shifts[6]. However, also here, whether the selectivity filter dynamics change in reference to the gating mode is unknown, and experimental data are scarce to resolve this question. Altogether, there is a fundamental lack of knowledge how the hydrogen bond network surrounding the selectivity filter modulates its gating, which critically limits our understanding of modal gating shifts and of Kv channels.

Here, we use modern proton-detected (¹H-detected)[15-20] solid-state NMR (ssNMR) in native-like membranes to compare the selectivity filter in WT KcsA and the three mutants (E71A, E71I, E71Q) that are best representatives

of modal gating. We show that E71 point-mutations cause marked changes in the selectivity filter conformational dynamics, in contrast to previous crystallographic studies that revealed virtually no changes in structure[6]. By combining ssNMR with long MD simulations, we demonstrate that altered structural dynamics in E71X mutants drive the selectivity filter into new conformational equilibria that represent the molecular origin of modal gating. Furthermore, we show that modal gating goes hand in hand with fluctuations in the hydrogen bonding and water network behind the filter, which are triggers of sudden mode shifts. Altogether, these results provide a high-resolution perspective on the complex kinetic behaviour of the selectivity filter of K^{+} channels. Importantly, the pronounced conformational and motional changes that we observe in E71I KcsA provide a foundation for future elucidation of the selectivity filter of eukaryotic K^{+} channels.

Results

NMR assignments of the channels at near-native conditions

We assigned the ^{1}H, ^{13}C, and ^{15}N ssNMR chemical shifts of WT KcsA and the E71A, E71I, E71Q mutants in order to analyse their conformational dynamics in membranes. First, we prepared uniformly [^{13}C,^{15}N]-labelled inversely Fractionally Deuterated[17] channels in liposomes composed of *E.coli* lipids. Samples were prepared in buffer conditions (pH 7.4, 100 mM K^{+}) at which WT KcsA is in the closed-conductive state,[21] i.e., a state with a closed activation gate and a conductive selectivity filter. *De-novo* backbone chemical shift assignments were obtained for mutant E71A using a set of four dipolar-based three-dimensional (3D) ^{1}H-detected ssNMR experiments (CαNH, CONH, Cα(CO)NH, CO(Cα)NH) (Figure 1C and Figure S1). The high spectral quality enabled us to almost fully assign residues L41-W87, which include the complete selectivity filter and pore helix, the pore loop, larger part of the outer transmembrane 1 (TM1) helix, and a few residues of the inner transmembrane 2 (TM2) helix. Since we used dipolar-based magnetization transfer steps that decrease in efficiency with increasing molecular mobility, the cytoplasmic domain (F125-R160) and the membrane-associated M0 helix (M1-H20) were not detectable at our experimental temperatures of 300-310 K[22]. Assignments were then transferred to KcsA mutants E71I and E71Q and confirmed with a reduced set of 3D ssNMR experiments (CαNH, CONH). The reduced set was also used to complement our previous WT KcsA assignments[17]. For the flicker mutant E71Q, spectral sensitivity was significantly lower, indicative of increased mobility, which averages dipolar magnetization transfer efficiency. Furthermore, for all mutants and WT KcsA, we acquired two-dimensional (2D) [13]C-^{13}C experiments. Moreover, we acquired dipolar 2D ^{15}N-^{1}H ssNMR spectra, in which each signal relates to one [15]N-^{1}H backbone or side chain unit, and which represent 'spectral

fingerprints'.

Modal gating relates to changes in the filter conformation

NMR chemical shifts are sensitive reporters of protein conformation. Therefore, comparing the chemical shifts of the mutants to WT KcsA enables the analysis of the structural impact of the substitutions at E71. The 2D ^{15}N-^{1}H and ^{13}C-^{13}C spectra of all E71X mutants superimposed very well onto WT KcsA, demonstrating that the global WT KcsA fold is conserved (Figure S2). However, for all mutants, we observed strikingly large ^{1}H and ^{15}N (HN) as well as ^{13}C chemical shift perturbations (CSPs) across the selectivity filter (Figure 1D, E and Figure S3). For all mutants, we observed very important HN CSPs for the essential residues W67, Y78, and D80 behind the filter, demonstrating changes in their hydrogen bond interactions. At the same time, the large ^{13}Cα and CO CSPs that we observed for residues G77, Y78, and D80 imply pronounced conformational filter backbone changes, which likely have implications for the K+ occupancy. Intriguingly, all mutants also exhibited a large CSP for V76CO which is immediately involved in K+ binding and key residue for C-type inactivation (Figure 1E)[3].
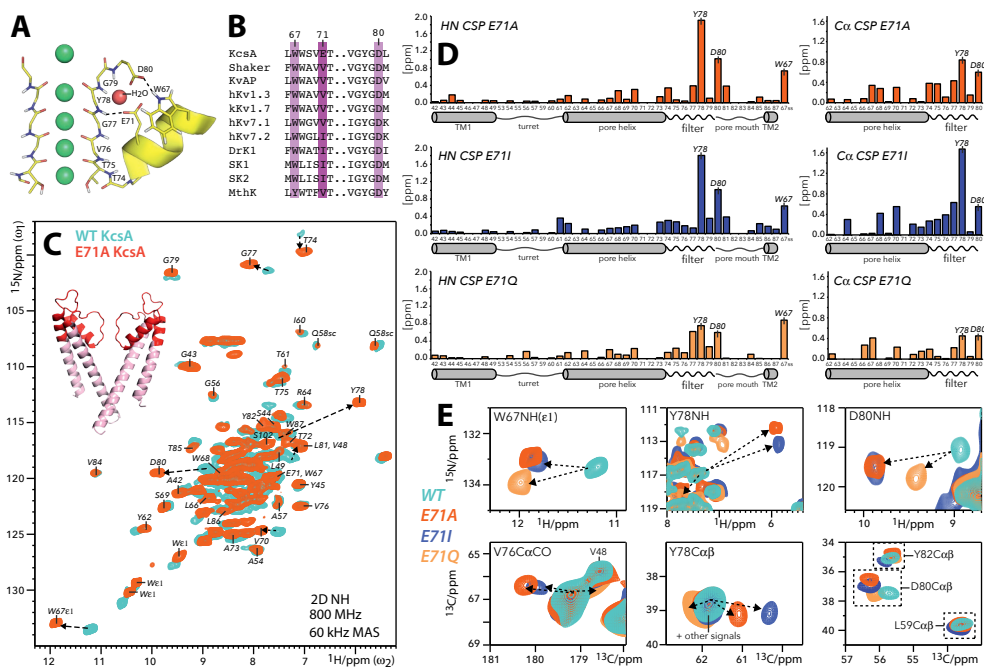
**Figure 1. E71X point-mutations cause large conformational changes in the KcsA selectivity filter.** A) The selectivity filter of K+ channel KcsA (1K4C) is regulated by a hydrogen bond network with the triad W67-E71-D80 at the center.[5] B) W67 and D80 are highly conserved, while E71 is commonly replaced by a nonpolar valine or isoleucine in Kv channels. C) 2D NH ssNMR spectra of WT KcsA (cyan) and mutant

E71A (red) acquired in membranes. Arrows indicate major signal shifts of key residues. Residues L41-W87 are annotated in the E71A spectrum and highlighted in red on the X-ray structure. D) Chemical shift perturbations (CSPs) of E71A (red), E71I (blue), and E71Q (orange) in reference to WT KcsA. (left) Combined HN CSPs of amino-protons and backbone-nitrogens and (right) Cα CSPs. The strongest NH CSPs in E71A are highlighted in Figure C. Source data are provided as a Source Data file. E) 2D NH (upper panel) and 2D CC spectra (lower) showing large CSPs of key residues W67, V76, Y78, and D80 in E71A (red), E71I (blue), and E71Q (orange) relative to WT KcsA (cyan).

Mutants E71A and E71I showed a strikingly similar CSP pattern. Here, the HN and ^{13}C signal shifts of W67, V76, Y78, and D80 are all similar in magnitude and in the same direction. This similarity appears plausible, given that neither alanine nor isoleucine is able to mimic the hydrogen bonding capacities of the E71 carboxyl group. However, although the CSP pattern is similar, E71I shows a much larger Y78Cα CSP than E71A, which implies conformational differences.

While we also observed CSP maxima at W67, G77, Y78, and D80 in E71Q, these signal shifts were partially in opposite direction relative to E71A and E71I, and less strong. In general, among the three mutants, the chemical shifts of E71Q deviated the least from WT KcsA. Considering that a glutamine can partly substitute for some of the hydrogen bonds of a glutamate, it is likely that the E71Q filter conformation is relatively close to WT KcsA. Indeed, the D80 side chain and the Y78 backbone showed by far the smallest CSPs for E71Q, which strongly suggests that Q71 - D80 and Q71 – Y78 maintain interactions analogous to WT KcsA, while these interactions are lost in E71A and E71I (Figures 2A and 1E).
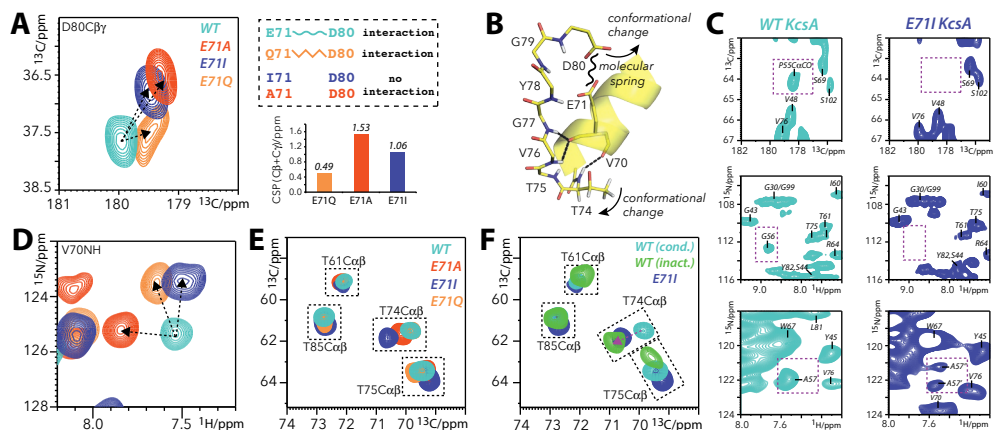
Figure 2. Loss of the E71-D80 interaction causes extended rearrangements behind the filter. A) (left) Zoom into 2D CC ssNMR spectra of WT KcsA (cyan), E71A (red), E71I (blue), and E71Q (orange) showing the D80 side chain CSP. (right) E71Q mimics the E71 – D80 interaction, which is lost in E71A and E71I. The D80 side chain CSPs are large in E71A and E71I, while they are small in E71Q. B) Structural representation (1K4C)

of the stabilisation of filter residues T74-G77 by hydrogen bonds with V70 and E71 of the pore helix. C) The E71I turret is disordered, which causes signals to disappear or split. Spectral zooms are show for WT KcsA (cyan) and E71I (blue). D) Overlay of 2D NH spectra showing a strong CSP for V70 of the pore helix. E) Overlay of 2D CC spectra, showing CSPs of the functionally critical T74 side chain in E71X mutants. F) The large T74 CSP in E71I (pH 7.4, 100 mM K⁺) is reminiscent of the inactivated filter in WT KcsA (pH 4, 0 mM K⁺).

Next to conformational changes in the filter, the mutants showed moderate to larger CSPs around residues W67-V70. These changes presumably relate to modulations in the aromatic belt W67, W68, and Y78 that surrounds the filter, and to the loss or modulation of interaction E71 – D80, which acts as a molecular spring that couples the pore helix to the pore mouth in WT KcsA (Figure 2B)[5]. Our data show that the pore helices in all mutant channels exhibit, compared to WT KcsA, local changes (Figure 2D) that modulate the residues T74-T75-V76-G77 at the N-terminal end of the selectivity filter, which are directly coordinated to the pore helix by hydrogen bonds. Indeed, all mutants show clear perturbations at V76 and G77 (Figure 1D, E). We observed the largest CSP in the E71I pore helix, which correlates with strong signal shifts of the T74 side chain. Since conformational changes of the T74 side chain relate to C-type inactivation[23,24], this perturbation could be functionally important for E71I, which favours transitions to a non-conductive state[6]. This assumption is corroborated by 2D CC spectra, which show that the T74 side chain conformation in E71I (pH 7.4, 100 mM K⁺) and in the inactivated filter of WT KcsA (pH 4, 0 mM K⁺) are close to each other (Figure 2E, F).

Furthermore, we observed remarkable conformational changes in the turret G53-T61. The turret is an important drug binding site[25] and responds to gating changes[26], however, the structural underpinning is unclear and inaccessible from X-ray structures because of intense interactions between turret and Fab fragments[4]. In our ssNMR experiments, the CSPs in the turret are small. However, to our surprise, residues P55, G56, and A57 in E71I disappeared or showed signal splitting, strongly indicative of stark structural heterogeneity (Figure 2C). This implies that the replacement of E71 by isoleucine causes long-range effect that are felt ~2 nm away from the mutation site. Note that CSPs for the TM1 and TM2 helices, as well as for un-annotated TM residues, were very small, confirming that the global WT KcsA fold is conserved in the mutants.

5

Changes in the filter dynamics and modal gating shifts

Historically, the selectivity filter was thought to form a stiff framework in order to allow fast conduction of K$^+$ together with high selectivity over Na^{+2}. More recent studies point to a more dynamic filter[27], and hypothesize that modal gating shifts relate to shifts in the motional behaviour of the filter[6]. However, quantitative experimental data on selectivity filter dynamics are not available in membranes, critically limiting our understanding of K$^+$ channel function. Here we probe the filter dynamics in reference to the gating mode with ssNMR relaxation, which is an ideal approach to measure the internal dynamics of membrane proteins at native conditions[17,28]. Site-resolved ssNMR relaxation can be probed with 2D ^{15}N-^{1}H experiments that include a relaxation element that is sensitive to dynamics on a certain time-scale. A series of spectra is then acquired with increasing duration of the relaxation element, and the signal sensitivity decreases according to the motion for a given residue. The signal decay is then converted into a relaxation rate R, and higher rates indicate enhanced dynamics. We probed the ^{15}N slow rotating-frame relaxation (R$_{1rho}$) for WT KcsA and the mutants (Figure 3) using extensive series of ^{1}H-detected 2D ^{15}N-^{1}H experiments[29]. ^{15}N R$_{1rho}$ relaxation is sensitive to dynamics in the nanosecond-millisecond range but dominated by motion with slow correlation times in the microsecond range[30]. The high sensitivity with ^{1}H-detection enabled us to measure relaxation rates with high accuracy. In all investigated channels, our study unravelled strikingly different filter dynamics that clearly correlate with the CSP maxima, thereby linking conformational and motional changes. In WT KcsA, the filter (~15 ms^{-1} R$_{1rho}$) is the most dynamic membrane-embedded region, with G79 as a distinct local maximum. The dynamics of the pore helix is slightly lower, TM1 residues show the least dynamics, while the extracellular turret is by far the most mobile region. These results agree with our previous relaxation studies in WT KcsA[17].

The global dynamics of mutant E71I, which mimics certain Kv channels, resembles WT KcsA. Surprisingly, compared to WT KcsA, we measured strongly enhanced dynamics at the filter entrance Y78-D80 (~25 ms^{-1} R$_{1rho}$). These residues also showed the largest CSPs, demonstrating again that local conformational and motional changes correlate. Furthermore, we observed sizeable stiffening at G77 in the middle of the E71I filter. Intriguingly, the selectivity filter dynamics is very different in the E71A mutant, in which the middle and upper filter regions (V76-D80) drastically rigidified (~8 ms^{-1} R$_{1rho}$). This means that both E71A and E71I exhibit clearly different filter dynamics in spite of similar CSP patterns. It is easy to imagine that these differential dynamics are at the origin of some of the heterogeneous gating kinetics observed in KcsA and other K$^+$ channels. As for the CSPs, the flicker mutant E71Q behaved very differently and featured substantially and globally enhanced R$_{1rho}$ values with a

maximum at V76. This means that the entire channel undergoes pronounced large-scale slow motions, which explains the strongly reduced sensitivity in our dipolar experiments with E71Q. Altogether, our data hence strongly suggest that the rapid flickering between open and closed states in KcsA, and observed in all K+ channels[6,10], relates to large-scale dynamics of the pore domain.

Another noteworthy observation was the stark change in the dynamics of the turret, which rigidified in E71A and E71I. As we concluded above (Figure 2C), this implies that the loss of the E71 – D80 interaction causes allosteric changes 2 nm distal from the mutation site, presumably by successive changes of hydrogen bonding partners. A likely starting point for this chain reaction could be D80, which adopts a clearly different conformation in E71A and E71I compared to WT KcsA (Figure 2A).

5
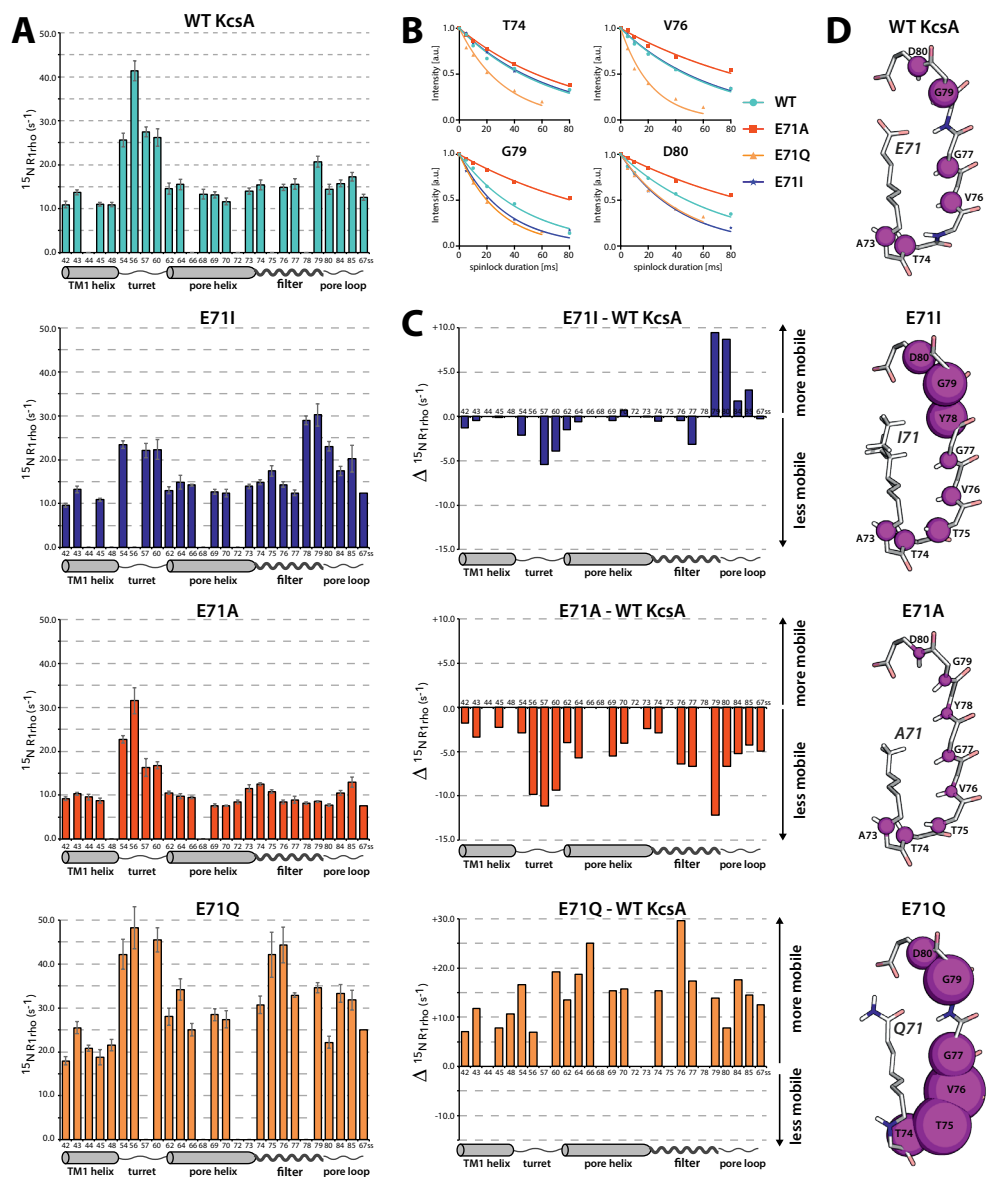
Figure 3 E71X point-mutations strongly change the selectivity filter dynamics. A) ^{15}N rotating-frame ssNMR relaxation rates (R_{1rho}) that report on slow molecular motions in WT KcsA (cyan), E71A (red), E71I (blue), and E71Q (orange) measured at 700 MHz and 58 kHz MAS. The error bars show the standard error of the fit. Source data are provided as a Source Data file. B). R_{1rho} signal decay curves for selected filter residues. Symbols mark data points and lines represent best fits. C) Plots of the differences in the dynamics between E71X mutants and WT KcsA. D) Illustration of the site-resolved selectivity filter dynamics. The size of the magenta spheres represents the R_{1rho} relaxation rates.

Fluctuations in a critical water cavity trigger modal gating

The strongly different filter dynamics in the E71X mutants raise the question which molecular events could cause spontaneous mode shifts. One potential trigger could be buried water, localised in a cavity behind the filter, which is an decisive gating determinant in K⁺ channels, relating to C-type inactivation and recovery[22,31,32]. Previous X-ray studies suggested that changes in size of the water cavity could trigger modal gating shifts. In these and other previous studies, two water molecules were resolved behind the filter of E71I and E71A[6,12], while the presence of buried water molecules in E71Q was unclear due to insufficient resolution.

Here, we revisit the water distribution behind the selectivity filter using H/D exchange ssNMR[17,33,34], for which we acquired 2D ¹⁵N-¹H spectra in fully deuterated buffers. At these conditions, exchange with deuterons strongly attenuates signals of water-exposed amino-protons, which provides high-resolution information on the water cavity size.[22] The channels were incubated in deuterated buffers for two days, and the completeness of the exchange was confirmed on the fully water-exposed turret, which entirely disappeared from the 2D NH spectra (Figure 4A, right panel). In WT KcsA, G79 is the only filter residue that disappeared in deuterated buffers while Y78-T74 showed no signs of H/D exchange (Figure 4A, B). The lack of exchange for Y78 in WT KcsA is astonishing, given that a water molecule is in direct proximity in the X-ray structure (Figure 1A), and strongly suggests that a tight hydrogen bond with E71 protects Y78 from H/D exchange. In line with this conclusion, Y78 showed attenuated intensity in both E71I (-33 %) and E71A (-81 %) (Figure 4B, C), in which the X71 – Y78 hydrogen bond is lost. Intriguingly, the much faster exchange of Y78 in E71A implies a larger water cavity, which agrees with the smaller size of alanine relative to isoleucine. The widened water cavity is also corroborated by the high rigidity of E71A (Figure 3), which renders enhanced molecular fluctuations an unlikely cause for increased H/D exchange. Strikingly, in the flickery E71Q channel, G79 did not exchange (Figure 4A). Similarly, L81 did not exchange in E71Q, while it disappeared in E71A, E71I, and WT KcsA, which confirms that the water cavity is smaller or fully absent behind the E71Q filter. Altogether, our NMR data demonstrate that, in membranes, E71X point-mutations changes the size of the water cavity in reference to the gating mode, analogous to the crucial change of the water cavity during C-type inactivation[31]. Note that long MD simulations, which are discussed in detail in the following sections, also show widened water cavities and higher exchange-rates with bulk water for E71A and E71I (Figure S4).
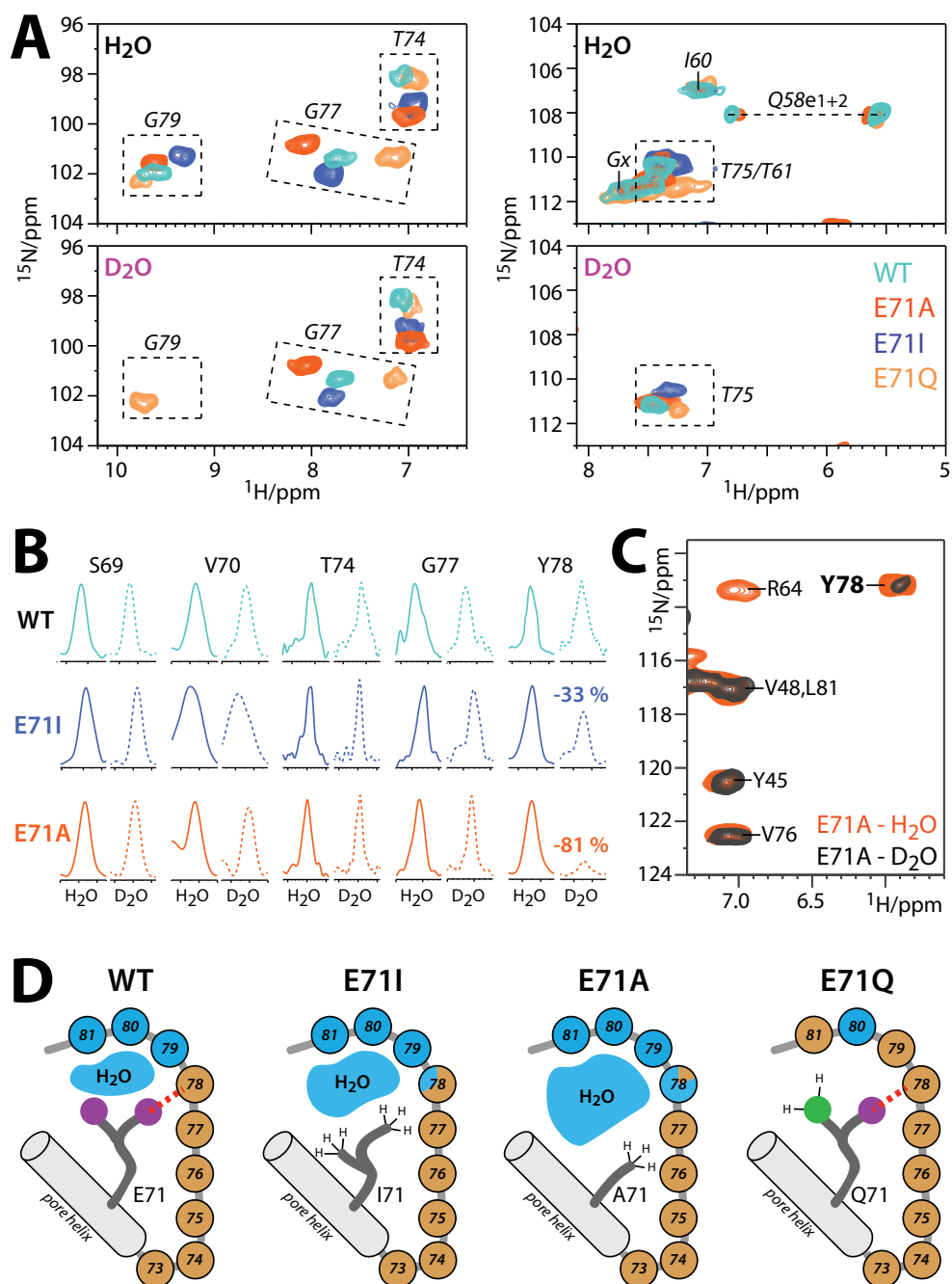
Figure 4 High-resolution analysis of the size of the water cavity behind the filter.
A) Zoom into 2D NH ssNMR spectra acquired in (upper panel) protonated and (lower) deuterated buffers of WT KcsA (cyan), E71I (blue), E71A (red), and E71Q (orange). B) Cross-sections from 2D NH spectra of WT KcsA, E71I, and E71A measured in protonated (continuous lines) and deuterated (dashed) buffers. For Y78 in WT KcsA, cross-sections

were extracted from 3D CANH experiments to resolve spectral overlap. Signals are normalised (see Methods). C) 2D NH spectra of E71A in protonated (red) and deuterated (grey) buffers showing the fast exchange of Y78, implying a larger water cavity. D) Illustrations of the ssNMR-derived water cavity size: in WT KcsA, the cavity is limited to G79-L81, and Y78 is exchange-protected. The cavity widens in E71I, strongly widens in E71A, and is absent in E71Q. Blue and brown spheres represent water-exposed and shielded amino-protons, respectively.

Shifts in the equilibrium structure of the filter

Our ssNMR data demonstrate that E71 point-mutations cause large CSPs in the selectivity filter, with maxima at Y78Cα and V76CO; the latter forming the S2 and S3 sites that are critically involved in C-type inactivation[3]. Such large perturbations in the heart of the filter are astonishing, given that E71A and E71I show a sharply reduced extent of C-type inactivation[6]. To gain a structural understanding of the ssNMR CSPs, we performed a series of 1 μs-long MD simulations for each WT KcsA and the mutants (Figure 5A and Figure S5). For WT KcsA, simulations show that the selectivity filter samples two conformations in which V76CO points either towards (inwards conformation) or away (outwards) from the filter pore[35]. The equilibrium between these two, most likely rapidly converting, conformations was recently confirmed by 2D IR data that showed a 60:40 ratio between inwards:outwards conformations. Remarkably, simulations also indicate that E71X mutations perturb this equilibrium, stabilising the V76CO inwards conformation in E71I and E71A, while the outwards state is favoured in E71Q.

To probe if the V76CO CSPs could be explained by a change in the average conformation of the filter, we back-calculated[36] the ^{13}C ssNMR chemical shifts over the MD simulations (Figures 5B, C). These calculations yielded a much lower V76CO chemical shift in the outwards conformation (predicted $\Delta V76CO_{inwards-outwards}$ = +2 to +3 ppm) (Figure 5D); a result that agrees with the much lower chemical shift of V76CO at low [K+] in the collapsed filter with a flipped V76-G77 plane (experimental $\Delta V76CO_{conductive\ filter\ -\ collapsed\ filter}$ = +3.3 ppm)[21,37]. Hence, these results show that the V76CO inwards conformation is strongly stabilised in E71A (V76CO CSP = +0.94 ppm relative to WT KcsA) and E71I (+0.77 ppm), while the sampling of the outwards conformation is enhanced in E71Q (-0.55 ppm) (Figure 5E). This conclusion also agrees with our relaxation data, which show reduced dynamics for V76 and G77 in E71A and E71I, whereas both residues show much higher mobility in E71Q. Notably, the stabilisation of the V76CO inwards state correlates with the decrease of C-type inactivation in E71A and E71I[6].
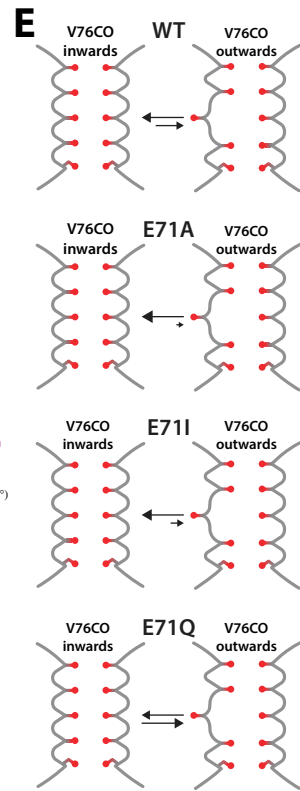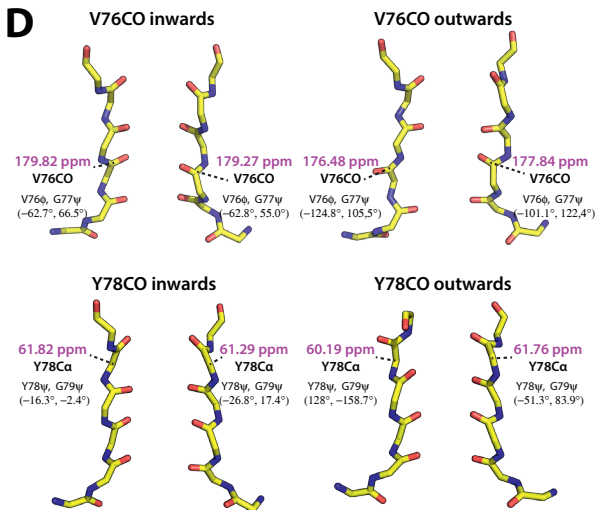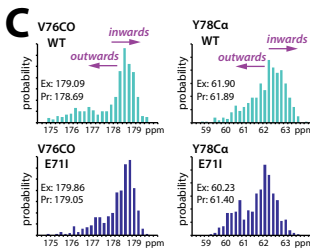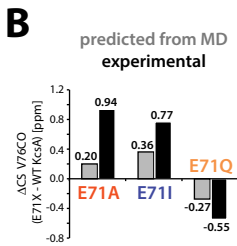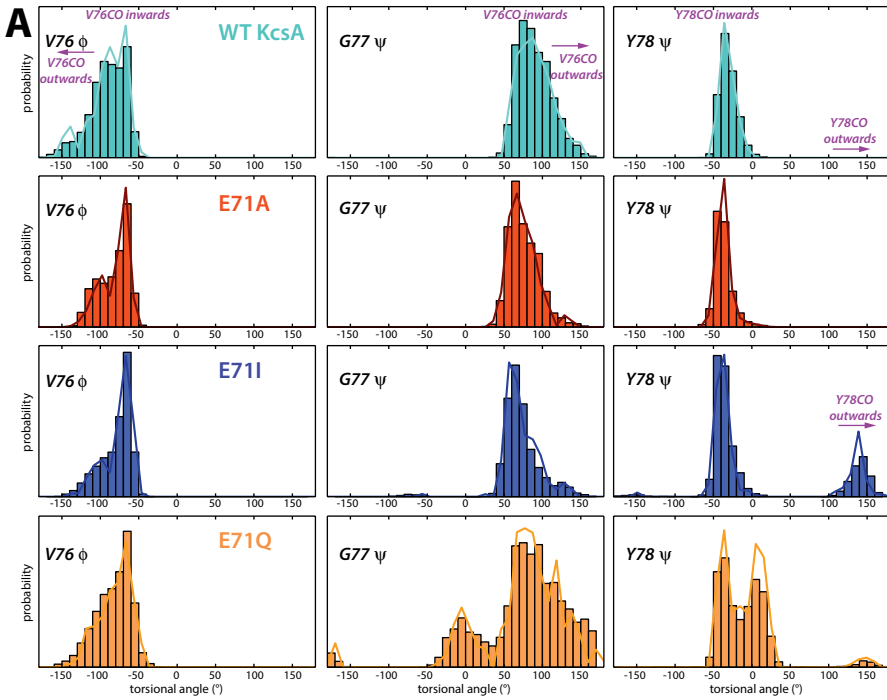
Figure 5. E71X mutations shift the equilibrium between inwards and outwards filter states. A) Dihedral angle distribution of filter residues of WT (cyan), E71A (red), E71I (blue), and E71Q (orange) derived from 1-µs-long MD simulations. Characteristic angular spaces for inwards conformations, with the carbonyl group oriented towards the filter pore, and outwards states are highlighted. B) Comparison of V76CO CSPs derived from experiments (black bars) and back-calculated[36] from MD simulations (grey bars). Source data are provided as a Source Data file. C) Histogram of back-calculated chemical shifts for V76CO and Y78Cα of WT KcsA (cyan) and E71I (blue). The V76CO (left) inwards state is stabilised in E71I, leading to higher V76CO chemical shifts, while the Y78CO (right) inwards state is destabilised in E71I, leading to lower Y78Cα chemical shifts. D) Representative MD snapshots of WT KcsA and E71I showing inwards and outwards states of V76CO and Y78CO. The chemical shifts (in magenta) of V76CO and Y78Cα strongly differ between inwards and outwards conformations. E) Illustration of the stabilisation of the V76CO inwards state in E71A and E71I, and the destabilisation in E71Q.

Similarly, we could derive a structural understanding of the stark Y78Cα CSPs. In MD simulations, WT KcsA exclusively adopts the Y78CO inwards conformation that is stabilised by the E71 – Y78 hydrogen bond. However, in E71I, the Y78 backbone is no longer stabilised and we observe sizeable sampling of an outwards conformation (Figure 5A). Here again, back-calculated chemical shifts show a much lower Y78Cα signal in the Y78CO outwards conformation (predicted ΔY78Cα $_{\text{inwards - outwards}}$ = +2 ppm) (Figure 5C, D). These results imply that a Y78CO outwards state is frequently sampled in E71I (Y78Cα CSP = -1.94 ppm relative to WT KcsA) and less frequently or only partially in E71A (Y78Cα CSP = -0.84 ppm). Note that we could not observe a Y78CO outwards state in E71A simulations, presumably due to insufficient sampling.

Destabilisation of the critical interaction D80 – W67

An especially remarkable finding in our study is the drastically increased filter dynamics in E71I compared to E71A despite similar nonpolar E71 substitutions, and this surge in flexibility most likely causes increased sampling of the Y78CO outwards state in E71I. We used MD simulations to gain a molecular understanding of the enhanced E71I filter dynamics. In our simulations, the conformational space of the D80 side chain is an event of particular interest (Figure S6). In WT KcsA, the interaction with E71 locks D80 in a down conformation (Figure 6A), and only this conformation enables the W67 – D80 interaction, which is critical for gating in Kv channels[38,39]. The down conformation prevails in E71A, enabling a steady W67 – D80 interaction (Figure 6B, D). However, in E71I simulations, the bulky isoleucine sterically destabilises the W67 – D80 interaction and causes D80 to increasingly sample middle and up conformations (Figure 6C). We validated the loss of the W67 – D80 interaction in E71I with ssNMR ^{15}N T$_1$ relaxation experiments that are sensitive to the fast pico-to-nanosecond motion of unbound side chains. These

experiments clearly show markedly enhanced W67 side chain dynamics in E71I, confirming an unstable W67 – D80 interaction in this mutant (Figure 6D, E). To compensate, D80 increasingly engages in interactions with the functionally important residues R64 and Y82[4,31] that are hardly sampled in WT KcsA. The D80 promiscuity is pronounced in MD simulations of E71I and E71Q and agrees with the enhanced ssNMR R_{1rho} dynamics at the filter entrance of E71I and E71Q (Figure 3). In E71A, however, a steady D80 – W67 interaction stabilises the filter, as demonstrated by strongly reduced R_{1rho} dynamics, and this stabilisation is most likely the reason why the Y78CO outwards state is much less frequently sampled in E71A than in E71I. Interestingly, our extensive MD analysis also demonstrates that the E71 point-mutations and the D80 promiscuity cause long-range modulations in the turret (Figure S6), which presumably relate to the turret heterogeneity in the mutants (Figures 2C and 3).
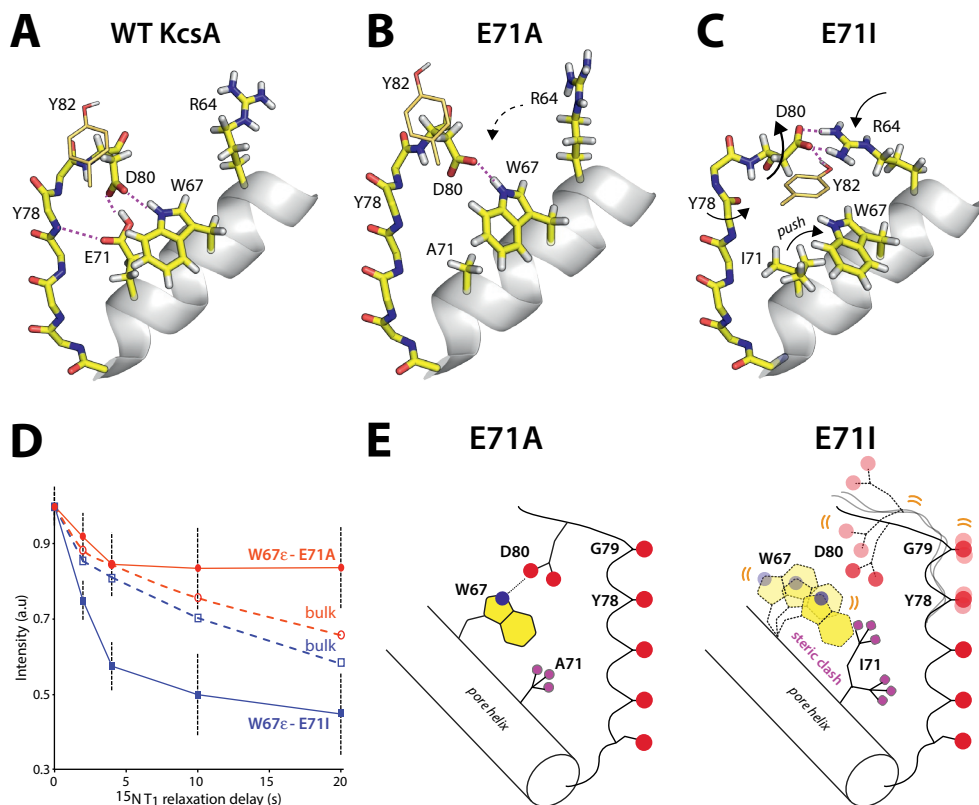
Figure 6. The functionally critical W67 – D80 interaction is destabilised in E71I KcsA. A) WT KcsA MD simulation: The tight interaction with E71 locks the D80 side chain in a down configuration that enables hydrogen bonding with W67 (snapshot after 270 ns). B) E71A simulation: The down conformation prevails, enabling the W67 – D80 interaction, which stabilizes the filter entrance (snapshot after 600 ns). C) E71I simulation: I71 impedes the W67 – D80 interaction which destabilizes the filter

entrance. D80 engages in interactions with Y82 (from a neighboring channel subunit) and R64 (snapshot after 600 ns). D) Longitudinal relaxation times (^{15}N T_1) that report on fast motion of the W67 side chain for E71A (red circles) and E71I (blue squares), measured at 950 MHz and 60 kHz MAS. The error shows the signal to noise ratio for W67Nε at a given data point. Source data are provided as a Source Data file. E) (left) The W67 – D80 interaction is maintained in E71A. (right) I71 hinders the W67 – D80 hydrogen bond, which entails increased dynamics at the pore mouth.

Discussion

Modal gating shifts at constant experimental conditions have been observed in K⁺,[4,6-10] Na⁺,[40] Ca²⁺[41,42], and other ion channels[43,44], and are considered a widespread regulatory mechanism[11,45], potentially to achieve intermediate activity levels. While known for a long-time, the molecular underpinning of modal gating behaviour is poorly understood. In KcsA, E71 point-mutations emulate modal gating shifts, however, X-ray structures of E71X mutants showed no differences compared to WT KcsA[6]. These seemingly disparate perspectives of functional heterogeneity and of structural similarity raise critical problems for our understanding of modal gating and also of Kv channel function (Figure 1B). Our ssNMR study in native-like conditions paints a strikingly different picture, demonstrating that E71 substitutions lock the selectivity filter in characteristic conformational and motional landscapes that markedly diverge from WT KcsA. These landscapes strongly depend on the nature of residue 71 and directly relate to the heterogeneous functional behaviour observed in K⁺ channels[6].

By integrating ssNMR and MD simulations, we show that E71 point-mutations rearrange the network behind the filter and perturb the K⁺ binding sites V76 and Y78 (Figure 1A, E). Thereby, we show that E71X mutations change the equilibrium between intrinsically sampled filter states (Figure 5E), which agrees with 2D IR data[35] and the so-called 'flipped' E71A structure that point towards a complex selectivity filter landscape that includes dynamical flips of K⁺ coordinating peptide planes[35]. Our data demonstrate a stabilisation of the V76CO inwards state in E71A and E71I relative to WT KcsA, which correlates with a sharply reduced entry into the C-type inactivated state. Furthermore, our data clearly show Y78 conformational perturbations in E71I and E71A. Such perturbations could not be observed in WT KcsA X-ray structures[3], however, there is strong evidence from previous ssNMR studies that Y78 modulations can accompany filter gating. Indeed, ssNMR data show that Y78Cα exhibits a drastically lower signal in the open-collapsed state (experimental ΔY78Cα $_{\text{conductive filter – collapsed filter}}$ = +4.3 ppm),[37] which unambiguously argues that the Y78 conformation can change in reference to the filter mode. This notion is also corroborated by the 'flipped' E71A X-ray structure (2ATK), which also features a Y78CO partial outward state[4,46], and it is in line with a recent cryo-EM structure

of the hERG channel[47]. While the exact role in KcsA is unclear, we surmise that Y78 backbone modulations may relate to a non-conductive state that is favoured by E71I, which agree with the strongly reduced K^+ occupancy at S0 – S2 in E71I[6].

Importantly, the marked conformational changes in the E71I selectivity filter, and especially the sterically destabilisation of the W67 – D80 interaction (Figure 6D, E) suggest to be of broad relevance for Kv channels (Figure 1B) where the W67 – D80 interaction plays a defining role in the inactivation process. Mutational studies showed that the inability to establish this highly conserved interaction entails severe functional perturbations for KcsA, Shaker, and Kv1.2[38,39]. Moreover, in line with the effect of the weakening of the W67 – D80 interaction in E71I, the destabilisation of the analogous interaction W434 – E447 in Shaker modulates the equilibrium between conducting and non-conducting filter states[48].

On the basis of our set of results, we show that modal gating shifts in K^+ channels relate to changes in the statistical weighting of pre-existing selectivity filter states which are triggered by fluctuations in the hydrogen bonding (Figure 6) and water network (Figure 4). Notably, we show that modulations in this network cause changes in the turret over more than 2 nm (Figure 2C, 3), which opens a pathway how turret-binding drugs, lipids or other protein can allosterically modulate the filter[21,25,49-51]. The question arises why most of these conformational subtypes could not be crystallised. Here, the reason is most likely the interaction with Fab fragments that act as crystallographic chaperons and attach to KcsA X-ray structures. In agreement with electrophysiological measurements[4], these artificial Fab interactions lock the selectivity filter in a specific conformation, and thereby hinder the capturing of transient configurations, masking the effect of E71 point-mutations. Interestingly, the lack of 'non-canonical' filter conformations in X-ray structures was mirrored by additional torsional or position restraints in MD simulations to stabilise a conductive filter conformation[52,53]. At least for KcsA, such potentials could mask the physiological filter plasticity, as demonstrated in this study and previously with 2D IR[35].

In conclusion, our work establishes the shifts in the conformational dynamics of the selectivity filter as the key physiological determinant of modal gating shifts. At the same time, our work provides a long-needed quantitative description of the selectivity filter dynamics in a native environment, which is of fundamental importance to understand ion channel function[54]. Given that the here described filter dynamics are strongly different in mutant E71I, our study may ultimately help to better understand eukaryotic Kv channels. Finally, we like to emphasize that further experiments with open channels under inactivating conditions will be critically required to fully comprehend how E71X mutations modulate channel open probability and C-type inactivation.

Materials and methods

Sample preparation. WT KcsA and E71X mutant channels were expressed in *Escherichia coli* M15 cells (Qiagen) using standard H_2O-based M9 medium supplemented with 0.5 g/L $^{15}NH_4Cl$ and 2 g/L D-glucose-^{13}C6-d7 in order to improve the spectral resolution in ^{1}H-detected ssNMR-experiments[17]. Cells were subsequently harvested, treated with lysozyme, and lysed via French press. The membranes containing the KcsA channels were collected by centrifugation (100000 x g) and proteins were extracted with 40 mM DM (Anatrace)[26]. KcsA channels were purified using Ni-NTA agarose beads (Qiagen), resulting in a final yield of 10 mg/L for WT KcsA and 5 mg/L for the E71X KcsA mutants. Liposome reconstitution was performed using *E.coli* polar lipids (Avanti) at 1:100 protein:lipid molar ratio, in which detergent was removed using polystyrene beads (Bio-Beads SM-2).[26] Before the ssNMR measurements, reconstituted samples were suspended in fully protonated phosphate buffer (pH 7.4, 100 mM K⁺). For spectral assignments, a fully protonated buffer was used in order to observe the entire channel in ^{1}H-detected ssNMR experiments. For proton/deuterium (H/D) exchange ssNMR spectroscopy, ion channels were incubated in fully deuterated buffers (pH 7.4, 100 mM K⁺) for a total of two days prior to the measurements.

Solid-State NMR spectroscopy. 3D ssNMR experiments for sequential backbone chemical shift assignments were performed at 800 MHz (^{1}H-frequency) using 60 kHz magic angle spinning (MAS) frequency and a real temperature of approximately 305 K. In total, we ran ten dipolar-based 3D ssNMR experiments to assign the three mutant channels and WT KcsA. The pulse sequences and experimental setups were performed as previously descried[17]. 2D ^{13}C-^{13}C PARISxy[55] (N = ½, m=1) experiments for side chain chemical shift assignments were performed at 700 MHz using 42 kHz MAS and a ^{13}C-^{13}C mixing time of 110 ms. ^{15}N T_{1rho} relaxation experiments were performed as described for the water-inaccessible part of KcsA and measured at 700 MHz and 58 kHz MAS using a ^{15}N spin lock amplitude of 17.5 kHz[17]. We used ^{1}H-detected 2D experiments together with relaxation increments of 0, 5, 10, 20, 40, and 80 ms. For the much faster relaxing flicker E71Q channel, we used increments of 0, 5, 10, 20, 40, and 60 ms. ^{15}N T1 measurements were performed at 950 MHz and 60 kHz MAS using relaxation elements of 0, 2, 4, 10, and 20 s. The W67 side chain is spectrally isolated in E71A and E71I (Figure S2) and could be readily analysed in a series of 1D experiments. For the analysis of H/D exchange data from 2D NH spectra acquired in protonated and deuterated buffers, we used the signal intensities, which were normalised to the water-inaccessible residues S69 and V70 that are not subjected to H/D exchange. PISSARRO[56] decoupling was used as decoupling method in all direct and indirect dimensions. Chemical shifts were back-calculated from MD simulations with the SPARTA⁺ program[36]. Channels

structures were extracted from MD simulations with a time-increment of 10 ns, yielding a total of 400 monomer structures. Compared to our experimental data, the SPARTA+ predictions give systematically lower chemical shifts for the V76 backbone carbonyl carbon, which we aligned by adding 2.5 ppm to the predicted carbonyl chemical shifts for all channels.

Molecular Dynamics Simulations. Atomic models of KcsA were constructed based on crystal structures, (1K4C[3] and 3OR6[6]) that represent a structural state with closed inner gate. After energy minimization, the conductive filter was restrained for 10-20 ns to relax any unfavorable contacts destabilizing the filter. Considering the high similarity between crystal structures of WT (1K4C), E71A (1ZWI), and E71I (3OR7), the simulation systems for E71A and E71I are built based the fully equilibrated WT system by introducing respective single mutation. With more substantial difference compared with WT, crystal structure for E71Q (3OR6) was used to build its simulation system. For all MD simulations, the channel was embedded in a bilayer of 3:1 POPC : POPG lipids and solvated in 150 mM or 200 mM KCl using the web service CHARMM-GUI[57,58]. Most residues were assigned their standard protonation state at pH 7. The total number of atoms in the MD systems is on the order of ~49,000. The CHARMM force field PARAM36 for protein[59], lipids[60], and ions[61] was used. Explicit water was described with the TIP3P model. In WT, the residue Glu71 is protonated to form a key hydrogen bond with Asp80[39,62]. The models of KcsA were refined using energy minimization for at least 2000 steps, and the ions and non-filter backbone atoms were kept fixed throughout the minimization procedure. All the simulations were performed under constant NPT conditions at 310 K and 1 atmosphere, and periodic boundary conditions with electrostatic interactions were treated by the particle-mesh Ewald (PME) method and a real-space cutoff of 12 Å. The simulations use a time step of 2 fs. After minimization and equilibration with harmonic positional restraints on all of the C atoms, MD simulations were performed for 1μs for wild type and all mutants, by using either NAMD version 2.11,[63] or on the special purpose computer Anton (Pittsburgh Supercomputer Center)[64].

Data availability. Data supporting the findings of this manuscript are available from the corresponding author upon reasonable request. The solid-state NMR assignments have been deposited in the BMRB (accession number 27676 for WT KcsA, 27678 for E71A KcsA, 27679 for E71I KcsA, and 27680 for E71Q KcsA). The source data underlying Figures 1D, 3A, 5B, 6D, and Supplementary Figure 3 are provided as a Source Data file.

Supplementary information
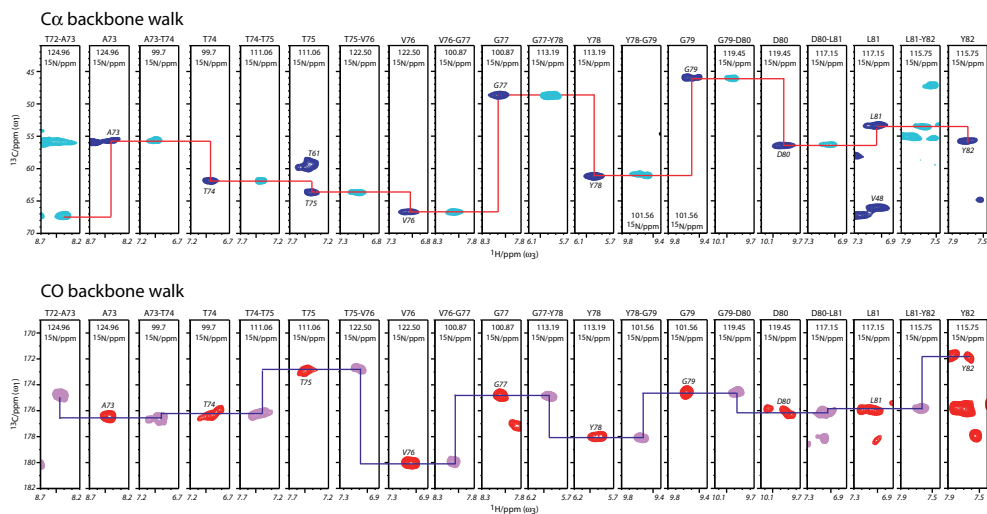
Figure S1. Sequential ssNMR assignments with ¹H-detected 3D experiments. Upper panel: Cα-Cα⁺¹ backbone walk showing full connectivity for residues T72 – Y82 in KcsA mutant E71A. Dark blue signals show CαH planes from a 3D CαNH experiment, cyan CαH planes were taken from a 3D Cα(CO)NH experiment. Lower panel: CO-CO⁺¹ backbone walk showing full connectivity for residues T72 – Y82 in E71A. Magenta signals show COH planes from a 3D CONH experiment, red COH planes were taken from a 3D Co(Cα)NH experiment.

5

2D NH spectra
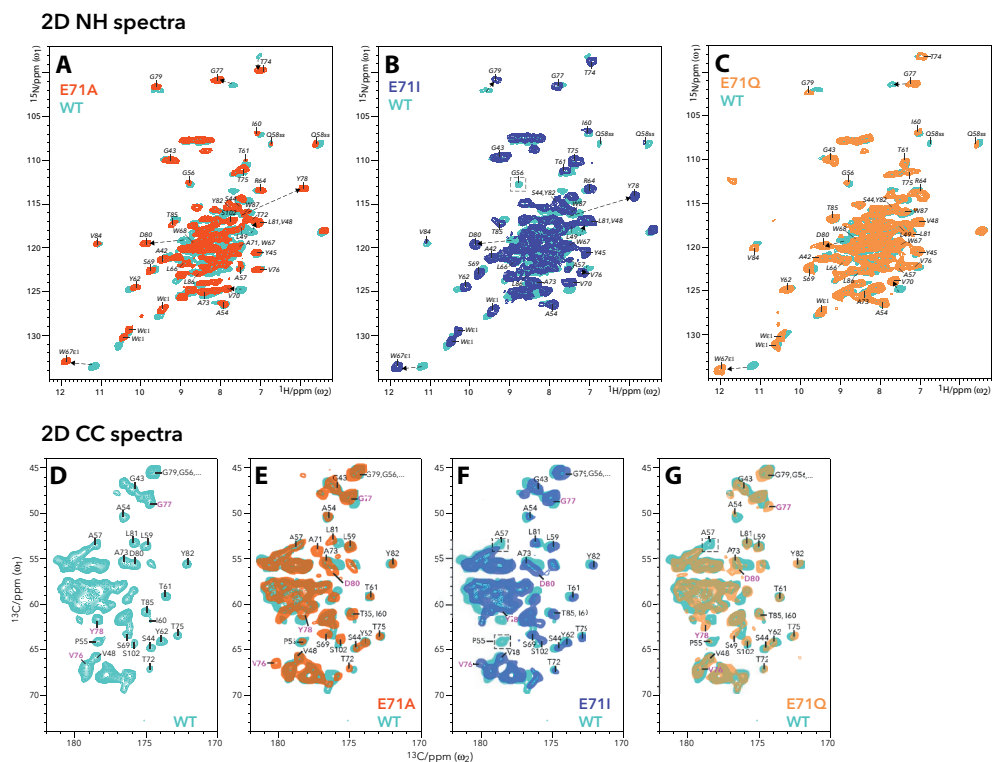
2D CC spectra

Figure S2. Comparison of 2D NH and 2D CC ssNMR spectra of WT KcsA and the E71X mutants. Upper row: Overlay of 2D NH spectra of WT KcsA (cyan) onto A) E71A (red), B) E71I (blue), and C) E71Q (orange). Lower row: Zoom into the carbonyl-region of 2D PARISxy[55] CC experiments. D) WT KcsA (cyan), E) E71A (red) and WT KcsA, F) E71I (blue) and WT KcsA, G) E71Q (orange) and WT KcsA. Signals of V76-Y78 and D80 that show larger chemical shift perturbations are highlighted in magenta. Signals of P55-A57 that disappear or split in E71I due to conformational heterogeneity are highlighted in dashed boxes.
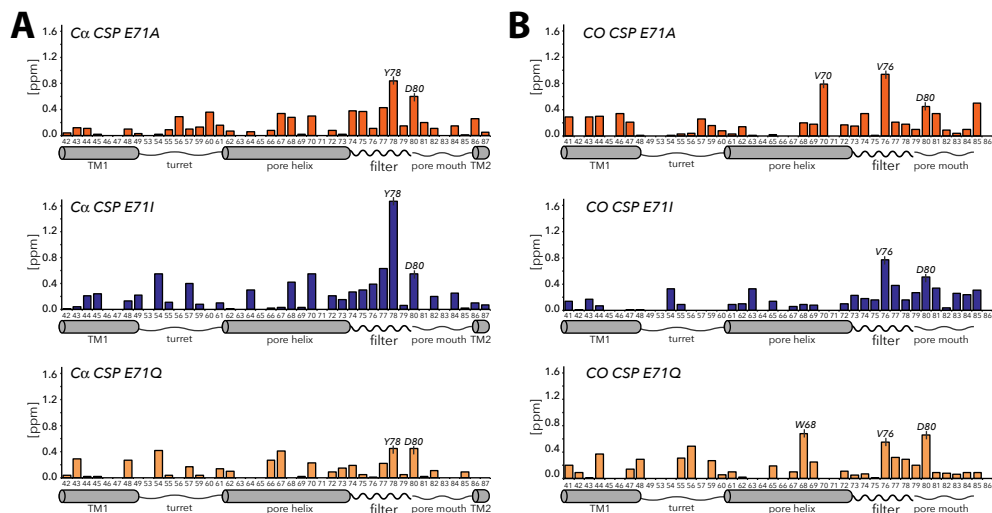
Figure S3. Cα and CO ssNMR chemical shift perturbations of the E71X KcsA mutants. Left panel: Cα CSPs for E71A (in red), E71I (blue), and E71Q (orange). Right panel: Corresponding CO CSPs. Source data are provided as a Source Data file.
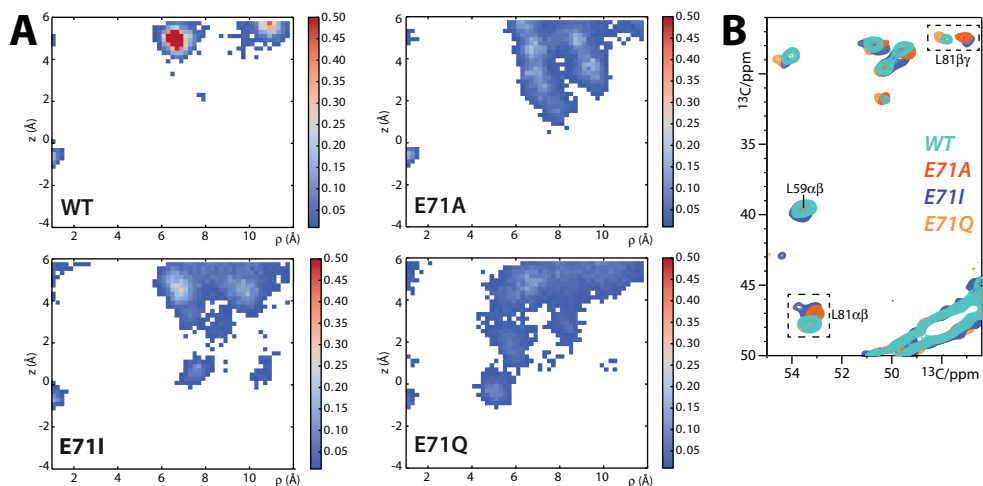
Figure S4. Water distribution derived from long MD simulations / Structural changes in the water-lid. A) 2D average occupancy map for all four subunits during 1000ns MD simulations. The x-axis describes the radius to the center of the selectivity filter, and the y-axis is the z-coordinate of water molecules. In agreement with our ssNMR data, MD simulations show a widening of the water cavity for mutant channels E71I and especially E71A. In these channels, the cavity water also exhibits a higher mobility, as described by higher exchange-rates with bulk water (see C). For E71Q, the simulations could not reproduce the smaller water cavity that we unambiguously detect in solid-state NMR experiments. Potential reasons for the mismatch between ssNMR and MD simulations for E71Q could be a suboptimal MD starting structure (which was derived

from WT KcsA) and insufficient sampling. B) The increased exchange with bulk water in mutants E71A and E71I most likely relates to structural and dynamical changes of residues D80 – Y82, which act as lid of the water cavity[31]. Indeed, we observe marked structural changes in the L81 side chain conformation in 2D CC ssNMR spectra of E71A and E71I. C) MD derived water exchange rates with bulk water:

	WT	E71I	E71A	E71Q
Number of water molecules	0.81±0.12	1.47±0.21	2.30±0.16	1.58±0.16
Turnover time (ns)	51.9±40.9	7.51±4.82	18.5±8.9	6.7±1.9

The water-binding cavity within each subunit is defined as the space with a distance less than 7 A° from both the nitrogen (or substituted ester oxygen) atom from Gly77 and the Cα from E71 in the same monomer. The number of water molecules within each subunit was determined as the average water number within this pocket during specific trajectory. The mean turnover time of water molecules within each subunit is defined as T_MD <N> = n_d, where T_MD is the length of the trajectory, <N> is the average number of water molecules in one cavity, and n_d is the number of distinct water molecules that visited the cavity at least once during the simulation. Each of the four subunits was treated as an individual sample to estimate the average and standard deviation. This kind of analysis was also used in previous studies[32].
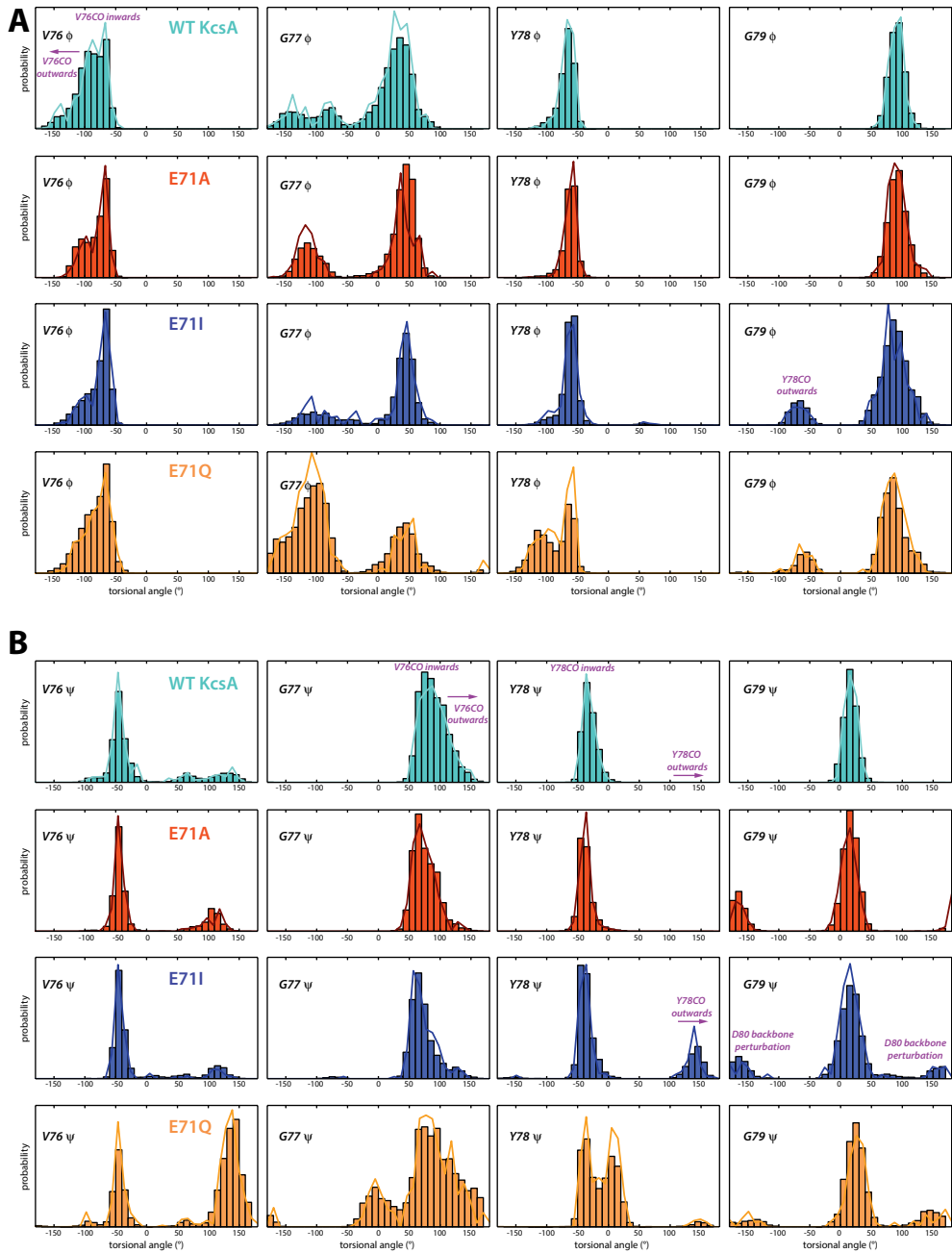
Figure S5. Simulated dihedral angle profiles of WT KcsA and the E71X mutant channels. A) Phi (φ) and B) Psi (ψ) torsional angle distribution of selectivity filter residues of WT KcsA (cyan), E71A (red), E71I (blue), and E71Q (orange) derived from 1 μs-long MD simulations.
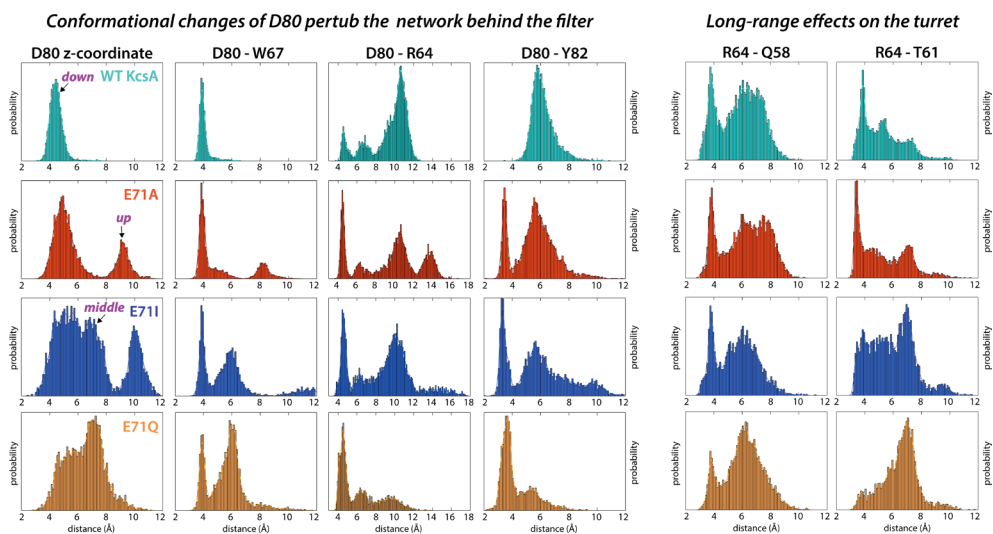
Figure S6. Distance measurement between side chains derived from MD simulations. Distance measurement between side chains derived from 1 μs-long MD simulations of WT KcsA (cyan), E71A (red), E71I (blue), and E71Q (orange). The D80 side chain conformation is shown as the distribution of its z-coordinate (the centre of mass of carboxyl group). For distance measurements, the atom selections are D80 (Cγ), Y82 (OH), W67 (Nε1), T61 (Og1), Q58 (backbone carbonyl oxygen), and R64 (Cζ). Q58, T61, R64, W67, and D80 are from the same subunit, while Y82 is from an adjacent subunit.

References

1   Yellen, G. The voltage-gated potassium channels and their relatives. *Nature* **419**, 35-42, doi:10.1038/nature00978 (2002).

2   Doyle, D. A. *et al.* The structure of the potassium channel: Molecular basis of K+ conduction and selectivity. *Science* **280**, 69-77, doi:DOI 10.1126/science.280.5360.69 (1998).

3   Zhou, Y. F., Morais-Cabral, J. H., Kaufman, A. & MacKinnon, R. Chemistry of ion coordination and hydration revealed by a K+ channel-Fab complex at 2.0 angstrom resolution. *Nature* **414**, 43-48, doi:Doi 10.1038/35102009 (2001).

4   Cordero-Morales, J. F. *et al.* Molecular determinants of gating at the potassium-channel selectivity filter. *Nat Struct Mol Biol* **13**, 311-318, doi:DOI 10.1038/nsmb1069 (2006).

5   Cordero-Morales, J. F. *et al.* Molecular driving forces determining potassium channel slow inactivation. *Nat Struct Mol Biol* **14**, 1062-1069, doi:10.1038/nsmb1309 (2007).

6   Chakrapani, S. *et al.* On the structural basis of modal gating behavior in K+ channels. *Nat Struct Mol Biol* **18**, 67-+, doi:10.1038/nsmb.1968 (2011).

7   Zagotta, W. N., Hoshi, T. & Aldrich, R. W. Shaker potassium channel gating. III: Evaluation of kinetic models for activation. *J Gen Physiol* **103**, 321-362 (1994).

8   Zheng, J. & Sigworth, F. J. Selectivity changes during activation of mutant Shaker potassium channels. *J Gen Physiol* **110**, 101-117 (1997).

9   Schoppa, N. E. & Sigworth, F. J. Activation of shaker potassium channels. I. Characterization of voltage-dependent transitions. *J Gen Physiol* **111**, 271-294 (1998).

10 Chakrapani, S., Cordero-Morales, J. F. & Perozo, E. A quantitative description of KcsA gating II: single-channel currents. *J Gen Physiol* **130**, 479-496, doi:10.1085/jgp.200709844 (2007).

11 Bicknell, B. A. & Goodhill, G. J. Emergence of ion channel modal gating from independent subunit kinetics. *Proc Natl Acad Sci U S A* **113**, E5288-5297, doi:10.1073/pnas.1604090113 (2016).

12 Cuello, L. G., Cortes, D. M. & Perozo, E. The gating cycle of a K+ channel at atomic resolution. *Elife* **6**, doi:ARTN e2803210.7554/eLife.28032 (2017).

13 Heer, F. T., Posson, D. J., Wojtas-Niziurski, W., Nimigean, C. M. & Berneche, S. Mechanism of activation at the selectivity filter of the KcsA K+ channel. *Elife* **6**, doi:ARTN e2584410.7554/eLife.25844.001 (2017).

14 Cheng, W. W. L., Mccoy, J. G., Thompson, A. N., Nichols, C. G. & Nimigean, C. M. Mechanism for selectivity-inactivation coupling in KcsA potassium channels. *P Natl Acad Sci USA* **108**, 5272-5277, doi:10.1073/pnas.1014186108 (2011).

15 Chevelkov, V., Rehbein, K., Diehl, A. & Reif, B. Ultrahigh resolution in proton solid-state NMR spectroscopy at high levels of deuteration. *Angew Chem Int Edit* **45**, 3878-3881, doi:10.1002/anie.200600328 (2006).

16 Agarwal, V. *et al.* De novo 3D structure determination from sub-milligram protein samples by solid-state 100 kHz MAS NMR spectroscopy. *Angew Chem Int Ed Engl* **53**, 12253-12256, doi:10.1002/anie.201405730 (2014).

17 Medeiros-Silva, J. *et al.* 1 H-Detected Solid-State NMR Studies of Water-Inaccessible Proteins In Vitro and In Situ. *Angew Chem Int Ed Engl* **55**, doi:10.1002/anie.201606594 (2016).

18 Andreas, L. B. *et al.* Structure of fully protonated proteins by proton-detected magic-angle spinning NMR. *Proc Natl Acad Sci U S A* **113**, 9187-9192, doi:10.1073/pnas.1602248113 (2016).

19   Retel, J. S. *et al.* Structure of outer membrane protein G in lipid bilayers. *Nature Communications* **8**, doi:ARTN 207310.1038/s41467-017-02228-2 (2017).

20   Medeiros-Silva, J. *et al.* High-resolution NMR studies of antibiotics in cellular membranes. *Nat Commun* **9**, 3963, doi:10.1038/s41467-018-06314-x (2018).

21   Ader, C. *et al.* A structural link between inactivation and block of a K+ channel. *Nat Struct Mol Biol* **15**, 605-612, doi:10.1038/nsmb.1430 (2008).

22   Weingarth, M. *et al.* Quantitative Analysis of the Water Occupancy around the Selectivity Filter of a K+ Channel in Different Gating Modes. *J Am Chem Soc* **136**, 2000-2007 (2014).

23   Cuello, L. G. *et al.* Structural basis for the coupling between activation and inactivation gates in K+ channels. *Nature* **466**, 272-U154, doi:10.1038/nature09136 (2010).

24   Pan, A. C., Cuello, L. G., Perozo, E. & Roux, B. Thermodynamic coupling between activation and inactivation gating in potassium channels revealed by free energy molecular dynamics simulations. *J Gen Physiol* **138**, 571-580, doi:10.1085/jgp.201110670 (2011).

25   Lange, A. *et al.* Toxin-induced conformational changes in a potassium channel revealed by solid-state NMR. *Nature* **440**, 959-962, doi:10.1038/nature04649 (2006).

26   van der Cruijsen, E. A. *et al.* Importance of lipid-pore loop interface for potassium channel structure and function. *Proc Natl Acad Sci U S A* **110**, 13008-13013, doi:10.1073/pnas.1305563110 (2013).

27   Baker, K. A., Tzitzilonis, C., Kwiatkowski, W., Choe, S. & Riek, R. Conformational dynamics of the KcsA potassium channel governs gating properties. *Nat Struct Mol Biol* **14**, 1089-1095, doi:10.1038/nsmb1311 (2007).

28   Good, D. B. *et al.* Conformational dynamics of a seven transmembrane helical protein Anabaena Sensory Rhodopsin probed by solid-state NMR. *J Am Chem Soc* **136**, 2833-2842, doi:10.1021/ja411633w (2014).

29   Lewandowski, J. R., Sass, H. J., Grzesiek, S., Blackledge, M. & Emsley, L. Site-Specific Measurement of Slow Motions in Proteins. *J Am Chem Soc* **133**, 16762-16765, doi:10.1021/ja206815h (2011).

30   Lewandowski, J. R. Advances in solid-state relaxation methodology for probing site-specific protein dynamics. *Acc Chem Res* **46**, 2018-2027, doi:10.1021/ar300334g (2013).

31   Ostmeyer, J., Chakrapani, S., Pan, A. C., Perozo, E. & Roux, B. Recovery from slow inactivation in K+ channels is controlled by water molecules. *Nature* **501**, 121-124, doi:10.1038/nature12395 (2013).

32   Li, J. *et al.* Chemical substitutions in the selectivity filter of potassium channels do not rule out constricted-like conformations for C-type inactivation. *P Natl Acad Sci USA* **114**, 11145-11150, doi:10.1073/pnas.1706983114 (2017).

33   Shi, L., Kawamura, I., Jung, K. H., Brown, L. S. & Ladizhansky, V. Conformation of a seven-helical transmembrane photosensor in the lipid environment. *Angew Chem Int Ed Engl* **50**, 1302-1305, doi:10.1002/anie.201004422 (2011).

34   Medeiros-Silva, J., Jekhmane, S., Baldus, M. & Weingarth, M. Hydrogen bond strength in membrane proteins probed by time-resolved (1)H-detected solid-state NMR and MD simulations. *Solid State Nucl Magn Reson* **87**, 80-85, doi:10.1016/j.ssnmr.2017.03.003 (2017).

35   Kratochvil, H. T. *et al.* Instantaneous ion configurations in the K+ ion channel selectivity filter revealed by 2D IR spectroscopy. *Science* **353**, 1040-1044, doi:10.1126/science.aag1447 (2016).

36   Shen, Y. & Bax, A. SPARTA+: a modest improvement in empirical NMR chemical shift prediction by means of an artificial neural network. *J Biomol Nmr* **48**, 13-

22, doi:10.1007/s10858-010-9433-9 (2010).

37   Wylie, B. J., Bhate, M. P. & McDermott, A. E. Transmembrane allosteric coupling of the gates in a potassium channel. *Proc Natl Acad Sci U S A* **111**, 185-190, doi:10.1073/pnas.1319577110 (2014).

38   Perozo, E., Mackinnon, R., Bezanilla, F. & Stefani, E. Gating Currents from a Nonconducting Mutant Reveal Open-Closed Conformations in Shaker K+ Channels. *Neuron* **11**, 353-358, doi:Doi 10.1016/0896-6273(93)90190-3 (1993).

39   Cordero-Morales, J. F., Jogini, V., Chakrapani, S. & Perozo, E. A multipoint hydrogen-bond network underlying KcsA C-type inactivation. *Biophys J* **100**, 2387-2393, doi:10.1016/j.bpj.2011.01.073 (2011).

40   Howe, J. R. & Ritchie, J. M. Multiple Kinetic Components of Sodium-Channel Inactivation in Rabbit Schwann-Cells. *J Physiol-London* **455**, 529-566, doi:DOI 10.1113/jphysiol.1992.sp019315 (1992).

41   Delcour, A. H. & Tsien, R. W. Altered Prevalence of Gating Modes in Neurotransmitter Inhibition of N-Type Calcium Channels. *Science* **259**, 980-984, doi:DOI 10.1126/science.8094902 (1993).

42   Ionescu, L. *et al.* Mode switching is the major mechanism of ligand regulation of InsP(3) receptor calcium release channels. *J Gen Physiol* **130**, 631-645, doi:10.1085/jgp.200709859 (2007).

43   Popescu, G. & Auerbach, A. Modal gating of NMDA receptors and the shape of their synaptic response. *Nat Neurosci* **6**, 476-483, doi:10.1038/nn1044 (2003).

44   Popescu, G., Robert, A., Howe, J. R. & Auerbach, A. Reaction mechanism determines NMDA receptor response to repetitive stimulation. *Nature* **430**, 790-793, doi:10.1038/nature02775 (2004).

45   Geng, Y. Y. & Magleby, K. L. Modal gating of endplate acetylcholine receptors: A proposed mechanism. *Journal of General Physiology* **146**, 435-439, doi:10.1085/jgp.201511534 (2015).

46   McCoy, J. G., Cheng, W., Thompson, A. N., Nimigean, C. M. & Nichols, C. G. Mechanism for Selectivity-Inactivation Coupling in KcsA Potassium Channels. *Biophys J* **100**, 565-565 (2011).

47   Wang, W. W. & MacKinnon, R. Cryo-EM Structure of the Open Human Ether-a-go-go-Related K+ Channel hERG. *Cell* **169**, 422-+, doi:10.1016/j.cell.2017.03.048 (2017).

48   Lueck, J. D. *et al.* Atomic mutagenesis in ion channels with engineered stoichiometry. *Elife* **5**, doi:10.7554/eLife.18976 (2016).

49   Weingarth, M. *et al.* Structural determinants of specific lipid binding to potassium channels. *J Am Chem Soc* **135**, 3983-3988, doi:10.1021/ja3119114 (2013).

50   Bohlen, C. J. *et al.* A bivalent tarantula toxin activates the capsaicin receptor, TRPV1, by targeting the outer pore domain. *Cell* **141**, 834-845, doi:10.1016/j.cell.2010.03.052 (2010).

51   Visscher, K. M. *et al.* Supramolecular Organization and Functional Implications of K(+) Channel Clusters in Membranes. *Angew Chem Int Ed Engl* **56**, 13222-13227, doi:10.1002/anie.201705723 (2017).

52   Jensen, M. O. *et al.* Mechanism of voltage gating in potassium channels. *Science* **336**, 229-233, doi:10.1126/science.1216533 (2012).

53   Kopfer, D. A. *et al.* Ion permeation in K(+) channels occurs by direct Coulomb knock-on. *Science* **346**, 352-355, doi:10.1126/science.1254840 (2014).

54   Shi, C. *et al.* A single NaK channel conformation is not enough for non-selective ion conduction. *Nat Commun* **9**, 717, doi:10.1038/s41467-018-03179-y (2018).

55   Weingarth, M., Bodenhausen, G. & Tekely, P. Broadband magnetization transfer using moderate radio-frequency fields for NMR with very high static fields and spinning speeds. *Chem Phys Lett* **488**, 10-16, doi:10.1016/j.cplett.2010.01.072 (2010).

56   Weingarth, M., Bodenhausen, G. & Tekely, P. Low-power decoupling at high spinning frequencies in high static fields. *J Magn Reson* **199**, 238-241, doi:10.1016/j.jmr.2009.04.015 (2009).

57   Jo, S., Kim, T., Iyer, V. G. & Im, W. CHARMM-GUI: a web-based graphical user interface for CHARMM. *J Comput Chem* **29**, 1859-1865, doi:10.1002/jcc.20945 (2008).

58   Jo, S., Lim, J. B., Klauda, J. B. & Im, W. CHARMM-GUI Membrane Builder for mixed bilayers and its application to yeast membranes. *Biophys J* **97**, 50-58, doi:10.1016/j.bpj.2009.04.013 (2009).

59   Best, R. B. *et al.* Optimization of the Additive CHARMM All-Atom Protein Force Field Targeting Improved Sampling of the Backbone phi, psi and Side-Chain chi(1) and chi(2) Dihedral Angles. *J Chem Theory Comput* **8**, 3257-3273, doi:10.1021/ct300400x (2012).

60   Klauda, J. B. *et al.* Update of the CHARMM All-Atom Additive Force Field for Lipids: Validation on Six Lipid Types. *J Phys Chem B* **114**, 7830-7843, doi:10.1021/jp101759q (2010).

61   Beglov, D. & Roux, B. Finite Representation of an Infinite Bulk System - Solvent Boundary Potential for Computer-Simulations. *J Chem Phys* **100**, 9050-9063, doi:Doi 10.1063/1.466711 (1994).

62   Bhate, M. P. & McDermott, A. E. Protonation state of E71 in KcsA and its role for channel collapse and inactivation. *Proc Natl Acad Sci U S A* **109**, 15265-15270, doi:10.1073/pnas.1211900109 (2012).

63   Phillips, J. C. *et al.* Scalable molecular dynamics with NAMD. *Journal of Computational Chemistry* **26**, 1781-1802, doi:10.1002/jcc.20289 (2005).

64   D. E. Shaw, R. O. D., J. K. Salmon, J. Grossman, K. M. Mackenzie, J. A. Bank, C. Young, C., M. M. Deneroff, B. Batson, K. J. Bowers et. al. Millisecond-scale molecular dynamics simulations on anton. *Proceedings of the Conference on on high performance computing, networking, storage and analysis*, 1-11 (2009).

CHAPTER 6

Discussion and perspectives

Discussion and perspective

NMR enables the study of proteins at atomic resolution and can provide with detailed insights into their structure, dynamics, topology, and function. Given the large number of drugs that target membrane-embedded and membrane-associated proteins, it is crucial to gain substantial knowledge on the underlying mechanisms by which they function. The integrity and function of these proteins largely depends on their environment[1,2]. This holds true for any kind of biomolecule. Hence, it is crucial to study biomolecules in their physiological context. However, solution NMR is restricted to membrane-embedded and membrane-associated proteins solubilized in detergents or embedded in small bicelles and nanodiscs. Instead, ssNMR has shown to extend the use of solution NMR and enables the study of such proteins in lipid bilayers[3-5], even in close-to-physiological cellular membranes[6]. While broad NMR resonances and sample sensitivity were a limiting factor at first, the advent of advanced methods such as fast MAS[7-9], ^{1}H detection[10-12] and DNP[13,14] make ssNMR more and more routine in the study of (complex) proteins in their native context. Besides membranes proteins, also heterogeneous systems, i.e. amyloid fibrils[15-17], are amenable to ssNMR. In this regard, ssNMR is a unique structural method.

In this thesis, we stress the versatility and strength of ssNMR by investigating three challenging systems: the antibiotic plectasin[18] and its target (**Chapters 2** and **3**), peptidic hydrogels for neural tissue engineering[19] (**Chapter 4**), and the potassium channel KcsA[20] (**Chapter 5**). These ssNMR studies provide with structural and functional rationales that might contribute to a better understanding of therapeutics and their targets.

The plectasin – lipid II complex as seen by ssNMR

Antimicrobial resistance continues to plague the global public health as our current reservoir of effective antibiotics is running empty[21]. Hence, we have reached an era where developing novel antibiotics that are robust to resistance development has become vital. Lipid II, also known as the "Achilles' heel" of bacteria, is a validated target for the design of next-generation antibiotics[22]. A particularly promising class of antibiotics are CSαβ defensins, which can kill refractory pathogens at nanomolar concentrations without known side effects. Despite their promising nature, the physiologically relevant binding mode of CSαβ defensins remains unknown due to challenges that are presented in studying small membrane-embedded drug-target complexes. On the example of the best-studied CSαβ defensin plectasin, our current understanding is derived from a solution NMR study with a truncated lipid II construct[23]. Likewise, previous studies have demonstrated that the study of antibiotic – lipid II complexes necessitates a physiologically relevant context[6]. In **Chapters 2** and **3**, we use a high-resolution ssNMR approach to improve the current understanding

of the plectasin – lipid II complex.

The previous micelle model of the plectasin – lipid II complex[23] showed that residues F2, G3, C4, H18 and C37 tightly interact with lipid II. However, experimental data that justify the involvement of these residues in the complex interface is absent. Moreover, the marked influence of the lipid II sugars on the binding affinity of plectasin[23] could not be explained by the micelle model. In **Chapters 2** and **3**, using ssNMR experiments, we conclusively demonstrate that the plectasin – lipid II complex is markedly different in membranes.

Our ssNMR data showed that using exclusively CSPs between unbound and bound plectasin is insufficient to derive the plectasin – lipid II complex interface, as we observed high CSPs across the entire peptide resulting from lipid II binding. To experimentally define the interface that coordinates the PPi group of lipid II, we monitored the PPi group and its interface with ^{31}P ssNMR spectra of the complex in membranes. These experiments not only confirmed that plectasin targets the PPi group, but also strongly suggested that other residues next to C37 bind directly to the PPi group[23]. With a unique approach, where we co-assembled ^{15}N,^{13}C-plectasin with ^{15}N,^{13}C-lipid II, we could for the first time identify interfacial contacts between plectasin and lipid II using ^{13}C-^{13}C spin diffusion experiments. Such data could finally explain the role of MurNAc and GlcNAc as we repeatedly found interfacial contacts that relate to both sugars. However, due to signal overlap, further ssNMR experiments will be necessary to further characterize the participation of both sugars in the complex. We were also able to clearly pinpoint residues that interact with the pentapeptide, which is critical to plectasin's function[23,24]. Our data demonstrate that the previously suggested interface is not present in membranes. Instead, we found clear interfacial contacts between E2 and residue Y40 of plectasin.

Employing a "FRET-like" ^{15}N(HH)^{13}C DNP-ssNMR experiment on the plectasin – lipid II complex, using ^{15}N, ^{13}C mixed labelled plectasin, unravelled a second binding event that was not observed before. ^{15}N(HH)^{13}C spectra showed that plectasin oligomerizes upon lipid II binding with a histidine side chain at the dimerization interface. This is in line with our ssNMR dynamics and mutational studies[25] that marked the influence of both H16 and H18 on the efficacy of plectasin. Nonetheless, ITC measurements showed that although both H16 and H18 mutants drastically reduced the binding affinity of plectasin, a severe effect was observed with H16. This implies that H16 is involved in lipid II binding, whereas H18 plays a role in dimerization. To further verify this assumption, we will employ ^{15}N(HH)^{13}C experiments on the histidine mutants, which will enable us to identify the function of both histidine residues. This is the first study ever to report on oligomerization events in plectasin.

The discovery of oligomerization events in plectasin raises several new questions that require further studies. 1D HP and 2D NH ssNMR data suggest that oligomerization occurs in equimolar amounts of plectasin and lipid II. Unfortunately, due to the severely impeded spectral resolution in our DNP-ssNMR spectra, we could not unambiguously define the plectasin – plectasin interface. Since we only observed minimal peak doubling in 2D ssNMR spectra, the complex is presumably symmetric. Further mutational and binding studies could shed light on the oligomerization properties of plectasin.

Dynamics studies on the plectasin – lipid II complex also identified an important structural motif that is inherent to the activity of plectasin. While loops in plectasin showed enhanced dynamics, the αβ-loop was virtually as rigid as the secondary structural elements. Moreover, this loop undergoes stark conformational changes upon lipid II binding. Interestingly, both MIC assays and ITC further underlined the importance of the αβ-loop as mutations in residues I22 and Y25 of the loop resulted in a complete loss of function of plectasin. This came as a surprise, since nothing had previously been reported on the role of the αβ-loop. Using ^{13}C-^{13}C spin diffusion experiments, we show that residues I22 and Y25 interact to form most likely a "stapler-like" conformation that might be allosterically involved in lipid II binding.

We have also clearly demonstrated with NMR that plectasin directly binds to divalent ions. While previous studies have emphasized on the influence of divalent ions on the activity of plectasin[26], they could not underpin the reason causing the observed ion sensitivity. Using the paramagnetic properties of Mn^{2+}, we have shown that the negative-patch D9-E10-D11-D12 unique to plectasin is strongly involved in ion coordination. Since our findings are preliminary, we still need to explore the biological relevance of an ion-binding site in plectasin. Thus far, we know that plectasin does not show specificity towards the type of ion it can bind. Moreover, our NMR data suggest that the ion does not prevent the formation of the plectasin – lipid II complex. Further research should exploit the nature of the newly discovered ion binding site in plectasin, which could largely contribute to the rational design of plectasin derivatives.

Although we could not yet establish the full picture of the plectasin – lipid II complex, we have significantly improved our understanding on the complex and have discovered many novel features that are fundamental for the function of plectasin. Ultimately, we should study the plectasin – lipid II complex in cellular membranes and eventually even in whole cells, since the *in vivo* situation might still be very different due to structural variations in the pentapeptide of lipid II among bacteria[27].

Characterization of peptidic hydrogels using ssNMR

Biomimetic scaffolds that support stem cells in their migration, differentiation and proliferation are key to the success of tissue engineering[28]. Hence, in order to design ideal tissue engineering scaffolds, it is a requisite to have an in-depth understanding of their properties. Techniques such as AFM and rheology that are typically used to characterize scaffold properties provide only macroscopic information. Although atomic scale information is critical for the improvement of scaffold functionality[29-31], it is scarce. While largely unexploited, ssNMR can provide atomic level information in tissue engineering scaffolds[32-35]. However, ssNMR studies on complex systems usually requires isotope enrichment that is either prohibitive or entails high costs. In **Chapter 4**, we investigate the properties of a series of peptidic hydrogels designed for treatment of spinal cord injuries using high resolution ssNMR at natural abundance.

Rigidity, as a mechanical scaffold property, was identified as a fundamental regulator in cell migration and differentiation[36,37]. Our dipolar- and scalar based ssNMR experiments that probe immobile and mobile molecular components, respectively, confirmed that rigidity goes hand in hand with functionality. However, exclusively rigidity could not explain the differences in functionality that was observed among the different rigid hydrogels[19].

To analyse the influence of peptide conformation on the mechanical properties, we used ^{1}H-detected 2D ssNMR at natural abundance to obtain ^{1}H-^{13}C assignments. This could be a very interesting application for the study of similar systems as it minimizes materials costs. Our analysis on peptide conformation gave first indications on the self-assembly procedure. Strikingly, comparing peptide conformations in the rigid hydrogels also allowed as to characterize heterogeneity as a novel parameter, which yields fundamental importance in the functionality of scaffolds[19]. From a biological perspective, heterogeneity in the supramolecular organization of scaffolds could interfere with the surface chemistry making it less favourable for cells to adhere. Moreover, rheology experiments showed that polymorphism relates to a reduced mechanical stability in the peptidic hydrogel.

Combining ssNMR with MD simulations provide atomic level insights into the supramolecular organization of scaffolds[38]. In line with our ssNMR experiments, MD simulations showed that biotin and phenylalanine are major intermolecular hotspots during the self-assembly procedure. This is in line with previous studies which demonstrated that aromatic residues have high binding affinities for biotin[39].

Conventional methods such as AFM and rheology could not underpin the molecular differences between the rigid hydrogels[19]. SSNMR, on the other hand, could provide important atomic insights into the mechanical properties

of the different hydrogels and revealed design parameters that were, thus far, ignored. We could potentially push the limits of ssNMR and study such scaffolds directly in the presence of stem cells. Hence, altogether, we have demonstrated that ssNMR is a powerful tool for the high-resolution characterization of tissue engineering scaffolds.

Unravelling the molecular determinants underlying modal gating in K⁺ channels

Many ion channels display a stochastic interplay between different gating modes at constant experimental conditions, known as modal gating[40-42]. Yet, the molecular determinants underlying this process are poorly understood. Previous studies have shown that point-mutations of residue E71 behind the selectivity filter locks the archetypical K+ channel KcsA in different gating modes[40]. While rearrangements in the selectivity filter were suggested to relate to modal gating, curiously, no structural differences were found in the X-ray structures of different E71X mutants[40]. In **Chapter 5**, we used ¹H-detected ssNMR experiments in native-like membranes to investigate the molecular origins of modal gating in KcsA.

To analyse the structural impact of the E71X mutants on WT KcsA, we first assigned ¹H- and ¹³C chemical shifts. While the integrity of the KcsA fold was globally conserved, we observed stark conformational differences in the selectivity filter and the surrounding hydrogen-bond network in E71X mutants. By integrating ssNMR with MD simulations, we discovered that E71X mutants cause rearrangements in the hydrogen-bond network behind the selectivity filter. This network plays an important role in the activity of KcsA[40,43]. SSNMR could also demonstrate that E71X mutants severely affect the turret, which has important implications in drug targeting[44].

Initially, it was suggested that the SF is highly rigid[20], yet recent studies have demonstrated that the filter is rather dynamic[45] which was assumed to relate to modal gating in K⁺ channels. Thus far, no experimental data was available that would support this assumption. In **Chapter 5**, we use ssNMR to study the dynamics of the different E71X mutants. Interestingly, our relaxation data revealed drastic differences in dynamics in the different gating modes. MD simulations further showed that rearrangements in the network behind the SF relate to these differences in dynamics behaviour in E71X mutants.

Altogether, using ssNMR we have, for the first time ever, provided critical insights into the molecular mechanism underlying modal gating in the K⁺ channel KcsA. These insights will ultimately help us to have a better understanding on eukaryotic K⁺ channels.

Conclusion

In this thesis, we aimed to contribute to the basic understanding of three challenging systems that are relevant for the design of therapeutics. Using modern ssNMR we provided in-depth insights into the mode of action of plectasin, design parameters for tissue engineering scaffolds, and modal gating behaviour in the K^+ channel KcsA. Lastly, integrating ssNMR data with complementary techniques, such as MD simulations, can further expand our scope on complicated biological systems.

6

References

1   Lee, A. G. Biological membranes: the importance of molecular detail. *Trends in biochemical sciences* **36**, 493-500 (2011).

2   Chipot, C. *et al.* Perturbations of native membrane protein structure in alkyl phosphocholine detergents: a critical assessment of NMR and biophysical studies. *Chemical reviews* **118**, 3559-3607 (2018).

3   Wang, S. *et al.* Solid-state NMR spectroscopy structure determination of a lipid-embedded heptahelical membrane protein. *Nature methods* **10**, 1007 (2013).

4   Cross, T. & Opella, S. Solid-state NMR structural studies of peptides and proteins in membranes. *Current opinion in structural biology* **4**, 574-581 (1994).

5   Andronesi, O. C. *et al.* Determination of membrane protein structure and dynamics by magic-angle-spinning solid-state NMR spectroscopy. *Journal of the American Chemical Society* **127**, 12965-12974 (2005).

6   Medeiros-Silva, J. *et al.* High-resolution NMR studies of antibiotics in cellular membranes. *Nature communications* **9** (2018).

7   Andreas, L. B., Le Marchand, T., Jaudzems, K. & Pintacuda, G. High-resolution proton-detected NMR of proteins at very fast MAS. *Journal of magnetic resonance* **253**, 36-49 (2015).

8   Salager, E. *et al.* Enhanced sensitivity in high-resolution 1H solid-state NMR spectroscopy with DUMBO dipolar decoupling under ultra-fast MAS. *Chemical Physics Letters* **469**, 336-341 (2009).

9   Weingarth, M., Demco, D. E., Bodenhausen, G. & Tekely, P. Improved magnetization transfer in solid-state NMR with fast magic angle spinning. *Chemical Physics Letters* **469**, 342-348 (2009).

10   Reif, B. & Griffin, R. 1H detected 1H, 15N correlation spectroscopy in rotating solids. *Journal of Magnetic Resonance* **160**, 78-83 (2003).

11   Chevelkov, V. *et al.* H detection in MAS solid-state NMR spectroscopy of biomacromolecules employing pulsed field gradients for residual solvent suppression. *Journal of the American Chemical Society* **125**, 7788-7789 (2003).

12   Medeiros-Silva, J. *et al.* 1H-Detected Solid-State NMR Studies of Water-Inaccessible Proteins In Vitro and In Situ. *Angewandte Chemie International Edition* **55**, 13606-13610 (2016).

13   Renault, M. *et al.* Solid-state NMR spectroscopy on cellular preparations enhanced by dynamic nuclear polarization. *Angewandte Chemie International Edition* **51**, 2998-3001 (2012).

14   Bajaj, V. S., Mak-Jurkauskas, M. L., Belenky, M., Herzfeld, J. & Griffin, R. G. Functional and shunt states of bacteriorhodopsin resolved by 250 GHz dynamic nuclear polarization–enhanced solid-state NMR. *Proceedings of the National Academy of Sciences* **106**, 9244-9249 (2009).

15   Petkova, A. T. *et al.* A structural model for Alzheimer's β-amyloid fibrils based on experimental constraints from solid state NMR. *Proceedings of the National Academy of Sciences* **99**, 16742-16747 (2002).

16   Heise, H. *et al.* Molecular-level secondary structure, polymorphism, and dynamics of full-length α-synuclein fibrils studied by solid-state NMR. *Proceedings of the National Academy of Sciences* **102**, 15871-15876 (2005).

17   Asakura, T., Yao, J., Yamane, T., Umemura, K. & Ulrich, A. S. Heterogeneous Structure of Silk Fibers from Bombyx M Ori Resolved by 13C Solid-State NMR Spectroscopy. *Journal of the American Chemical Society* **124**, 8794-8795 (2002).

18   Mygind, P. H. *et al.* Plectasin is a peptide antibiotic with therapeutic potential from a saprophytic fungus. *Nature* **437**, 975 (2005).

19 Gelain, F. *et al.* BMHP1-derived self-assembling peptides: hierarchically assembled structures with self-healing propensity and potential for tissue engineering applications. *ACS nano* **5**, 1845-1859 (2011).

20 Doyle, D. A. *et al.* The structure of the potassium channel: molecular basis of K+ conduction and selectivity. *science* **280**, 69-77 (1998).

21 Ventola, C. L. The antibiotic resistance crisis: part 1: causes and threats. *Pharmacy and therapeutics* **40**, 277 (2015).

22 Breukink, E. & de Kruijff, B. Lipid II as a target for antibiotics. *Nature reviews Drug discovery* **5**, 321 (2006).

23 Schneider, T. *et al.* Plectasin, a fungal defensin, targets the bacterial cell wall precursor Lipid II. *Science* **328**, 1168-1172 (2010).

24 Münch, D. *et al.* Identification and in vitro analysis of the GatD/MurT enzyme-complex catalyzing lipid II amidation in Staphylococcus aureus. *PLoS pathogens* **8** (2012).

25 Chen, H. *et al.* Design and pharmacodynamics of recombinant NZ2114 histidine mutants with improved activity against methicillin-resistant Staphylococcus aureus. *AMB Express* **7**, 46 (2017).

26 Yang, Y. *et al.* Characterization of recombinant plectasin: solubility, antimicrobial activity and factors that affect its activity. *Process biochemistry* **46**, 1050-1055 (2011).

27 Münch, D. & Sahl, H.-G. Structural variations of the cell wall precursor lipid II in Gram-positive bacteria—Impact on binding and efficacy of antimicrobial peptides. *Biochimica et Biophysica Acta (BBA)-Biomembranes* **1848**, 3062-3071 (2015).

28 Scadden, D. T. The stem-cell niche as an entity of action. *Nature* **441**, 1075 (2006).

29 Halperin-Sternfeld, M., Ghosh, M., Sevostianov, R., Grigoriants, I. & Adler-Abramovich, L. Molecular co-assembly as a strategy for synergistic improvement of the mechanical properties of hydrogels. *Chemical Communications* **53**, 9586-9589 (2017).

30 Alberti, K. *et al.* Functional immobilization of signaling proteins enables control of stem cell fate. *Nature methods* **5**, 645 (2008).

31 Brandl, F., Sommer, F. & Goepferich, A. Rational design of hydrogels for tissue engineering: impact of physical factors on cell behavior. *Biomaterials* **28**, 134-146 (2007).

32 Chao, P. H. G. *et al.* Silk hydrogel for cartilage tissue engineering. *Journal of Biomedical Materials Research Part B: Applied Biomaterials* **95**, 84-90 (2010).

33 Shaw, W. J., Long, J. R., Campbell, A. A., Stayton, P. S. & Drobny, G. P. A solid state NMR study of dynamics in a hydrated salivary peptide adsorbed to hydroxyapatite. *Journal of the American Chemical Society* **122**, 7118-7119 (2000).

34 Lin, K. S. *et al.* Mechanistic study of apatite formation on bioactive glass surface using 31P solid-state NMR spectroscopy. *Chemistry of materials* **17**, 4493-4501 (2005).

35 Garcia, H., Barros, A. S., Gonçalves, C., Gama, F. M. & Gil, A. M. Characterization of dextrin hydrogels by FTIR spectroscopy and solid state NMR spectroscopy. *European Polymer Journal* **44**, 2318-2329 (2008).

36 Breuls, R. G., Jiya, T. U. & Smit, T. H. Scaffold stiffness influences cell behavior: opportunities for skeletal tissue engineering. *The open orthopaedics journal* **2**, 103 (2008).

37 Peyton, S. R. & Putnam, A. J. Extracellular matrix rigidity governs smooth muscle

cell motility in a biphasic fashion. *Journal of cellular physiology* **204**, 198-209 (2005).

38   Rad-Malekshahi, M. *et al.* The supramolecular organization of a peptide-based nanocarrier at high molecular detail. *Journal of the American Chemical Society* **137**, 7775-7784 (2015).

39   Saggio, I. & Laufer, R. Biotin binders selected from a random peptide library expressed on phage. *Biochemical Journal* **293**, 613-616 (1993).

40   Chakrapani, S. *et al.* On the structural basis of modal gating behavior in K+ channels. *Nature structural & molecular biology* **18**, 67 (2011).

41   Popescu, G. & Auerbach, A. Modal gating of NMDA receptors and the shape of their synaptic response. *Nature neuroscience* **6**, 476 (2003).

42   Zahradnikova, A. & Zahradnik, I. Description of modal gating of the cardiac calcium release channel in planar lipid membranes. *Biophysical journal* **69**, 1780-1788 (1995).

43   Zhou, Y., Morais-Cabral, J. H., Kaufman, A. & MacKinnon, R. Chemistry of ion coordination and hydration revealed by a K+ channel–Fab complex at 2.0 Å resolution. *Nature* **414**, 43 (2001).

44   Lange, A. *et al.* Toxin-induced conformational changes in a potassium channel revealed by solid-state NMR. *Nature* **440**, 959 (2006).

45   Baker, K. A., Tzitzilonis, C., Kwiatkowski, W., Choe, S. & Riek, R. Conformational dynamics of the KcsA potassium channel governs gating properties. *Nature structural & molecular biology* **14**, 1089 (2007).

Appendices

Summary

Solid-state Nuclear Magnetic Resonance (ssNMR) spectroscopy has emerged as a powerful tool that allows the study of proteins and protein complexes in their native environment. Such information can be of great value especially in the field of drug development. Moreover, ssNMR enables the study of protein dynamics, drug – target interactions and heterogeneous systems. In this thesis, we have investigated the plectasin – lipid II complex, peptidic hydrogels for spinal cord tissue engineering, and modal gating behaviour in the K$^+$ channel KcsA using state-of-the-art ssNMR experiments.

The first part of **Chapter 1** describes the basic principles behind ssNMR. The second part of the chapter briefly introduces the three different systems.

High-resolution ssNMR study of the plectasin – lipid II complex in membranes

Antimicrobial resistance is a growing threat to human health worldwide which urgently calls for novel antibiotics that act through unexploited pathways. A validated and promising target for antibiotic design is lipid II, an essential precursor in the biosynthesis of the peptidoglycan network. A particularly interesting peptide-antibiotic that targets lipid II is the CSαβ defensin plectasin. However, structural data on the drug – lipid II complex are scarce and unavailable in its physiologically relevant membrane environment. In **Chapter 2** and **3**, we exploit the plectasin – lipid II complex in membranes. In **Chapter 2**, we analysed the structure and dynamics of plectasin in the unbound and bound state in great detail using high resolution ssNMR. Comparing plectasin in the two states revealed strong structural changes in previously ignored structural regions of plectasin such as the αβ-loop. We show that hydrophobic residues in the αβ-loop engage in a "stapler-like" interaction critical for lipid II binding. **Chapter 2** also demonstrates that the two histidine sidechains have important roles in the mode of action of plectasin.

In **Chapter 3** we investigated the interface of the plectasin – lipid II complex at high-resolution. We could experimentally show that plectasin indeed targets lipid II at the irreplaceable PPi group. Moreover, we could provide with insights into the complex interface which could finally describe the role of the sugar – pentapeptide head group of lipid II. Our ssNMR experiments could also provide us with the topological orientation of plectasin in the complex.

Strikingly, we discovered several novel features of plectasin, including oligomerization and a binding site for bivalent ions, which may provide promising leads for the rational design of CSαβ defensin-based antibiotics. Interestingly, while one histidine is involved in lipid II, we found strong evidence that the other histidine plays a role in oligomerization. We could also finally explain the function of the unique negative patch in plectasin, which directly binds

the bivalent ion. Overall, we have found stark differences between the mode of action of plectasin in micelles and in membranes, which further underlines the need of physiologically relevant studies for drug design purposes.

Altogether, our ssNMR study has provided with high resolution insights into the plectasin – lipid II complex in lipid membranes. The next step would be to investigate the complex directly in cell membranes and whole cells to further characterize the mode of action of plectasin.

SSNMR spectroscopy for the characterization of tissue engineering scaffolds

Material properties of tissue engineering scaffolds dominate the behaviour of stem cells and are inherent to the success of tissue engineering. Hence, having substantial insights into the material properties is of critical importance. However, techniques such as AFM and rheology that are commonly used for the characterization of such scaffolds only provide with macroscopic insights. In **Chapter 4** we explore the feasibility of studying the mechanical properties of a series of peptidic hydrogels, designed for neural tissue regeneration for treatment of spinal cord injuries, using modern ssNMR at natural abundance.

Using dipolar and scalar based experiments and modern ^{1}H-detected experiments enabled us to characterize the material properties of the different hydrogels. Thereby, we could not only describe material properties such as the rigidity and assembly degree at high resolution, but we could also identity the scaffold conformational heterogeneity as novel and decisive design parameter for the functionality of the scaffolds. Moreover, by integrating ssNMR assignments in MD simulations enabled us to derive the supramolecular organization of several hydrogels. Overall, we have demonstrated that ssNMR methods pave the way to obtain atomic level insights into mechanical properties of tissue engineering scaffolds. Hence, we anticipate that ssNMR will become more routine in the characterization of such scaffold.

The molecular determinants underpinning modal gating in KcsA

Modal gating shifts are a widespread regulatory phenomenon in many ion channels. However, the molecular underpinning of these shifts remains unknown. In **Chapter 5** we explore the molecular origin of modal gating behaviour in the archetypical K^+ channel KcsA in native-like membranes using extensive ssNMR dynamics studies. We characterized the conformation and dynamics of mutant channels that represent the different modal gating modes. By integrating our ssNMR data with MD simulations, we discovered that shifts in the selectivity filter dynamics, caused by fluctuations in the water and hydrogen bonding network, are the driving forces for modal gating behaviour in KcsA. Thereby, our results provide a foundation for an improved understanding of K^+ channels in general.

Samenvatting

Vaste stof NMR (vsNMR) is een krachtige techniek waarmee eiwitten en eiwitcomplexen in hun natuurlijke omgeving kunnen worden bestudeerd. Dergelijke informatie kan van grote waarde zijn, voornamelijk op het gebied van medicijnontwikkeling. Bovendien kan vsNMR toepast worden voor het bestuderen van eiwitdynamica, interacties tussen drug en doelwit, en heterogene systemen. In dit proefschrift hebben we het plectasin – lipid II-complex, peptide hydrogelen voor het regenereren van ruggenmergweefsel en modale kanalisering in de kaliumkanaal KcsA onderzocht.

Het eerste deel van **Hoofdstuk 1** beschrijft de basisprincipes van vsNMR. Het tweede deel van het hoofdstuk introduceert kort de drie verschillende systemen.

Hoge-resolutie vsNMR studie van het plectasin – lipid II - complex in membranen.

Antimicrobiële resistentie is een wereldwijd groeiende bedreiging voor de publieke gezondheid, die dringend nieuwe antibiotica eist die via onbenutte wegen werken. Een gevalideerd en veelbelovend doelwit voor de ontwikkeling van nieuwe antibiotica is lipid II, een essentiële voorloper in de biosynthese van de peptidoglycaanlaag. Een bijzonder interessant peptide-antibioticum dat zich op lipid II richt, is de CSαβ defensin plectasin. Structurele gegevens over het drug – lipid II – complex zijn echter schaars en zelf afwezig in fysiologische condities. In **Hoofdstuk 2** en **3** bestuderen we het plectasin – lipid II – complex in membranen. In **Hoofdstuk 2** hebben we de structuur en dynamica van plectasin zowel in de ongebonden als gebonden toestand gedetailleerd geanalyseerd met hoge resolutie. De vergelijking tussen plectasin in de twee toestanden onthulde interessante en sterke structurele veranderingen die een berlangrijke rol voor de αβ-lus suggereerden. We toonden aan dat hydrofobe residuen in de αβ-lus met elkaar interacteren om een "nietmachine-achtige" conformatie te vormen die kritisch is voor lipid II binding. **Hoofdstuk 2** gaf ook de eerste aanwijzingen dat zowel H16 als H18 een belangrijke rol spelen in het werkingsmechanisme van plectasin.

In **Hoofdstuk 3** hebben we het complex verder onderzocht, waarbij voor het eerst experimenteel kon worden aangetoond dat plectasin inderdaad aan de onvervangbare pyrofosfaat (PPi) groep van lipid II bindt. Bovendien hebben we inzichten verkregen in het raakvlak tussen plectasin en lipid II die uiteindelijk de rol van de suiker – pentapeptide kopgroep van lipid II kon beschrijven. Onze vsNMR-experimenten hebben ook inzicht gegeven in de topologische oriëntatie van gebonden plectasin op het membraan.

We hebben verschillende nieuwe kenmerken van plectasin ontdekt, waaronder oligomerisatie en een bindingsplek voor tweewaardige ionen.

Deze kenmerken kunnen bijdragen aan het rationeel ontwerpen van nieuwe antibiotica. Hoewel een histidine betrokken is bij het binden van lipid II, hebben we sterk bewijs gevonden dat de andere histidine een rol speelt bij het oligomeriseren van plectasin. Verder is het ons ook gelukt om de functie van de negatieve streek in plectasin te verklaren, waarvan wordt aangenomen dat het aan het ion bindt. Over het algemeen hebben we grote verschillen gevonden tussen het werkingsmechanisme van plectasin in micellen en in membranen. Dit benadrukt de noodzaak voor het uitvoeren van fysiologisch relevante studies voor de ontwikkeling van nieuwe geneesmiddelen.

Al met al, heeft onze vsNMR-studie hoge resolutie inzichten gegeven in het plectasin – lipid II – complex in membranen. De volgende stap zou zijn om het complex direct in celmembranen en zelfs in hele cellen te onderzoeken om de werkingswijze van plectasin verder te karakteriseren.

VSNMR als een applicatie voor de karakterisering van scaffolds voor weefselregeneratie

Materiaaleigenschappen van scaffolds voor weefselregeneratie doeleinden domineren het gedrag van stamcellen en zijn daarom onafscheidelijk verbonden aan het succes van weefselregeneratie. Het hebben van enig inzicht in de materiaaleigenschappen is daarom van cruciaal belang. Standaardtechnieken, zoals AFM en reologie, die worden gebruikt voor de karakterisering van dergelijke scaffolds, bieden echter alleen macroscopische inzichten. In **Hoofdstuk 4** onderzoeken we de mechanische eigenschapen van een reeks peptide hydrogelen met behulp van moderne vsNMR zonder het gebruik van ^{13}C isotooplabelverrijking.

Met behulp van dipolaire, scalaire en moderne ^{1}H-detectie experimenten hebben we verschillende materiaaleigenschappen in de hydrogelen kunnen karakteriseren. Daardoor konden we niet alleen rigiditeit en assemblagegraad beschrijven als belangrijke eigenschappen, maar konden we ook heterogeniteit als een nieuwe en beslissende ontwerpparameter voor de functionaliteit voor scaffolds identificeren. Door vsNMR te integreren met MD-simulaties, konden we de supramoleculaire organisatie van de reeks hydrogelen afleiden. Enfin, we hebben aangetoond dat vsNMR-methoden uitermate geschikt zijn voor het verkrijgen van atomair niveau inzichten in de materiaaleigenschappen van scaffolds voor weefselregeneratie. We verwachten ook dat vsNMR meer routine zal worden in in het karakteriseren van zulke scaffolds.

De moleculaire determinanten die modale kanalisering in KcsA ondersteunen

Modale kanaliseringsverschuivingen zijn een geconserveerd fenomeen in talloze ionenkanalen. Het moleculaire mechanisme dat deze verschuivingen veroorzaakt is echter onbekend. In **Hoofdstuk 5** hebben we de onderliggende

A

mechanisme voor modale kanalisering in KcsA in native membranen onderzocht met behulp van vsNMR. We hebben zowel de conformatie als de dynamiek van de verschillende E71-mutanten, die de verschillende kanaliseringsmodes vertegenwoordigen, gekarakteriseerd. Door vsNMR-verkregen informatie te integreren met MD-simulaties, ontdekten we dat schommelingen in de waterstofbrug-netwerk conformatieveranderingen in het selectiviteitsfilter veroorzaken. Deze veranderingen veroorzaken het kanaliseringsgedrag van KcsA. Deze bevindingen bieden een sterke basis voor een beter begrip van kaliumkanalen in het algemeen.

Acknowledgements

These past four years have been an amazing journey and there are many people that I would like to thank for making it such a nice experience. First of all, I would like to express my gratitude towards my supervisor and copromotor, **Markus Weingarth**. Thank you for teaching me NMR, for giving me a plan B when plan A didn't work out, for all the discussions we had, for always challenging me and for pushing me to do better. I have sincerely learned a lot from you and I'm very grateful that you gave me this opportunity.

I would also like to thank the assessment and promotion committee members **Alexandre Bonvin**, **Eefjan Breukink**, **Enrico Mastrobattista**, **Tom Grossman**, **Antoinette Killian**, **Nathaniel Martin** and **Henk Haagsman** for reading and evaluating the thesis.

Marc Baldus, thank you for all the discussions and NMR advices, for giving me access to the solid-state lab and NMR machines, and of course for being my promotor. **Barbara Hendricx**, you were a great help as a secretary and during the PhD procedure. **Geeske Badart**, you are truly an amazing person! You have been very helpful and supportive, and you always look at the bright side of things. Thank you for everything. Thank you **Mark Daniëls** for your valuable help in the lab. You really pushed my plectasin project forward by providing me with the right cells! **Raymond Schellevis**, thank you for all your hard work to keep the lab going, which hasn't always been easy! I also want to thank **Gert Folkers**, whom I could always ask for advice and have interesting discussions with. I did enjoy teaching together with you and some other colleagues (don't tell anyone!). **Johan van der Zwan**, de man die alles kan! The NMR group would be really lost without you. Thank you for your technical support. **Andrei Gurinoc**, thank you for your help with the NMR machines. I enjoyed the interesting stories that you and your wife **Svetlana** told about your time in Saudi Arabia. Also, know that I'm available if you ever need a catsitter! Big thanks to **Klaartje Houben** and previous officemate **Hans Wienk** for helping me with solution NMR measurements. I have learned a lot from you two!

Eefjan Breukink, you have helped me so many times throughout my PhD. Thank you for the pleasant collaboration, for teaching me several new techniques and for your experienced advice. I also want to thank **Henk Haagsman** and **Edwin Veldhuizen** for allowing me to use the ITC instrument in your group. **Edwin**, you are such a fun and easygoing person, I really enjoyed working together with you. Thank you for helping me out with the ITC instrument. Thank you **Nathaniel Martin** and **Kamal Tehrani** for doing the extensive MIC assays. Despite of the large number of mutants that I wanted to include in the assays, you never complained **Kamal**. Thank you for your effort!

The computational group played a big role in creating the nice ambiance at the NMR department. This would not have been possible without the HADDOCK captain **Alexandre Bonvin**. I enjoyed your stories about skiing, golfing and your travels. I hope we can improve your HADDOCK model of the plectasin - lipid II complex someday! Also, thank you for always being in a good mood. **Anna Vangone**, **Li Xue**, **Zeynep Kürkcüoglu** and **Jörg Schaarsmidt**, thank you for the good time at the lab. **Adrien Melquiond** and **Mikael Trellet**, you were such a great duo! You really brought a lot of joy to the lunch table. Also, thank you for the French lessons, it was fun to practice French with

you. **Brian Jimenez** and **Rodrigo Honorato**, I wish you all the best in your research. **Rodrigo**, I really hope you'll never complain about how hot it is during summer. You know better now! **Cunliang Geng**, thank you for bringing the most interesting dishes to our New Year's dinners. The tofu was really amazing! **Farzaneh Meihmandi**, it was very nice to have you in our office, I enjoyed our conversations about Iran and Iranian food. I wish you and your little family all the best! Thank you **Siri van Keulen** for organzing board games night, ladies night and for your overall good mood! **Zuzana Jandova**, you truly are a crazy and fun person! Thank you for the nice and crazy atmosphere you brought to the group. **Francesco Ambrosetti**, the effort it takes to teach you how to count to twenty in Dutch... It was very amusing to see your love for Italy and how everything is fake Italian food. Too bad you made it to my dirty list. Good luck with your next adventure! **Jorge Roel Touris**, you will always be remembered by the red sweater. Thank you for the entertainment, especially at borrels! **Charlotte van Noort**, thank you for your friendliness, your hospitality and for baking me cookies for my birthday! Good luck with everything. **Panagiotis Koukos**, you are the perfect example of "don't judge a book by its cover". You are a wonderful person. Thank you for always helping me, for explaining me things and for not making fun of me (well..most of the time). Oh and I'm excited that you started to like cats!

I want to thank **Rolf Boelens** for his suggestions, interesting discussions and for actively participating at our Wednesday group meetings! **Hugo van Ingen**, it was very kind of you to set up a standarized protocol for the solution NMR machines and for your NMR lessons. Thank you for all your effort and for joining us in Utrecht. I really enjoyed interacting with your group members. **Ulric le Paige**, thank you for all the baking you did for us, for your long long long conversations and for your help in the lab. And for sending me cat pictures! Thank you **Velten Horn** for the interesting life lessons. Also, I kept the avocado plant alive, so thank you for your help! **Heyi Zhang**, I think you are by far the most interesting person I have ever met. Thank you for all the conversations, random questions and the awesomeness you brought to the group. Thank you for your kindness **Clara van Emmerik**. I'm happy to see that hard work pays off. All the best for you and your little family! **Vincenzo Lobbia**, I really enjoyed teaching together with you. Thank you for all your help in the lab and good luck with your challenging project!

Thank you **Shengqi Xiang**, **Marie Renault** and **Deni Mance** for your help with the NMR machines. **Shengqi**, it was very kind of you to give us NMR lessons. It was very educative. **Marie**, I enjoyed our conversations about food, the French language and sailing. **Deni**, it was nice to occasionally travel together by train to work or home and have interesting discussions. **Alessandra Lucini Paioni**, you are truly the happiest person I have come across. I wasn't aware that volleyball and pizza could bring so much joy! Thank you for your emotional support, help with DNP and for answering my (stupid) NMR questions. I loved being your officemate! **Helena Ehren**, you gave crazy a whole new definition. Your love for carnaval and bad music is something I will never understand, but sharing an office with you was never boring. Thank you for all the good times and the entertainment. **Meaghan Ward** (oh hey friend), thank you so much for all the food you've made me when I was sick, for organizing several activities, for your overall good mood and most importantly for making **Fionn Skoog** (**Mookie**)! You and your husband **Chris Skoog** are such kind people and very hospitable. Thank you both for all the good times. Thank you **Yanzhang Luo**, for being the golden boy, for

moving to Gouda and for the nice dinners prepared by your wife **Jane**. Too bad you'll be leaving Gouda, but regardless I wish you both all the best! **Reinier Damman**, I'm still amazed how you can walk around in a t-shirt when its freezing outside and still not be cold. Thank you for your entertainment the past four years, it was lots of fun seeing you practice your African dance moves. Thank you! Big thanks to **Siddarth Narasimhan**, the walking encyclopaedia! The things you know are just endless and very random, but it was entertaining in some way. Thank you for your bad dad jokes, your support and for being there when things became difficult. It's nice to see how different cultures are so alike. **Cecilia Pinto**, I still remember the day we first met. It was this awkward handshake/hug, but from that moment on I knew we would be good friends. I am very happy that you love cats just as much as I do. Now I only need to convince you to move to my beautiful city The Hague! Thank you for being my friend. Another great person is **Ivan Corbeski**. You are one of the most humble, loyal, helpful, caring and honest person I have met. I hope that one day you'll see what you are worth. Thank you for everything and for your friendship. **Agnes Adler**, **David Beriashvili** and **Anamika Gaur**, I wish you all the best with your PhD. I'm sure you'll all be successful. **Agnes**, I enjoyed saying Gutentag to you every single day. **David**, thank you for your friendliness and for sending cat pictures and videos. **Anamika**, I'm super happy that you have joined our group and made it to my clean list!

João Silva, I am grateful for having you as my colleague and friend. You were always willing to help despite the fact that you had lots of work to do yourself. The joy and laughter you brought to the NMR department was priceless. Thank you for your help and support. I am confident that you'll be successful in every way. **Rhythm Shukla**, you are so much fun! I really hope you'll stay the cheerful, social and kind person you are now. And I'm very delighted to see that you have transformed in a crazy cat lady! **Maik Derks**, I wish you all the best with this challenging project. I hope your positive mindset will help you throughout this (sometimes frustrating) journey. Good Luck! Thank you **Federico Fontana** for the nice collaboration on the hydrogel project. I enjoyed your stories about hiking and rowing.

Throughout my PhD, I was lucky to supervise some great students: **Barend Elenbaas**, you were my first student and together we tackled the expression and purification of plectasin. You were a great help with estabilising a protocol for the expression and purification, thank you! **Marek Prachar** and **Felix Torres**, thank you for your help with NMR experiments, MD simulations and all the other computational parts of the projects. I wish you both all the best for your PhD! **Francesca D'Amigo**, you were such an ambitious student. Coming from an organic chemistry lab, you were determined to learn as much as possible about biochemistry in only three months. **Benjamin Vermeer**, I really admired your motivation to work hard and learn new things. I am confident that your hard work will pay off! **Danique Ammerlaan**, when you came around I was so busy supervising the other students, but you managed to work independently and figured out a lot by yourself! One day, you'll be a great scientist if you'd like. **Francesca**, **Benjamin** and **Danique**, thank you for patience, your help and your friendship. I really enjoyed working together with you. I also want to thank my adopted student **Vicky Charitou** for all her great work. You pick up things really fast and I'm certain that great things are ahead of you. I also would like to thank other students I have met: **Christoph Müller-Hermes**, **Bram Vermeulen**, **Felix Kümmerer**, **Thorben Maaß**, **Apfrida**

Kendek, **Sam de Vos, Greg Kafetzopoulos**, **Federico Napoli** and **Tim Neijenhuis**. Thank you all for your kindness and for the nice conversations. **Christoph**, I am happy we became friends. Oh and you are definitely crazy and suikerverslaafd! **Tim**, thank you for taking care of my avocadoplant, pretty sure it wouldn't have survided without you. And **Greg**, never have I encountered a student being so thankful for a coffee card, you are so kind! **Federico**, you are such a hard working person. I wish you the best with your studies.

To all my high school and study friends, thank you very much for your support and patience. Special thanks to **Cindy Kwok** and **Jasmin Kutter** for always looking after me, making sure that I stayed sane and for being there for me when I needed you the most. I'm extremely lucky to have you as friends. **Jasmin**, hold on, you're almost there too! Thank you **Michael van der Geer**, **Danique Hof** and **Stef van der Krieken** for your understanding, your interest and effort to maintain our friendship. I appreciate it a lot. **Michael**, I will have all time to steel Maki now!

Ik wil graag mijn familie, **tante**, **ooms**, **neven** en **nichten,** bedanken voor hun steun, interesse en aanmoedigingen de afgelopen jaren. Lieve schoonfamilie, **Iverna**, **Jos**, **Oma**, **Tosca**, **Carmen** en **Joë (**en de kleine **Yara!)**, bedankt dat jullie me zo liefdevol in jullie familie hebben verwelkomt. Jullie steun heeft veel voor me betekend! **Sanaa**, **Anwar** en **Faissal**, bedankt dat jullie altijd in mij geloofd hebben zelfs op momenten dat ik er doorheen zat. **Pap**, helaas mocht het niet zo zijn dat je dit mee mag maken, maar ik hoop dat ik je trots heb mogen maken. **Mam**, jij hebt me geleerd om hard te werken om mijn doelen te bereiken. Bedankt voor je onvoorwaardelijke liefde, alle opofferingen die je voor ons hebt gemaakt, je steun en aanmoediging.

Last but definitely not least: **Roman Dingjan**, bedankt voor zóveel, voor je steun, je liefde, je vertrouwen, je begrip, je geduld, je zorgzaamheid en je relativeringsvermogen als ik weer eens doordraaide. Je was er echt voor me tijdens "the good, the bad and everything in between". Het was niet gelukt zonder jou aan mijn zijde!

List of publications

Jekhmane, S.; Prachar, M.; Pugliese, R.; Fontana, F.; Medeiros-Silva, J.; Gelain, F.; Weingarth, M.; Design parameters of tissue-engineering scaffolds at the atomic scale. (2019), *Angewandte Chemie International Edition*, 58, 16943-16951

Medeiros-Silva, J.; **Jekhmane, S.**; Breukink, E.; Weingarth, M.; Towards the native binding modes of Lipid II targeting antibiotics. (2019) *ChemBioChem*, 20, 1731-1738

Jekhmane, S.; Medeiros-Silva, J.; Li, J.; Kümmerer, F.; Müller-Hermes, C.; Baldus, M.; Roux, B.; Weingarth, M.; Shifts in the selectivity filter dynamics cause modal gating in K+ channels. (2019) *Nature Communications*, 10, 123.

Medeiros-Silva, J.; **Jekhmane, S.**; Lucini Paioni, A.; Gawarecka, K.; Baldus, M.; Swiezewska, E.; Breukink, E.; Weingarth. M.; High-resolution NMR studies of antibiotics in cellular membranes. (2018) *Nature Communications*, 9, 3963.

Saracino, G.; Fontana, F.; **Jekhmane, S.**; Medeiros-Silva, J.; Weingarth, M.; Gelain, F.; Elucidating self-assembling peptide aggregation via morphoscanner: A New Tool for Protein-Protein Structural Characterization. (2018) *Advanced Science*, 5, 1800471.

Medeiros-Silva, J.; **Jekhmane, S.**; Baldus, M.; Weingarth, M.; Hydrogen bond strength in membrane proteins probed by time-resolved ^{1}H-detected solid-state NMR and MD simulations. (2017) *Solid State Nuclear Magnetic Resonance*, 87, 80-85.

Medeiros-Silva, J., Mance, D.; Daniëls, M.; **Jekhmane, S.**; Houben, K.; Baldus, M.; Weingarth, M.; ^{1}H-detected solid-state NMR studies of water-inaccessible proteins in vitro and in situ. (2016) *Angewandte Chemie International Edition*, 55, 13606-13610.

A

Curriculum Vitae

Shehrazade Jekhmane was born on December 17th 1991 in The Hague, the Netherlands. She obtained her Bachelor's and Master's degree in Molecular Life Sciences at Wageningen University. Her Master's thesis was performed in the group of Dr. Renko de Vries, where she worked on the characterization of artificial viral coat proteins for the delivery of mRNA. Afterwards, she did an internship at FUJIFILM Europe BV where she developed and characterized delivery agents for growth factors for bone tissue regeneration. Both projects resulted in a publication.

In 2016, she joined the group of Dr. Markus Weingarth at the NMR Spectroscopy Research group of Utrecht University. During her PhD, she used solid-state NMR to characterize different challenging biological systems, which have therapeutic applications, in their physiological context. The work of her PhD is described in this thesis.